The Center for Marine and Coastal Studies — North Carolina State University

AN EXPERIMENTAL INVESTIGATION OF SOME COMBINED FLOW SEDIMENT TRANSPORT PHENOMENA

By

LARRY BLIVEN,

NORDEN E. HUANG

and

GERALD S. JANOWITZ

REPORT NO. 77-3
UNC-SG-77-04

FEBRUARY, 1977

AN EXPERIMENTAL INVESTIGATION OF SOME COMBINED FLOW SEDIMENT TRANSPORT PHENOMENA

By

LARRY BLIVEN,

NORDEN E. HUANG

and

GERALD S. JANOWITZ

REPORT NO. 77-3
UNC-SG-77-04

FEBRUARY, 1977

AN EXPERIMENTAL INVESTIGATION OF SOME COMBINED FLOW SEDIMENT TRANSPORT PHENOMENA

by

Larry Bliven,

Norden E. Huang

and

Gerald S. Janowitz

Report No. 77- 3

UNC-SG-77-04

February, 1977

Copies Available From

Center for Marine and Coastal Studies
1204 Burlington Labs.
North Carolina State University
Raleigh, North Carolina 27607

or

UNC Sea Grant College Program
1235 Burlington Labs.
North Carolina State University
Raleigh, North Carolina 27607

ABSTRACT

Sediment transport and the resulting topographic features generated by combined wave and steady flow conditions are studied by laboratory experiments. The investigation is limited to the conditions where bed-load is the dominant transport mode. A dimensional analysis of the sediment and fluid variables is performed to identify the pertinent nondimensional parameters. Various characteristic measures of the sediment profiles are obtained using statistical methods. These topographic measures and the sediment transport are related to the non-dimensional parameters. A generalized expression is introduced to describe the ripple number spectra as a function of the sediment and flow characteristics for both local equilibrium and equilibrium states. The net sediment transport rate is linearly related to the stream power available at the top of the bottom boundary layer as proposed by Bagnold. The possibility of quantitatively measuring the net sediment transport rate by topographic features is proposed.

ACKNOWLEDGEMENTS

We wish to offer our sincere appreciation to Dr. C. E. Knowles, Dr. J. L. Machemehl, and Dr. L. J. Pietrafesa whose critical comments helped promote this research.

Mr. O. David Biddy provided invaluable technical assistance in the laboratory by modifying and maintaining numerous scientific instruments. Thanks are given to Mr. Paul Blankinship, Dr. Charles McClain, and Mr. Jim Singer, who aided in the collection of data. Special thanks are extended to Mr. John Boone for his part in discussions of methods of data analysis.

Dr. Yates Sorrell loaned some equipment from the Engineering Mechanics Department, North Carolina State University. Dr. Steve Long permitted the use of some electronic equipment on loan to North Carolina State University from the National Aeronautic and Atmospheric Administration, Wallops Island, Virginia. Dr. Charles McClain constructed the velocity probe employed in this study.

Major funding for this project was provided by the North Carolina State University Center for Marine and Coastal Studies. Supplemental funding was received from the North Carolina State University Research Administration Faculty Research and Development Fund (Trust No. 09223) and the University of North Carolina Sea Grant College Program, Office of Sea Grant, NOAA, U.S. Dept. of Commerce under Grant No. 04-6-158-44054 and the N. C. Department of Administration. The U.S. Government is authorized to produce and distribute reprints for governmental purposes notwithstanding any copyright that may appear hereon.

TABLE OF CONTENTS (continued)

LIST OF TABLES

LIST OF FIGURES

LIST OF FIGURES (continued)

1. INTRODUCTION

Continental shelves often have noncohesive sedimentary bottoms. For example, Newton et al. (42) mapped the sediment grain size distribution for water depths less than 50 meters (m) on the North Carolina shelf between Cape Fear and Cape Hatteras and found that the sediment varied from mud to coarse sand. For this region, the grain size ranges 0.125 to 0.250 millimeters (mm) and 0.250 to 0.500 mm represented approximately 50 percent of the total area. These grain size ranges correspond to fine and medium sand. The fluid velocity fields on the continental shelves are complex. Some velocity modes which can be present in these systems include: wind generated waves and currents, barotropic and/or baroclinic currents generated by horizontal pressure gradients, and internal gravity waves. Field and laboratory observations have shown that once the velocity in the proximity of a noncohesive sedimentary bed exceeds a "critical" velocity, sediment is transported. Komar et al. (31) photographed sedimentary topographic features indicating sediment transport in water depths up to 125 m on the Oregon continental shelf. The sediment transport generated by the complex velocity field on a continental shelf can be investigated by representing the velocity field as the combination of a quasi-steady current, defined as the sum of all velocity components with periods greater than gravity wave periods, and a nonsteady velocity component, defined as the sum of all velocity components with periods less than or equal to gravity wave periods. Since the velocity associated with gravity waves decays with depth from the free surface and is a function of the mean depth of the water, the wave velocity close to the bed is a meaningful choice for specification of the wave induced velocity in studies of sediment transport. For example, a gravity wave with a height of 3 m and a period of 8 seconds (sec) has a maximum horizontal orbital velocity near the bed of approximately 17 centimeters per second (cm/sec) at a water depth of 30 m and approximately 34 cm/sec at a water depth of 10 m.

The U.S. Army Corps of Engineers (52) defined two sediment transport modes: bedload and suspended load. Bedload transport is the motion of particles along the bed generated by the shear produced by water moving over the sediment bed. Suspended load transport is the transport of particles by currents after the grains have been lifted from the bed. While the transport mode is a function of the sediment and hydraulic characteristics, particles larger than sand sized are predominantly transported as bedload, sand sized particles are commonly transported as bedload with intermittent suspension, and silts and clays are generally transported in suspension.

Sediment transport is an important process concerning man's coastal activities. The design and efficient maintenance of navigable waterways, harbors, and marine structures depends on the stability of the sediment substrate. Beaches are also dynamic sediment transport systems. Beach sediment budgets may include terms representing processes such as stream sources, cliff erosion sources, inlet sources or sinks, onshore or offshore sediment transport, sinks due to transport into submarine canyons, and sources or sinks due to wind blown beach sand. The net result of the sediment transport processes determines whether a beach is eroding, stable, or accreting. Bed topographic features are evidence of sediment transport in areas such as the offshore region, estuaries, rivers, and lakes. Since bedforms are a function of the sediment and flow characteristics and some consolidated sedimentary rocks have preserved these features, a qualitative knowledge of the relationship between sedimentary bedforms and flow conditions aids geologists in their interpretation of previous depositional environments.

McClennen (37) measured the velocity at four locations at approximately 2 m from the bed in water depths of 30 to 143 m on the New Jersey continental shelf during the late springs of 1970 and 1971. The range of the average root-mean-square speeds for these stations during these periods was approximately 12 to 20 cm/sec. McClennen also obtained wave period and height observations for the study area from the National Oceanographic Data Center and employed the Airy wave theory to predict the wave induced orbital velocities near the bed. For a depth of 30 m and an assumed critical velocity of 25 cm/sec for the sediment, either the mean current or the wave induced orbital velocity could generate sediment transport approximately 16 percent of the time. However, McClennen did not consider the case in which both the wave orbital velocity and the steady current combined to generate sediment transport.

Since the flow fields which exist in the offshore region can be a combination of a quasi-steady current and a nonsteady velocity component, it is important to develop and test models which predict the sediment transport rate for these conditions. However, in the past, sediment transport has been extensively investigated for either steady uniform open channel flows or gravity wave motion but it has not been extensively investigated for combined steady current and wave conditions. While measurement of the sediment transport rate in the offshore zone is difficult, some features of the bed topography can more readily be measured in the field or measured indirectly from photographs of the bed topography. Therefore, establishment of quantitative relationships between the bed topographic features and the sediment transport rate would provide a useful tool.

The objective of this study is to establish quantitative measurements of the sediment transport rate and topographic features generated by a combined steady current and gravity wave field in order that the relationships between the sediment transport rate and the flow field, the topographic features and the flow field, and the sediment transport rate and the topographic features can be investigated. The study is limited to the class of flows in which the steady current and the gravity wave propagate in the same direction and bedload transport is the dominant transport mode. To achieve this objective, laboratory experiments were conducted in which a steady uniform current and/or gravity waves were transmitted over an initially flat noncohesive sand bed. The flow characteristics, bedform topography, and sediment transport rates were measured. Using a dimensional analysis, the dynamic sedimentary processes are related to the flow field.

2. LITERATURE REVIEW

2.1 General

Researchers have investigated the dynamic sedimentary phenomena generated by steady open channel flows, gravity waves, and some combined steady current and wave conditions. Various mechanisms have been proposed to explain these phenomena. A brief review of the bed topography and sediment transport phenomena as well as the more successful theories is presented to help advance the investigation of these phenomena in the offshore region of the continental shelf.

The coordinate system and a few basic parameters which are used extensively in this text are displayed in Figure 1. A right-handed Cartesian coordinate system is used. The x-axis lies in the plane of the mean free surface of the fluid and is positive in the direction of the wave propagation. The z-axis is positive vertically upwards. At the mean free surface of the fluid, z equals zero. The elevation of a surface gravity wave is ζ . The distance between successive maximum values of ζ is the wavelength L. The time interval between successive crests is the wave period T. The mean fluid depth is h. The density of the fluid is ρ_f. The average fluid velocity is $\bar{U}$.

The mean bed elevation relative to h is represented as η. The distance between two successive maximum values of η represents the bedform wavelength λ. The local maximum of η is represented as η_m. The mean grain size diameter is represented as d. The density of the sediment is ρ_s.

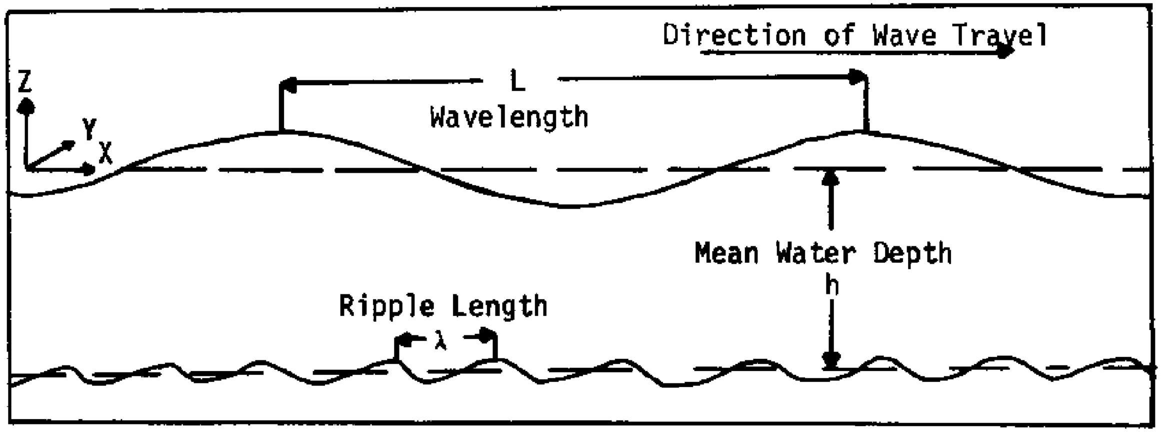

Figure 1. The coordinate system

2.2 Bed Topography

The transport of sediment by a steady uniform open channel flow produces undulations in a noncohesive sediment bed. The topographic features exhibit several well recognized patterns which are a function of the sediment properties and the flow field. The intrinsic relationship between the various topographic patterns and the flow field was established by Simons et al. (48). The experimental investigation differentiated three classes of undulated bedforms: ripples, dunes, and antidunes. The length of a ripple is less than 60 cm but most ripples are less than 30 cm long. The ripple height is independent of the flow depth and is usually less than 5 cm. In the direction of the mean current, a ripple profile is similar to a skewed triangle with the gentle slope facing upstream. Ripples have no effect on the free surface of the water. A dune profile is similar to a ripple profile but its length is greater than 60 cm. The dune height, usually greater than 5 cm, is dependent on the flow depth. The flow field associated with dunes has a free surface standing wave out of phase with the dune topography. The length of an antidune is on the order of meters and the height is on the order of a meter. The flow field associated with antidunes has a free surface standing wave inphase with the antidune topography. Simons et al. (48) also delineated the bedform classes on a graph of the stream power versus grain size. Stream power is defined as the rate at which fluid does work transporting sediment. To delineate the bedform classes, stream power was represented as $\bar{U}\cdot\bar{\tau}$, where the steady uniform current shear stress acting on the bed is represented by $\bar{\tau}$. As the stream power increases, the bedform class progresses from ripples to dunes to antidunes but ripples do not develop when the grain size is greater than 0.60 mm.

Several theories have been advanced to relate the bedform patterns to the hydraulic and sediment characteristics. These theories assume that a deterministic relationship exists between the flow field and the bed topography. Anderson (1) used potential theory to relate the dune length to water depth ratio to the Froude number. The theory compares favorably with experimental data by Hooker (20), Straub (49), and Tison (51). However, the theoretical development does not correspond to the physical system since Anderson erroneously assumed the dune profile was inphase with the free surface standing wave. This assumption is not consistent with the experimental data presented by Simons et al. (48).

Kennedy (28) developed a model for determining the bedform class. He assumed an inviscid flow field, an impermeable bottom boundary, a sediment transport equation related to an arbitrary power of the fluid velocity, and the lag distance concept. The lag distance was defined as the distance which the sediment transport rate lagged the local velocity due to the inertia of the sediment particle. The theory produces solutions corresponding to dunes, flat beds, and antidunes. The solutions are dependent on the Froude number, flow depth, and lag distance.

Ho and Gelhar (19) presented a theoretical analysis for bedform classification similar to the one by Kennedy (28). The essential difference is that the latter theory assumes a permeable bottom boundary. The flow field in the sediment was defined by Darcy's law which represents a linear relationship between the fluid transport rate in a permeable medium and the gradient of the fluid head loss. Since the theory produces solutions corresponding only to a flat bed, the variety of topographic features which is observed in nature is not modeled by this theory.

Since bedform lengths and heights are random varialbes, statistical methods have recently been employed to characterize these features. Many common statistical definitions are found in Bendat and Piersol (4). Some of the less familiar definitions which are used to characterize sediment topography are presented here. A power spectral density function G displays the spatial (or temporal) record of a physical process in its wave number (or frequency) components. The monents of a ripple number power spectral density distribution are used to objectively define characteristic length scales. The ripple number k is defined as the reciprocal of the bedform length. That is

$$k = 1/\lambda . \qquad 2.1$$

The i^{th} moment M_i of a ripple number power spectral density distribution is defined as

$$M_i = \int_k G(k)\, k^i \, dk. \qquad 2.2$$

The characteristic length scale L_1 was defined by Nordin (43) as the reciprocal of the ripple number corresponding to the centroid of the ripple number power spectral density distribution. This is mathematically expressed as

$$L_1 = \left(\frac{M_0}{M_1} \right). \qquad 2.3$$

Rice (46) and Longuet-Higgins (34) showed that for a stationary Gaussian process, L_2 is equal to an average wavelength. The value of the characteristic length scale L_2 is

$$L_2 = \left(\frac{M_o}{M_2}\right)^{1/2} . \qquad 2.4$$

Jain (26) calculated L_2 values from laboratory data for steady open channel flows. The results showed that L_2 is related to the Froude number and flow depth.

The width Δ of a power spectral density distribution is defined as

$$\Delta = \left(\frac{M_o M_4 - M_2^2}{M_o M_4}\right)^{1/2} . \qquad 2.5$$

For a stationary Gaussian process, the probability density distribution pd of the height of the local nondimensional maximum elevations η_o is a function of M_o and Δ. The local nondimensional maximum elevation is defined as

$$\eta_o = \frac{\eta_m}{M_o} . \qquad 2.6$$

As Δ approaches zero, the spectrum becomes infinitely narrow and a Rayleigh probability density distribution is approached for η_o. A Rayleigh distribution is expressed as

$$\begin{aligned} pd\ (\eta_o) &= \eta_o\ e(\tfrac{-\eta_o}{2}) && \eta_o > 0 \\ &= 0 && \eta_o < 0 . \qquad 2.7 \end{aligned}$$

As Δ approaches one, the probability density distribution for η_o becomes Gaussian and the spectrum is broader. A Gaussian distribution is expressed as

$$pd\ (\eta_o) = (\frac{1}{2\pi})^{1/2}\ e^{-\frac{|\eta_o|}{2}} \qquad -\infty<\eta_o<\infty\ . \qquad 2.8$$

The spectral width and the resulting distributions were derived by Rice (46), discussed in detail by Cartwright and Longuet-Higgins (8), and further reviewed by Nordin (43). Experiments conducted by Jain (26) showed that for the topographic features generated by a steady uniform open channel flows, Δ approached one.

As the wave number increases, a power spectral density distribution may obtain a maximum value and then decay. For these conditions, the segment of the spectrum with wave numbers greater than the wave number for the maximum are referred to as the equilibrium range. A fully developed topographic form is one whose profile is limited by some "critical" angle. The critical angle for sediments is the angle of repose θ. By using dimensional analysis, Hino (18) proposed a "minus three power law" for the equilibrium range of the spectrum corresponding to fully developed bed forms. The minus three power law can be applied more generally. It has been successfully applied to fully developed gravity waves by Phillips (44) and to fully developed capillary waves by Phillips (45). In fact, dimensional analysis shows that the equilibrium range of any fully developed two dimensional random height distribution obeys a minus four power law. This implies that a one dimensional distribution obeys a minus three power law. Hino (18) further proposed that the equilibrium range of the spectrum for fully developed bedforms has the form

$$G(k) = C(\theta)k^{-3} \qquad 2.9$$

where the coefficient $C(\theta)$ is a function of θ only. Recently, the results by Jain (26), which included the experimental data obtained by Nordin (43) and Ashida and Tanaka (2), demonstrated that the equilibrium range of the spectra for fully developed bedforms does obey a minus three power law. One can also use this data to show that for the grain size range of 0.24 to 0.73 mm, the coefficient $C(\theta)$ is a function of the flow parameters.

All the previous results were obtained for steady uniform open channel flows. The knowledge of bed topographic features generated by gravity waves is less advanced. To date, no diagram relating the bed form classes to the fluid and sediment characteristics is known to exist.

Carsten et al. (6) simulated progressive wave flow over a non-cohesive bed in a laboratory study performed in a U-shaped tank. The oscillatory velocity was generated by a piston in one of the vertical sections of the tank. A dimensional analysis showed that for a given sediment, the ripple length was a function of the orbital excursion length of a water particle at the top of the bottom boundary layer and to the wave frequency. These experiments were conducted at a constant frequency. The results showed that for an orbital excursion length/grain diameter less than 1000, the ripple length was linearly related to the orbital excursion length, but at values greater than 1000, the ripple length was constant. Mogridge and Kamphuis (41), used a U-shaped tank to extend the experiment performed by Cartsten et al. (6) to include the effect of wave frequency. The experimental results showed that when the grain size diameter to orbital excursion length was less than 1000, the ripple length to orbital excursion length ratio varied linearly with the wave frequency.

Studies of the bed topography generated by combined current and wave conditions were performed by both Inman and Harms. Inman (23) conducted field observations of the bed topography in the offshore region adjacent to La Jolla, California. Ripple lengths were measured in water depths ranging from 6 to 23 m. The study showed that the grain size was the most significant parameter determining ripple length. In general, longer ripple lengths were associated with larger grain sizes. However, for a particular grain size, as the water velocity increased, the ripple length increased to a maximum value and then it decreased.

Harms (16) formalized the concept that ripple geometry may be used to determine the relative magnitude of the wave orbital velocity to mean flow velocity for combined wave and steady current conditions. Whereas the ripples produced by waves have a nearly symmetric shape and ripples produced by a mean current have a skewed triangular shape, the ripples produced by combined wave and steady current conditions exhibit a combination of these two geometric shapes. Experimental results showed that the variability of ripple height and length is greater for steady currents than for wave conditions. The experimental results were used to develop a quantitative method for determining the flow condition from the bed topography. However, only three experiments involved wave orbital velocities greater than 3 cm/sec, so the quantitative scheme relating bed topographies to flow conditions is highly subjective.

Neither of these studies applied statistical methods to relate ripple number spectral characteristics or bed elevation probability density distributions to the flow field. Furthermore, no relationship between the flow field and the sediment transport rate was developed.

2.3 Sediment Transport

The total sediment load is defined as the sum of all the sediment which is transported. The sediment discharge Q is defined as the net sediment load transported through a specified cross sectional area per unit time. The net load transported per unit channel width per unit time represents the unit sediment discharge Q_N. The ability to accurately predict the unit sediment discharge for a broad range of steady uniform open channel flows by a single equation has not yet been developed. Classical theories for bedload transport rates have been developed by researchers such as DuBoys (12), who related the unit discharge to the bottom shear stress; Einstein (13), who employed statistical methods to predict the unit discharge; and Colby and Hembree (9), who related the unit discharge to the mean fluid velocity and the water depth. Comparing the range of validity of bedload sediment transport equations with regard to laboratory and field data, Vanoni (54) concluded that the unit sediment discharge can be related to the flow field best by an equation of the form

$$Q_N \propto (\bar{U}h)^p \qquad 2.10$$

where the exponent p has a value between 2 and 3.

Recently, Jain and Kennedy (27) used bed form spectra to determine the coefficients in the sediment transport equation which was employed by Kennedy (28) to predict the bed form class generated by steady uniform open channel flows. However, no sediment transport data is known to exist which demonstrates the accuracy of the proposed sediment transport equation.

Yang (56) applied the stream power concept to predict the suspended sediment transport for sediments with a grain size range of 0.062 to 2 mm in uniform open channel flows. For this process the unit stream power was defined as the time rate of potential energy expenditure per unit weight of water. The constants necessary to relate the stream power to the sediment discharge were obtained from an extensive experimental and field data set which is referenced by Yang (56). The final equation accurately predicted the sediment discharge measured by Vanoni (54) for the Niobrana River near Cody, Nebraska.

Gravity wave motions generating sediment transport in the offshore region and in laboratory tanks can be approximated by small amplitude wave theory. It is instructive to review the results of that theory which are relevant to the dynamic sediment processes. The following expressions are found in texts, such as Phillips (45), which investigate gravity wave theory. The relationships which are presented assume a coordinate system like the one presented in Figure 1. A monochromatic gravity wave is represented as ζ where

$$\zeta = a \cos (k_w x - ft) . \qquad 2.11$$

The value "a" represents the maximum displacement of ζ. The angular wave number k_w and the angular wave frequency f are defined as

$$k_w = 2\Pi/L \qquad 2.12$$

and

$$f = 2\Pi/T . \qquad 2.13$$

The fluid velocity field over a flat impermeable bed has been decomposed into a surface boundary layer, an inviscid interior, and a bottom boundary layer. For a laminar bottom boundary layer, the boundary layer thickness δ according to Phillips (45) is

$$\delta = \left(\frac{2\nu}{f}\right)^{1/2} \tag{2.14}$$

where ν is the kinematic viscosity of the fluid.

The periodic orbital velocity u' at the top of the bottom boundary layer according to Phillips (45) is

$$u' = \frac{af}{\sinh\,(k_w h)} \cos(k_w x - ft)\,. \tag{2.15}$$

The maximum value of u' defines the characteristic orbital velocity U'.

Longuet-Higgins (33) and Huang (22) investigated the mass transport velocity induced by small amplitude gravity waves. Although the theories differed with regard to the mass transport velocity at the free surface and interior regions, they produced a similar results for the mass transport velocity in the bottom boundary layer. The theories showed that there is always a positive (in the direction of wave propagation) mass transport velocity in the bottom boundary layer and a flow reversal in the interior. The mass transport velocity $\bar{U}_o$ at the top of the bottom boundary layer defines a characteristic velocity which is

$$\bar{U}_o = \frac{5}{4}\,\frac{a^2 f k_w}{\sinh^2 k_w h}\;. \tag{2.16}$$

Longuet-Higgins (33) showed that the mean wave induced stress $\bar{\tau}_o$ at the top of the bottom boundary layer is

$$\bar{\tau}_o = \frac{a^2 f^2 k_w \delta}{4\,\sinh^2 k_w h}\;. \tag{2.17}$$

For gravity wave flows or combined current and wave conditions, it is possible to have sediment transported upstream as well as downstream. For these flow conditions, a unit sediment dispersive discharge Q_D is defined as the total load transported through a unit channel width per unit time.

Vincent (55) measured the Q_N produced by gravity waves in a laboratory system. The results show that for laminar bottom boundary layers

$$Q_N \propto (U')^6 \; . \tag{2.18}$$

Vincent was aware of the two velocity scales $\bar{U}_o'$ and U'. Indeed, he presented a review of gravity wave theory similar to that presented in this report. A relationship similar to Equation 2.18 but relating Q_N to $\bar{U}_o$ would have been more physically meaningful.

Bagnold (3) proposed a theory for the net immersed weight sediment transport rate per unit channel width per unit time generated by a combined wave and steady current flow field. This transport rate, i, was related to Q_N as

$$i = \left(\frac{\rho_s - \rho_f}{\rho_s}\right) g Q_N \; . \tag{2.19}$$

The theory predicted that the transport rate is related to the flow field as

$$i = K \, \bar{w} \, \frac{\bar{U}}{U'} \; . \tag{2.20}$$

The symbol K represents a proportionality constant and the variable $\bar{w}$ represents the decrement in the transmitted wave power due to bed drag. The basic concept behind the theory is that the wave motion produces the stress which is necessary to induce sediment motion and the mean current is responsible for the net transport. The quantity $\bar{w}/U'$ has the units of a stress and can be considered as the wave induced shear stress. With this representation, $(\bar{w}/U')\cdot\bar{U}$ is another statement of the stream power concept.

Inman and Bowen (25) performed a laboratory investigation of the sediment transport generated by combined flows simulating the flow field in the offshore region of the continental shelf. The decrement of wave power was computed from a measurement of the decrease in wave amplitude as it propagated over the sand bed. The experimental results produced too much scatter to confirm the theory proposed by Bagnold (3) and the broad range of transport rates that was measured has never been adequately explained. One source of error in the transport rates which Inman and Bowen (25) measured was wave reflections which were observed in the laboratory system but not measured. Longuet-Higgins (33) investigated the bottom boundary layer flow for the condition of total reflection and concluded that when small amplitude waves propagate in a fluid with a constant depth and the bottom boundary layer is laminar, a flow reversal is generated in the bottom boundary layer during part of the wave period. Since Carter *et al.* (7) established that the critical reflection coefficient below which no flow reversal occurs is 0.4, laboratory systems should be designed to minimize wave reflections.

Inman and Bagnold (24) proposed a method for computing the longshore sediment transport in the surfzone based on a stream power theory developed by Bagnold (3). Komar and Inman (30) presented field data for the longshore sediment transport in the surfzone which confirmed the validity of the method.

In summary, sedimentary topographic features and transport rates are a function of the generating flow field and the sediment characteristics. Numerous investigations have been performed which relate these processes to various flow fields and sedimentary conditions. However, no investigation has been performed which quantitatively relates both the topographic features and the transport rates to the flow field. In particular neither of these relationships exist for the combined steady current and wave conditions which can be found in the offshore regions of the continental shelves. In these regions it is difficult to measure the transport rates, but photographs of the bottom topography are relatively easy to produce. By quantitatively relating the topographic features and transport rates to the combined flow parameters and quantitatively relating the topographic features to the sediment transport rate, an assortment of methods would be established for predicting the sediment transport rate. This study attempts to determine these relationships for combined steady current and wave conditions in which bedload is the dominant transport mode.

3. EXPERIMENTAL APPARATUS AND PROCEDURES

3.1 Description of the Wave-Current Tank

The wave-current tank used for this investigation is located at North Carolina State University. A scale drawing of the tank is shown in Figure 2. The 15 m tank has a cross sectional area of 60 x 90 cm^2. The tank bottom is steel and the side walls are 1.3 cm glass.

A Berkeley Pump Company centrifugal pump (Model B62RH CWG1750), which is powered by a U. S. Motors motor (Model F-9247-00138), generated a steady current by recirculating water through a Berkeley Pump Company 15 cm clear flow butterfly valve (Model 226), a Rockwell 10 cm rotor gallon register (Model C1-8197), and a 10 cm pipe. The pump intake was located behind the beach sections. The exhaust diffuser was located near the wave paddle.

Waves with a frequency range of 0.0 to 1.87 hertz were generated by a paddle generator. The paddle was powered by a variable speed dynamatic motor (Model M1-100066-0033) which is rated at 5 horsepower for a speed range of 0 to 1680 revolutions per minute. The motor is coupled to a paddle by a Browning A worm gear reducer which has a 15 to 1 reduction ratio. A beach consisting of a series of energy absorbers with a decreasing porosity effectively reduced the reflected wave energy.

Instrument carriages were supported by 1.3 x 1.3 cm^2 steel rails which are located above the edge of either side of the tank. The support system for the parallel rails included the use of hemispherical washers so that the rails were "easily" mounted in a plane parallel to the plane of the bed of the tank. A mobile instrument carriage was

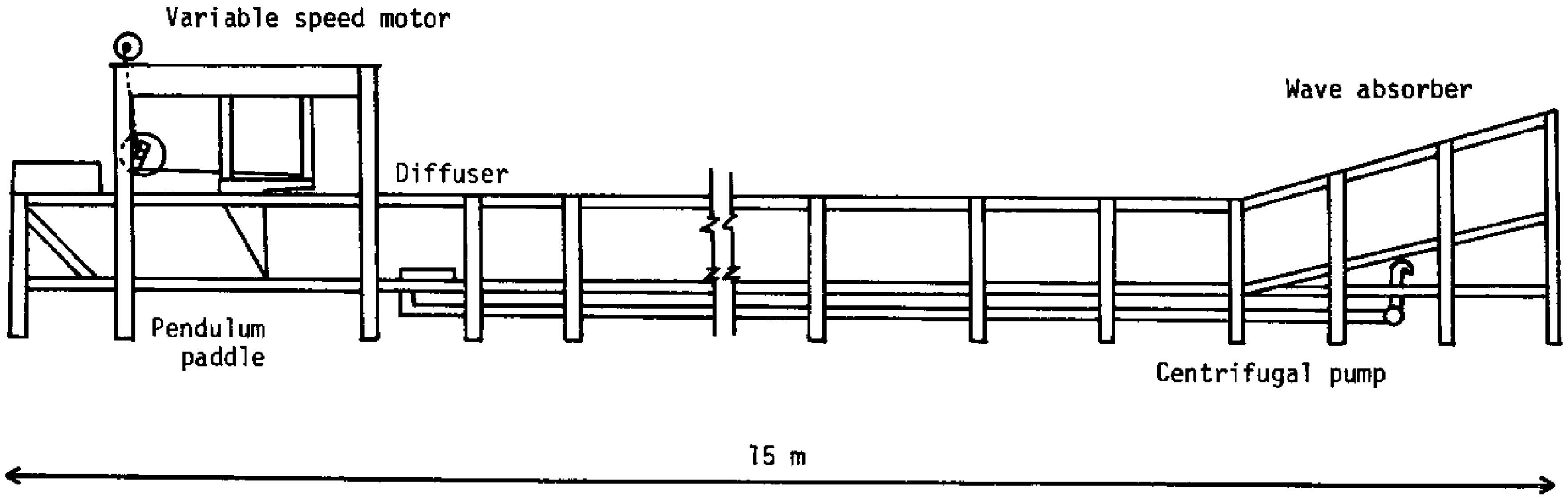

Figure 2. The wave-current tank

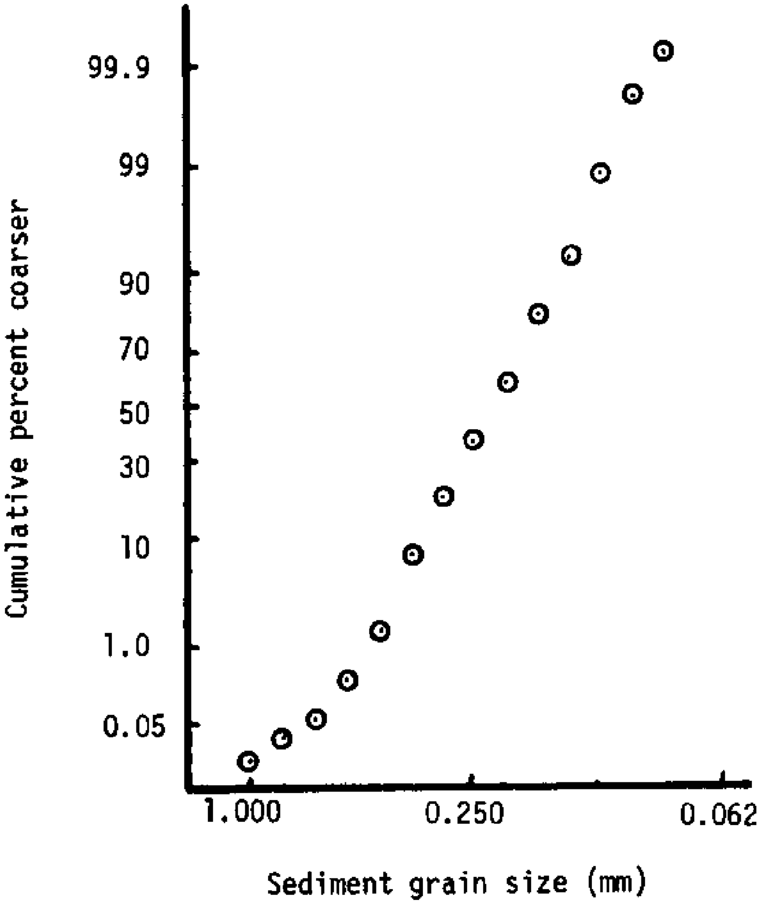

Figure 3. Grain size distribution of experimental sand

propelled by a variable speed motor. By using a 0.6 cm steel cable and a pulley system, the reversing motor drove the carriage along the track at a constant rate in either direction.

The channel bed had a 10 cm layer of sand covering a section 6 m long. At either end of the sand bed, an acrylic ramp with a slope of 1 to 10 made the transition from the tank bottom to 10 cm. The ramps had open ends to that water could flow through the sand that was under them.

The sediment used for the experiments was natural beach sand obtained from above the high water level at Holden Beach, North Carolina. Figure 3 shows the grain size distribution that was obtained from a sieve analyis. According to the definitions presented by Folk (14), the sand, which has a mean size of 0.22 mm with a standard deviation of 0.74 mm, is described as fine, well sorted, near-symmetrical, mesokurtic sand.

3.2 Instrumentation

The fluid velocity field was composed of steady and nonsteady components. In the experimental system, a steady current was produced by a pump which recirculated water. The pumping rate was obtained from data supplied by a gallon register located in the return flow pipe line and a timer.

The nonsteady velocity was due to wave motion generated by a paddle wave generator, free stream turbulence, and boundary induced turbulence. Anemometry was used for measuring the nonsteady fluid velocities. For velocity measurements in an aqueous environment, the use of hot film sensors rather than hot wire sensors has developed primarily because hot film sensors are inherently more rugged. McQuivey (39) showed that the major source of sensor error is electrolysis which can be reduced by applying a thin coat of insulating material over the sensor. The insulation also reduces problems caused by fluid-borne particles. The horizontal velocity probe used in this investigation was built using a hot film sensor, a mounting adhesive, and a protective coating manufactured by Micro-Measurements. The film (Model ETG - 50C) was epoxied (M-bond AE-10) to a 1.3x2.0 cm^2 piece of acrylic and a protective coating (M - coat A) was applied. The sensor was ducted to allow unidirectional velocity measurements. The sensor was activated by a Thermo-Systems anemometer system which consisted of a power supply (Model 1051-2), constant temperature anemometer (Model 1050), signal conditioner (Model 1057), and a linearizer (Model 1055). The probes were calibrated in the North Carolina State University 12x0.6x0.3 m^3 recirculating flume. The mean velocity in the flume was calculated using data from the gallon register in the return flow pipe

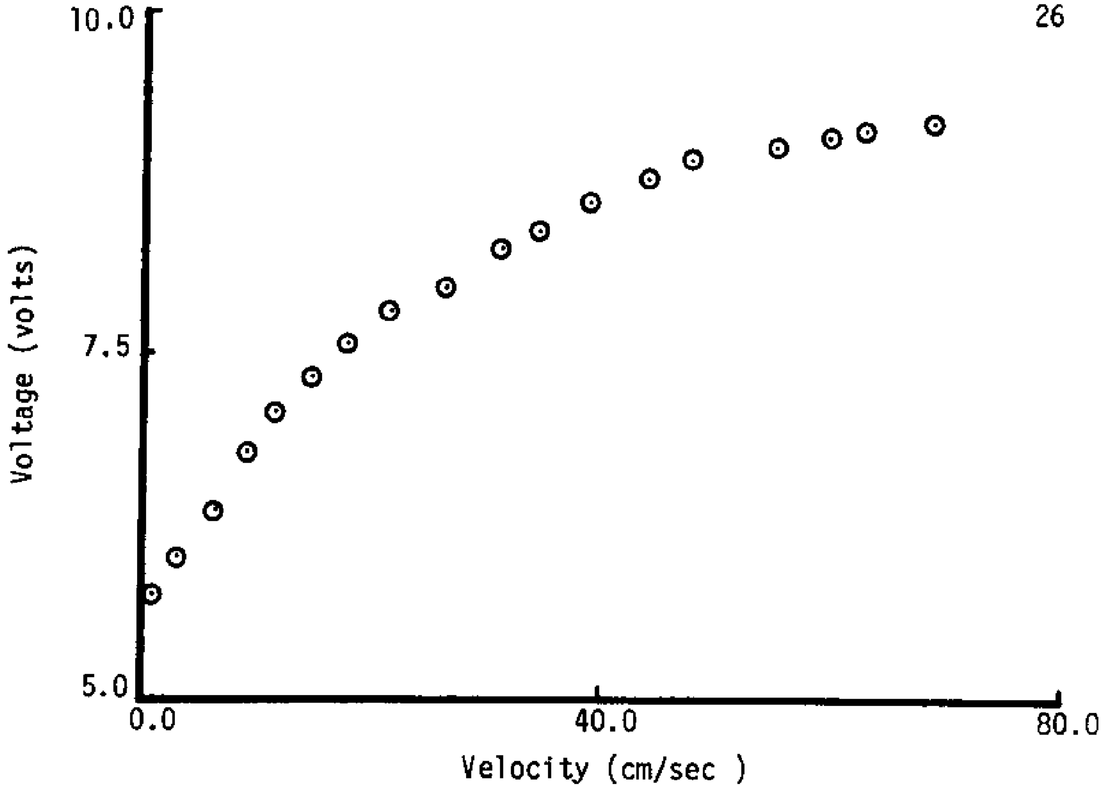

Figure 4. Horizontal velocity probe calibration curve

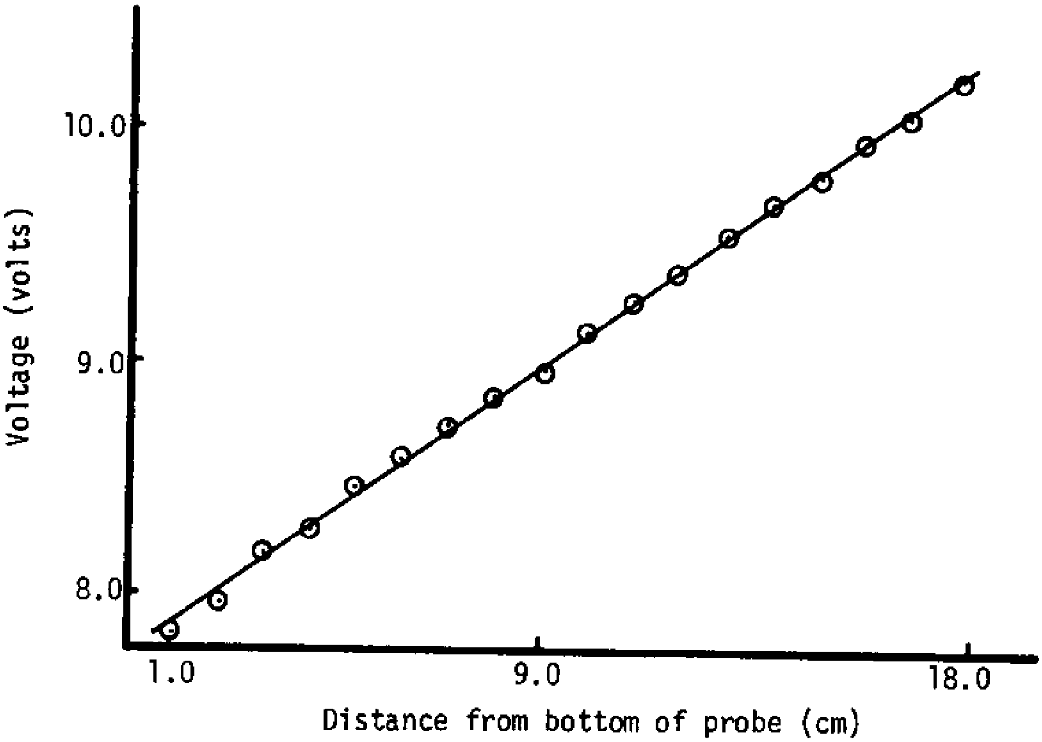

Figure 5. Wave gauge calibration curve

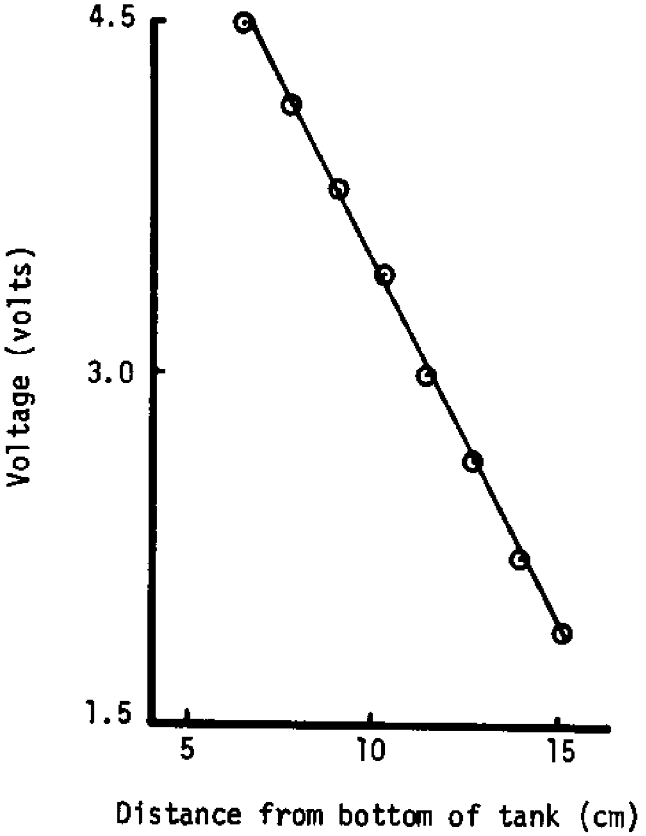

Figure 6. Fathometer calibration curve

and a timer. Figure 4 shows the calibration curve that was established for the horizontal velocity probe and indicates that the relationship between velocity and voltage is nonlinear. The linearizer was employed to make the voltage vary linearly with velocity.

The free surface elevation of the wave motion was measured by capacitance probes that were activated by an electronic device described by McGoldrick (38). The capacitance probe technique was compared to an optical technique by Sturm and Sorrell (50). Their analysis showed that capacitance probes are accurate for wavelengths greater than 5 cm. Since the wavelengths produced during the present investigation were on the order of meters, the capacitance probes achieved acceptable accuracy. One capacitance probe was positioned at a fixed location in the wave tank and it consisted of a taut insulated wire which penetrated the mean water surface at 90° and a ground plate. This probe produced the linear relationahip between voltage and water surface elevation shown in Figure 5. Another probe, which also produced a linear response, consisted of an insulated wire held taut by a steel bow that also acted as the ground terminal. This probe was mounted on the mobile instrument carriage.

The sedimentary parameters that were measured include bed elevation as a function of space and sediment transport. The bed elevation was measured by an Automation Industries ultrasonic distance meter (Model 1050). The probe was calibrated using distances to known elevations above the channel bed. Figure 6 shows that within experimental limits, the distance versus voltage relationship is linear.

The method of tagging sand particles was chosen to measure sediment transport because it simulates the natural processes. Two tracer methods which could have been employed are radioisotopic sand, discussed by Duane (11), and fluorescently dyed sand. The fluorescently dyed sand method was employed for the present investigation for the following reasons: the materials were readily available, no special safety precautions were necessary, and no special electronic equipment was necessary. The method of dying sand proposed by Masterson et al. (35), which is a modified version of the method proposed by McArthur and Rector (36), was employed to dye sand for these experiments.

To measure the sediment transport rates, a dyed sand core was placed in an acrylic trough which contained natural beach sand. Figure 7 displays a cross channel view of the initial sediment distribution in the trough. The trough dimensions were 120 x 9 x 12 cm^3 and the initial dyed core dimensions were 1.27 x 9 x 10 cm^3. During an experiment the trough was centered in the sand bed in the wave current tank. The initially level sediment surface in the trough was at the same elevation as the surrounding sand bed. The trough ends were removed for the duration of the experiment. At the completion of an experiment, the trough was removed from the wave-current tank. Figure 8, which displays a typical front or cross channel view of the sediment distribution in the trough, shows that the final dyed core dimensions were 1.27 x 9 x z cm^3. For the assumptions that (1) bedload was the dominant transport mode, (2) the cross channel transport was negligible, (3) the long channel transport was independent of position, (4) there were no sediment sources or sinks, (5) and that the trough side wall effects on the transport rate were small, the following equations were derived for the sediment transport. The change of elevation Z of the dyed sediment core during an experiment was

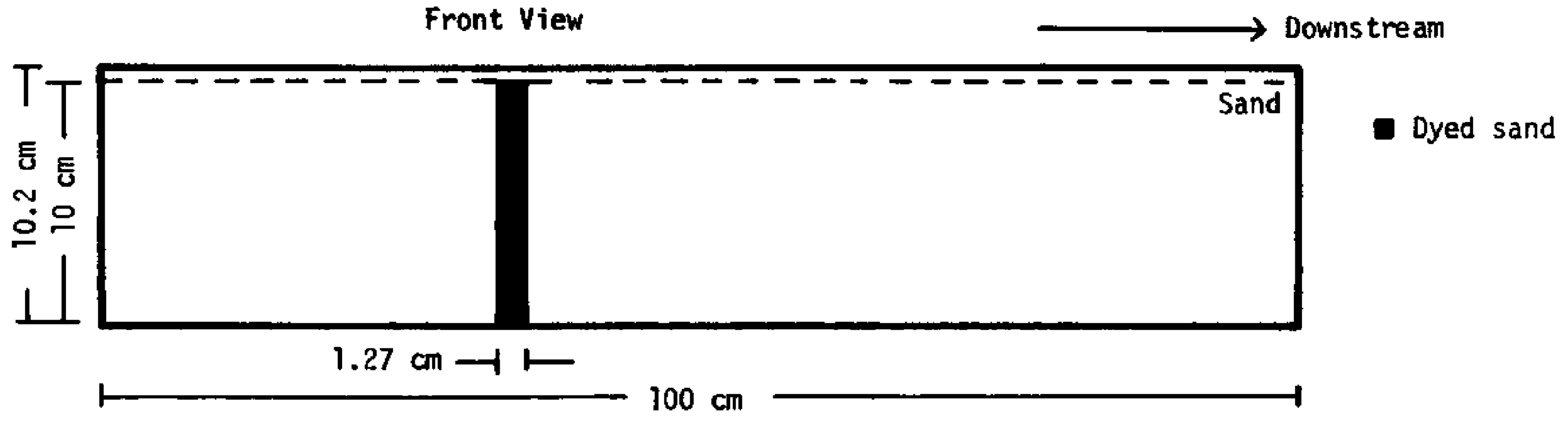

Figure 7. Initial sediment distribution in the sediment trough

Figure 8. A typical final sediment distribution in the sediment trough

$$Z = 10 - z \text{ cm} . \tag{3.1}$$

The front view, i.e. cross channel view, of the dyed sediment distribution in the sediment trough indicated that an area A_c of dyed sediment had been displaced from the original dyed sediment core where

$$A_c = L_c \cdot Z \text{ cm}^2 \tag{3.2}$$

and L_c represents the core length which was 1.27 cm. Thus a volume V_c of dyed sand was displaced for each unit width of channel where

$$V_c = L_c \cdot 1 \cdot Z \text{ cm}^3 \tag{3.3}$$

for a unit channel width of 1 cm.

This displaced dyed sediment was transported upstream and/or downstream so the x-axis was partitioned at 2.50 cm increments. The cross channel view of the displaced dyed sediment distribution showed that associated with each 2.5 cm increment of the x-axis was an area A_i of dyed sediment which had been displaced from the original dyed sediment core. Each dyed area indicated that an increment of sediment volume $\hat{v}_i$ represented by

$$\hat{v}_i = A_i \cdot 1 \text{ cm}^3 \tag{3.4}$$

had been displaced for each unit channel width and each L_c.

The average displacement distance x_i for each $\hat{v}_i$ was measured as the distance between the origin of the x-axis and the midpoint of the appropriate 2.5 cm increment of the x-axis. Since the duration of an experiment was T_e, the mean horizontal speed u_i of each $\hat{v}_i$ was

$$\mu_i = \frac{x_i}{T_e} \quad \frac{cm}{sec} \quad . \tag{3.5}$$

The incremental volume transport rate V_i per unit channel width per unit channel length is equal to the incremental volume transport per unit channel width per unit channel length of the original dyed sediment core multiplied by the average speed of the volume increment. For this investigation this relationship is expressed as

$$V_i = \frac{\hat{v}_i \cdot u_i}{1 \cdot L_c} \quad \frac{cm^2}{sec} \quad . \tag{3.6}$$

Thus the incremental unit mass discharge q_i is

$$q_i = a' \cdot \rho_s \cdot V_i \qquad \frac{gm}{cm\ sec} \tag{3.7}$$

where the constant a' represents a correction factor for the sand pore space. A value of a' for beach deposits was stated by Komar (29) as typically 0.6. The sand was transported upstream for $x_i > 0$ and downstream for $x_i < 0$. The total upstream (downstream) mass transport Q^- (Q^+) per unit channel width per unit time is

$$Q^- = \sum_i q_i \quad \frac{gm}{cm\ sec} \qquad x_i < 0 \tag{3.8}$$

$$Q^+ = \sum_i q_i \quad \frac{gm}{cm\ sec} \qquad x_i > 0 \quad . \tag{3.9}$$

The unit sediment discharge is

$$Q_N = Q^+ - Q^- \qquad \frac{gm}{cm\ sec} \quad . \tag{3.10}$$

3.3 Experimental Procedure

Initially, the wave-current tank contained no water. When the sediment trough had been inserted in the center of the sediment bed and the sand around the trough had been smoothed by raking, a fine jet of water was used to minimize small irregularities. Then the tank was slowly filled with water to the desired height which was measured by a scale mounted on the sidewall of the tank. After recording the gallon register reading and the time, the wave paddle and/or pump were turned on. Simultaneous measurements of the nonsteady velocity and waveheight were obtained over the dyed sediment core and the data was stored on scripchart recordings and magnetic tapes. The wavelength was measured by moving the mobile capacitance probe downstream from the plane of the fixed capacitance probe until the two waveheight signals were again inphase. For several runs, a measurement of the wave field homogeneity was recorded by moving the mobile wave gauge down the channel at a velocity on the order of 0.5 cm/sec. At the conclusion of an experiment, the time and gallon register readings were recorded and a bottom profile was produced by towing the carriage up the channel at a constant velocity. This information was stored on scripchart recordings and magnetic tapes. After slowly draining the tank so as not to disturb the bed forms, the bed was photographed (black and white plus color) in both profile and plane views. Upon removing the sediment trough, profile and plane view photographs were made of the trough while it was illuminated by an ultraviolet light source.

4. THE DATA

4.1 Flow Parameters

Fresh water was used for each experiment to minimize the effects of surface contamination on the wave characteristics. The water temperature was always $18^{+}-2$ degrees Celsius so the kinematic viscosity was approximately constant and equal to 0.01 cm^2/sec. The mean still water depth was approximately 15.2 cm. Table 1 is a tabulation of the numerical values of several flow parameters which varied among the experiments. The methods employed to procure these numerical values follow.

During each experiment, the wave height was recorded on a scripchart and magnetic tape. Figure 9 displays a reproduction of a portion of a typical scripchart wave height record. The angular wave frequencies, f, and the wave amplitudes, a, were obtained from these records.

During each experiment, the nonsteady horizontal velocity 3 cm above the mean bed level was recorded on a scripchart and magnetic tape. Figure 10 displays a reproduction of a typical horizontal velocity scripchart record. The maximum wave velocities at 3 cm above the bed, U', were obtained from these records.

The wavelength, L, was measured and recorded during each experiment. It represents the minimum nonzero separation for which two capacitance probes were inphase.

Small amplitude shallow water wave theory was employed to calculate the maximum horizontal displacement of a water particle from its mean position. This excursion length, L_{ex}, was calculated using

Run	f	a	U'	L	L_{ex}	D_o	D	T_e
	$\frac{1}{sec}$	cm	$\frac{cm}{sec}$	cm	cm	$\frac{cm}{sec}$	$\frac{cm}{sec}$	min
1A	2.28	2.34	17.4	315	7.6	3.4	0.0	120
1B	2.26	2.57	24.3	323	8.6	4.2	0.0	100
1C	2.28	2.51	16.9	338	8.8	4.2	9.3	120
1D	2.26	2.61	20.9	358	9.8	4.9	9.1	120
1E	2.36	1.95	18.2	427	8.7	3.3	23.0	65
1F	2.26	2.06	16.5	384	8.2	3.2	23.3	75
2A	2.59	2.74	22.8	239	6.8	4.0	0.0	60
2B	2.59	3.24	26.7	328	11.0	7.7	11.8	60
2C	2.58	1.92	17.5	350	6.9	2.9	22.1	30
3B	2.98	2.00	14.0	264	5.4	2.7	16.2	78
5A	3.53	2.90	25.5	160	4.6	4.1	0.0	90
5B	3.53	2.96	29.6	278	9.8	7.4	14.3	34
5C	3.58	3.57	29.5	267	8.5	10.5	19.2	33

Table 1. Experimental Flow Parameters.

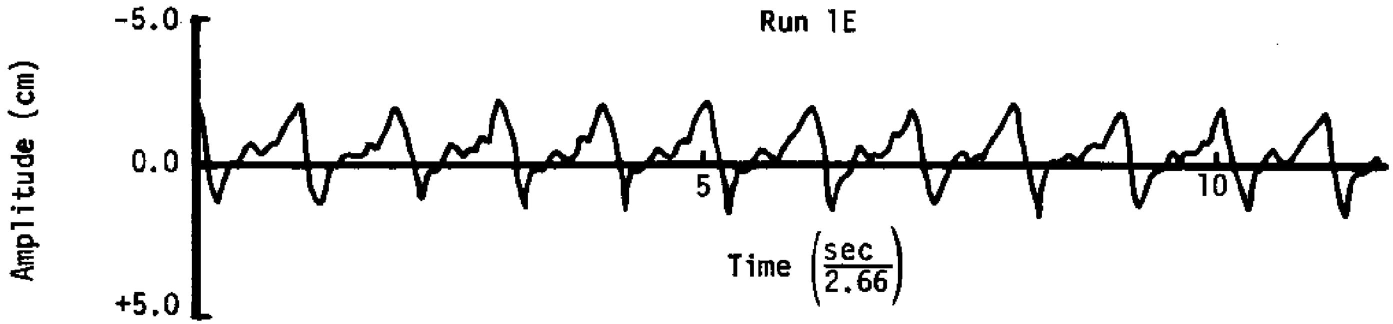

Figure 9. A typical wave height record

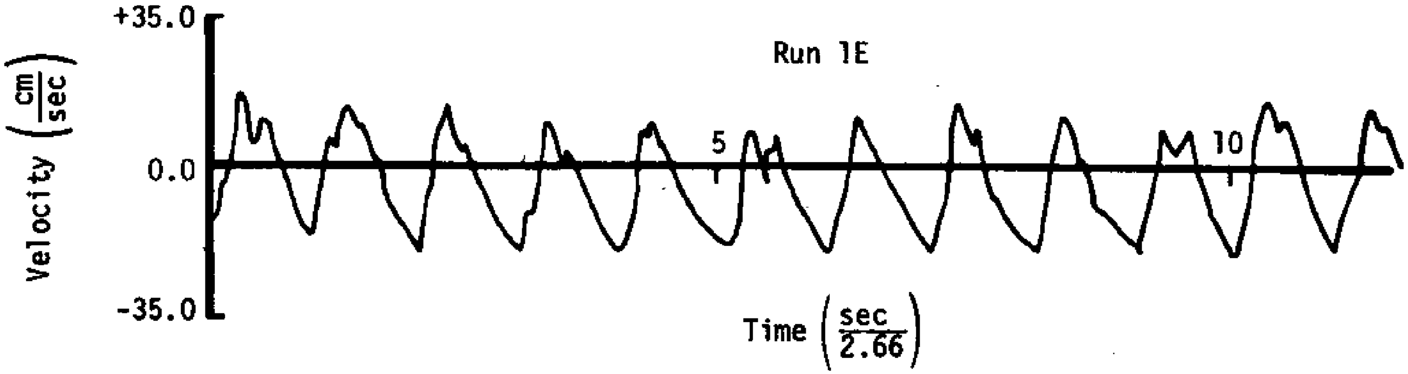

Figure 10. A typical horizontal velocity record 3 cm above the bed

the experimental data and Equation 4.1 from Lamb (32).

$$L_{ex} = \frac{a}{\sinh k_w h} \quad . \tag{4.1}$$

Experimental data and Equation 2.16 were used to calculate the wave induced mass transport velocity, $\bar{U}_o$, at the top of the bottom boundary layer. Equation 2.16 is reproduced here as Equation 4.2.

$$\bar{U}_o = \frac{5}{4} \frac{a^2 f k_w}{\sinh^2 k_w h} \quad . \tag{4.2}$$

The average velocity $\bar{U}$ was calculated from a continuity expression relating the water transport rate through the return flow pipe and the transport rate through the tank test section.

The duration of an experiment, T_e, was measured by a timer and recorded at the conclusion of an experiment.

4.2 Sediment Parameters

The unfiltered tape recordings of the bed topography were processed by a Nicolet correlator (Model UC-202C) to produce probability density and cumulative distributions. These graphs are displayed in Appendix 9.1. The initial sand depth for each experiment was approximately 10.0 cm which defines the datum height represented by 0.0 cm on the graphs. For each distribution, the correlator approximated 3.25 m of analog topography by 3.25×10^7 data points which were sorted into 512 levels. Since the correlator full scale output represented a bed elevation range of ± 25.4 mm, the 512 levels yield a vertical resolution of 0.1 mm. For each experiment, 77 equally spaced points were obtained from the probability density distribution and used to compute the standard deviation $STDV_t$, skewness SK_t, and kurtosis K_t. The subscript "t" is used to emphasize that these parameters correspond to unfiltered data and in the text they are referred to as bed form values. The experimental values are tabulated in Table 2.

Run	$STDV_t$ cm	SK_t	K_t
1A	0.72	0.36	2.22
1B	0.70	0.10	2.59
1C	0.50	0.34	2.35
1D	0.55	0.05	2.90
1E	0.77	0.30	3.02
1F	0.98	0.29	2.26
2A	0.83	-0.36	3.09
2B	0.73	1.01	4.09
2C	1.12	0.65	2.97
3B	1.19	0.15	1.91
5A	1.22	0.32	2.08
5B	0.84	0.44	2.92
5C	0.89	-0.21	3.84

Table 2. Bedform Statistical Measures Obtained From the Bedform Probability Density Distributions.

Ripple number power spectral density distributions were produced for each bed topographic profile by a Nicolet spectral analyser (Model UA-500A-1). The normalized spectral distributions are presented in Appendix 9.2. By averaging 64 spectra, the analyser achieved a normalized statistical error of 12.5 percent for each spectrum. Each of the 64 spectrum represented 1.25 m of analog topographic data by 512 data points so the ripple number resolution is 0.08 mm^{-1}. For each experiment, 91 equally spaced points were obtained from the power spectral density distributions and used to compute the moments of the ripple number spectra tabulated in Table 3.

Run	M_o	M_1	M_2	M_3	M_4
	cm^{-1}	cm^{-2}	cm^{-3}	cm^{-4}	cm^{-5}
1A	9.66	1.66	0.339	0.0789	0.0205
1B	12.63	1.86	0.340	0.0730	0.0180
1C	5.72	0.70	0.117	0.0259	0.0069
1D	10.12	1.55	0.296	0.0667	0.0171
1E	19.85	2.18	0.309	0.0573	0.0134
1F	12.77	1.41	0.204	0.0383	0.0090
2A	8.03	1.21	0.239	0.0566	0.0154
2B	8.55	1.25	0.224	0.0491	0.0127
2C	19.32	2.26	0.354	0.0725	0.0182
3B	10.41	1.20	0.184	0.0363	0.0087
5A	11.96	1.59	0.295	0.0690	0.0189
5B	18.43	2.54	0.421	0.0847	0.0205
5C	16.49	1.67	0.238	0.0467	0.0116

Table 3. Moments of the Ripple Number Spectra.

The area under each spectrum is a measure of the variance $(STDV_r)^2$ for ripples with lengths between 2.5 and 25 cm. These values were calculated using the 91 points from each distribution. Equations 2.3, 2.4, and 2.5 were used to calculate the characteristic length scales L_1 and L_2 and the spectral width Δ. All the parameters calculated from the spectral distributions represent only those bedform with length between 2.5 and 25 cm, so these parameters are referred to as ripple parameters in the text. The experimental values of $STDV_r$, L_1, L_2, and Δ are tabulated in Table 4.

Run	$STDV_r$ cm	L_1 cm	L_2 cm	Δ
1A	0.20	5.82	5.34	0.65
1B	0.22	6.79	6.09	0.70
1C	0.15	8.17	6.99	0.81
1D	0.20	6.53	5.85	0.71
1E	0.28	9.11	8.01	0.80
1F	0.23	9.06	7.91	0.80
2A	0.18	6.64	5.80	0.73
2B	0.18	6.84	6.18	0.73
2C	0.28	8.55	7.39	0.80
3B	0.20	8.68	7.52	0.79
5A	0.20	7.52	6.37	0.79
5B	0.27	7.26	6.62	0.73
5C	0.26	9.87	8.32	0.84

Table 4. Ripple Statistical Measures Obtained From the Ripple Number Power Spectral Density Distributions.

The cross channel view, color slides of the dyed sand distributions in the sediment trough were used to calculate the sediment transport rates. The photographic images were projected on graph paper and the dyed sand distributions were mapped. The A_i areas were computed for 2.5 cm wide vertical columns. The x_i distances were the distance from the dyed sand core to the A_i midpoints. The transport rates Q^-, Q^+, Q_N, and Q_D were computed using Equations 3.8 - 3.11 respectively and are tabulated in Table 5.

Run	Q^-	Q^+	Q_N	Q_D
	$10^{-2} \frac{gm}{cm\ sec}$	$10^{-2} \frac{gm}{cm\ sec}$	$10^{-2} \frac{gm}{cm\ sec}$	$10^{-2} \frac{gm}{cm\ sec}$
1A	0.04	0.11	0.07	0.15
1B	0.04	0.16	0.12	0.20
1C	0.00	0.72	0.72	0.72
1D	0.00	0.55	0.55	0.55
1E	0.01	0.97	0.96	0.98
1F	0.00	0.74	0.74	0.74
2B	0.00	0.82	0.82	0.82
5A	0.31	0.07	-0.24	0.38
5B	0.22	0.95	0.73	1.17
5C	0.00	2.53	2.53	2.53

Table 5. Sediment Transport Rates.

5. ANALYSIS

5.1 General

The bedload sediment transport and topographic features generated by fluid flow fields are a function of both the fluid-sediment boundary layer structure and the response characteristics of the sediment particles to the flow field. Classification of the experimental boundary layers as well as a simple model which yields a characteristic time scale for a moving particle to respond to horizontal velocity variations are presented as an aid to provide a better qualitative understanding of the physical system which existed in the laboratory.

No boundary layer classification method is known to exist for either a wave or a combined wave and steady current flow field over the irregular topography of a mobile, permeable sediment bed. However, for the experimental data, the characteristic height to length ratio of the topographic features will be shown to be small so the beds can be approximated as flat. Furthermore, the effects of mobility and permeability on the boundary layer characteristics are assumed to be small. With these approximations, the boundary layers of the experiments involving only wave induced sediment transport can be classified by a method proposed by Horikawa and Watanabe (21). However, no boundary layer classification method is known to exist for combined wave and steady current conditions. Therefore, characteristic parameters are defined and their experimental values are employed in both a wave boundary layer classification scheme and a steady current boundary layer classification scheme. Finally, the results of the boundary layer classification are summarized.

The progressive wave boundary layer classification scheme which was proposed by Horikawa and Watanabe (21) is employed to classify the boundary layers which developed during the experiments in which progressive waves were the sole mechanism generating sediment transport. The classification scheme is summarized in Table 6. Since the bedform height to length ratios, i.e. $STDV_t$ divided by L_2, are on the order of one-tenth, the bed topography is approximated as flat. The maximum boundary layer thickness was calculated to be 0.94 mm and the mean grain size was 0.22 mm. Thus δ/d was always less than 6.54 which indicates that all the boundary layers were rough. To determine whether a boundary layer is laminar or turbulent, this classification scheme employs the wave Reynolds number, $R_{v\cdot}$, which is defined as

$$R_{U'} = \frac{U' \cdot d}{\nu} . \qquad 5.1$$

Since the experimental values of the wave Reynolds number are less than the critical value of 104, all the boundary layers were laminar.

Smooth: $\delta/d > 6.54$

Laminar: $\frac{U'\cdot\delta}{\nu} < 160$

Turbulent: $\frac{U'\cdot\delta}{\nu} \geq 160$

Rough: $\delta/d < 6.54$

Laminar: $\frac{U'\cdot d}{\nu} < 104$

Turbulent: $\frac{U'\cdot d}{\nu} \geq 104$

Table 6. Progressive Wave Boundary Layer Classification Scheme by Horikawa and Watanabe (21).

The boundary layers which developed during the combined wave and steady current experiments are first classified according to the progressive wave boundary layer classification scheme proposed by Horikawa and Watanabe (21). Again, all the bedform height to length ratios are on the order of one-tenth so a flat bed classification method is employed. Since the boundary layer thickness to grain size ratios were all less than 6.54, all the boundary layers were rough. The peak velocity, u_p, which is defined as

$$u_p = \bar{U} + U' \qquad 5.2$$

is chosen as the characteristic velocity for the combined wave and steady current boundary layer classification and is employed in the wave Reynolds number relationship. The wave Reynolds number is less than the critical value of 104 for all the experiments, except 5C which has a value of 107. Thus this classification method indicates that all the combined flow boundary layers were laminar with the exception of experiment 5C which had a turbulent boundary layer.

The boundary layers of the cobmined wave and steady current experiments can also be classified according to a scheme for steady flows. Experiments by Hegge-Zejnen (17) and Hansen (15) demonstrated that the critical Reynolds number, R_x, for a steady flow over a flat plate is $3 \cdot 10^5$. The Reynolds number for this class of flows is expressed as

$$R_x = \frac{u \cdot x}{\nu} \ . \qquad 5.3$$

For the combined wave and steady current experiments, the characteristic length scale L_2 was on the order of 10 cm and the magnitude of the peak velocity was less than 50 cm/sec, so the maximum value of the Reynolds number is on the order of $5 \cdot 10^4$. Therefore, the steady current boundary layer classification scheme indicates the boundary layers were laminar. For steady laminar flows over flat plates, the experimental results produced by Blassius (5) demonstrated that the boundary layer thickness δ_x is a function of the Reynolds number and the horizontal length scale as defined in Equation 5.4.

$$\delta_x = \frac{5 \cdot x}{R_x} \quad . \qquad 5.4$$

For the experimental values of L_2 and u_p, a minimum boundary layer thickness of 2 mm was calculated. Therefore, δ_{L_2}/d was greater than 10 which indicates that all the beds were smooth.

For the assumptions which have been made, the results of the boundary layer classification are now summarized. (1) During the experiments in which only progressive waves were employed, the boundary layers were rough and laminar. (2) During the combined wave and steady current experiments, the progressive wave boundary layer classification scheme indicates the boundary layers were rough and laminar with the sole exception of experiment 5c which was rough and turbulent. For these same combined wave and steady current experiments, a steady current boundary layer classification scheme indicates the boundary layers were all smooth and liminar.

The motion of a sediment particle obeys Newton's first law which is also known as the law of enertia. Equation 5.5 is an expression relating the horizontal motion of a suspended sediment particle to the net horizontal fluid force D.

$$M_e \frac{du}{dt} = - D \, . \qquad 5.5$$

The variable M_e represents the effective mass of the particle considering buoyancy effects. The solution of this equation which also satisfies the proper boundary condition will define the subsequent motion of a particle for a given situation. The purpose of this exercise is to establish the order of magnitude for the response of a suspended sediment particle to horizontal velocity variations. Since only the order of magnitude of the response time is desired, the following problem will be considered. The sediment particle is represented by a sphere which is moving with an initial velocity u_o relative to the surrounding fluid. What is the subsequent motion of the sphere? An obstacle arises in obtaining a general solution of Equation 5.5 since the functional form of D is a function of the Reynolds number. However, the Stokes drag D_s on a sphere is a valid representation of D for a particle diameter Reynolds number less than 0.2 and it is a fair approximation for a particle diameter Reynolds number less than 500, so a solution will be obtained for this range of Reynolds numbers. The Stokes drag on a sphere according to Schlichting (47) is

$$D_s = 3\Pi \, d\mu u \qquad 5.6$$

where μ is the dynamic viscosity.

Thus the subsequent horizontal motion of a sphere which is initially moving with a velocity u_o with respect to the surrounding fluid is

$$u(t) = u_o \exp \left(-\left(\frac{3\Pi d\mu}{M_e}\right)t\right) \, . \qquad 5.7$$

Finally, the response time t_o is defined as the time for a sphere to reach 0.37 u_o. Since the effective mass of a sphere is

$$M_e = \frac{1}{6} \pi d^3(\rho_s - \rho_f) \qquad 5.8$$

the response time is

$$t_o = \frac{M_e}{3\pi du} = \frac{1}{18} \cdot (\frac{\rho_s - \rho_f}{\rho_f}) \cdot \frac{d^2}{\nu} \quad . \qquad 5.9$$

The quartz sand which was used in the experiments was approximately spherical. Since the largest value of the peak horizontal velocity was approximately 50 cm/sec and the mean grain diameter was 0.22 mm, the grain size Reynolds number was always less than 110. Therefore, t_o is employed to estimate the order of magnitude of the time for the moving sediment particles to respond to velocity variations. This response time was calculated to be approximately 4 milliseconds. Since the wave orbital velocity had a period on the order of 1 second, the moving particles could readily respond to these velocity fluctuations.

5. 2 Dimensional Analysis

No proven analytical equation exists which can predict the topographic features or sediment transport rates produced by a combined wave and steady current flow field in which bedload is the dominant mode of sediment transport. Since experimental data for the topographic features, sediment transport rates, and the flow field has been obtained for combined wave and steady current flows in which bedload was the dominant transport mode, a dimensional analysis is performed to identify the significant nondimensional parameters. The results of the dimensional analysis will be used to investigate the relationships among the topographic features, the sediment transport rates, and the nondimensional parameters. Let any dependent variable which measures a sedimentary feature or process be represented by ψ. To obtain a meaningful dimensional analysis, the relevant sediment and flow field variables must be specified. The sediment variables will be established first. Both a static classification, which is based on the grain diameter, and a dynamic classification, which is based on the grain fall velocity, exist for sediments. Since the sediment transport process is dynamic, the dynamic sediment classification method is employed in this dimensional analysis. To completely specify the sediment characteristics by this method, w, ρ_f, ρ_s, u, g, and Θ must be specified as the independent variables. The angle of repose, Θ, of the sediment is included because this angle limits the development of the topographic features. For sediment particles which are approximately spherical, as is the case for natural sand sized quartz sediment found in the offshore region of the continental shelves and the sediment employed in the present investigation, specifica-

Symbol	Definition	Units	Dimension
w	sediment particle fall velocity	$\frac{m}{sec}$	$\frac{L}{t}$
ρ_f	density of the fluid	$\frac{kg}{m^3}$	$\frac{M}{L^3}$
g	acceleration due to gravity	$\frac{m}{sec^2}$	$\frac{L}{T^2}$
ρ_s	density of the sediment	$\frac{kg}{m^3}$	$\frac{M}{L^3}$
μ	dynamic viscosity of the fluid	$\frac{kg}{m \cdot sec}$	$\frac{M}{L \cdot T}$
h	depth of the fluid	m	L
f	progressive wave angular frequency	$\frac{1}{sec}$	$\frac{1}{T}$
U'	progressive wave orbital velocity at the top of the bottom boundary layer	$\frac{m}{sec}$	$\frac{L}{T}$
$\bar{U}_t$	total mean current; wave mass transport velocity at the top of the bottom boundary layer + the depth averaged steady current velocity	$\frac{m}{sec}$	$\frac{L}{T}$
θ	angle of repose of the sediment	Nondimensional	Nondimensional
ψ	a sedimentary process	$kg^{\alpha 1} \cdot m^{\alpha 2} \cdot sec^{\alpha 3}$	$M^{\alpha 1} \cdot L^{\alpha 2} \cdot T^{\alpha 3}$

α_1, α_2, α_3 specify the appropriate units and dimensions of ψ.

Table 7. Primary Variables for Combined Wave and Steady Current Sedimentary Processes.

tion of ρ_f, ρ_s, μ, and g allows either d or w to be determined when the other one is specified. For practical application, Mitchell (40) has presented a series of equations and graphs which permit the determination of w or d for a wide range of the appropriate variables. Using this method, the fall velocity of the mean grain size of the sediment used in the experimental system was calculated to be 3.2 cm/sec.

Four independent variables are necessary to specify the velocity field at the top of the boundary layer for combined wave and steady current flows. The variables h, f, U', $\bar{U}_t$ are chosen. The flow depth is important in determining whether interactions occur between the free surface of the fluid and the sediment bed. The wave frequency indicates a time scale for the nonsteady processes and variables. At the top of the bottom boundary layer, the wave induced maximum orbital velocity is an order of magnitude larger than the wave induced mass transport velocity. Therefore, the wave induced orbital velocity can be an important mechanism which initiates sediment transport whereas the total mean current $\bar{U}_t$ produces the net sediment transport where

$$\bar{U}_t = \bar{U}_o + \bar{U} \ . \qquad 5.10$$

These eleven independent variables, which are summarized in Table 7, were employed in a Buckingham Pi analysis. The variables represent three dimensions (mass, length, and time) so that with the selection of w, ρ_f, and g as the basic dimensions, eight Pi, Π_i, equations are generated. These equations are:

$$\Pi_1 = \Theta \qquad 5.11$$

$$\Pi_2 = \frac{\rho_s}{\rho_f} \tag{5.12}$$

$$\Pi_3 = \frac{\mu \cdot g}{\rho_f \cdot w^3} \tag{5.13}$$

$$\Pi_4 = \frac{h \cdot g}{w^2} \tag{5.14}$$

$$\Pi_5 = \frac{f \cdot w}{g} \tag{5.15}$$

$$\Pi_6 = \frac{U'}{w} \tag{5.16}$$

$$\Pi_7 = \frac{\bar{U}_t}{w} \tag{5.17}$$

and

$$\Pi_8 = \psi . w^{\alpha 4} . \rho_f^{\ \alpha 5} . g^{\alpha 6} . \tag{5.18}$$

These eight Pi terms specify a functional relationship such that

$$F_o(\psi . w^{\alpha 4} \rho_f^{\ \alpha 5} . g^{\alpha 6}, \Theta, \frac{\rho_s}{\rho_f}, \frac{\mu \cdot g}{\rho_{f \cdot w^3}}, \frac{h \cdot g}{w^2}, \frac{f . w}{g}, \frac{U'}{w}, \frac{\bar{U}_t}{w}) = 0. \tag{5.19}$$

During the experiments, the variables Θ, ρ_s, ρ_f, μ, g, and h were constant so the Pi terms one through four are constant with values of approximately 30 degrees, 2.65, 0.30, and 1450 respectively. The large difference between the experimental value and the real world value of the Π_4 term appears to be the most serious restriction which might limit the range of application of the concepts which will be developed from the experimental data. However, photographs by Komar et al. (31) established the existance of ripples in the offshore region of the continental shelf and ripples were the bedforms generated in the laboratory system. Also, Simons et al. (48) found that there is no interaction between the ripple topography and the free surface of the fluid at small Froude numbers. The largest Froude number for the experiments was small since it was on the order of 0.25. Thus an extension of the concepts derived from the experimental data to similar flow conditions at greater depths should be valid.

The Buckingham Pi theory allows manipulation of the independent varibles. Therefore, to obtain an independent variable which relates the relative magnitude of the total steady current to the orbital wave velocity, the terms U'/w and $\bar{U}_t/w$ were combined to form $(\bar{U}_t/U')^2$. The variable $(\bar{U}_t/U')^2$ will be referred to as the relative flow intensity. As the flow varies from a strictly wave condition, to a combined wave and steady current condition, and finally to a strictly steady current condition, the relative flow intensity varies from $(ak)^2$ to ∞. This entire flow range will be designated as combined flows. The strictly wave conditions and the strictly steady current conditions are subsets of the set of combined flows. The term $\bar{U}_t/w$ is also squared and $(\bar{U}_t/w)^2$ defines the relative mean flow intensity.

Thus the final form of the functional relationship for the sedimentary processes and features generated in the laboratory system is expressed as the function F which appears in Equation 5.20.

$$F(\psi \cdot w^{\alpha 4} \cdot \rho_f^{\alpha 5} \cdot g^{\alpha 6},\ \frac{f \cdot w}{g},\ (\frac{\bar{U}_t}{U'})^2,\ (\frac{\bar{U}_t}{w})^2 = 0\,. \qquad 5.20$$

5.3 Bed Topographic Features

5.3.1 General

Previously investigators frequently used a deterministic approach to characterize the topographic features generated by steady open channel flows or pure gravity wave motions. Since bed topographies are random rather than deterministic, statistical methods must be employed to obtain meaningful quantitative measures of the characteristic parameters. Statistical methods have been employed to quantitatively measure the characteristic parameters of the bedform profiles generated during this investigation. Relationships between the dependent variables and the independent variables developed in the dimensional analysis will be presented.

5.3.2 Ripple Length

The ripple length L_2 is the dependent variable which is used to represent the characteristic ripple length for the experimental data. This length scale is defined as a ratio of moments of the ripple number spectra and if the ripple length is normally distributed, it equals the mean ripple length. Several models are investigated in an attempt to predict the nondimensional ripple length, $L_2 \cdot g/w^2$, as a function of the independent variables.

Figure 11 displays the log-log form of the nondimensional ripple length with respect to the relative mean flow intensity. A positive correlation exists between the variables and 63 per cent of the variation in the nondimensional ripple length is accounted for by the variation in the relative mean flow intensity. The remaining variation of the nondimensional ripple length is not a significant function of the nondimensional frequency.

Figure 12 displays the log-log form of the nondimensional ripple length with respect to the relative flow intensity. A positive correlation exists between the variables and 64 per cent of the variation in the ripple length is accounted for by the variation in the relative flow intensity. The variation due to the different nondimensional frequencies is responsible for some of the remaining difference between the observed values and the simple regression model.

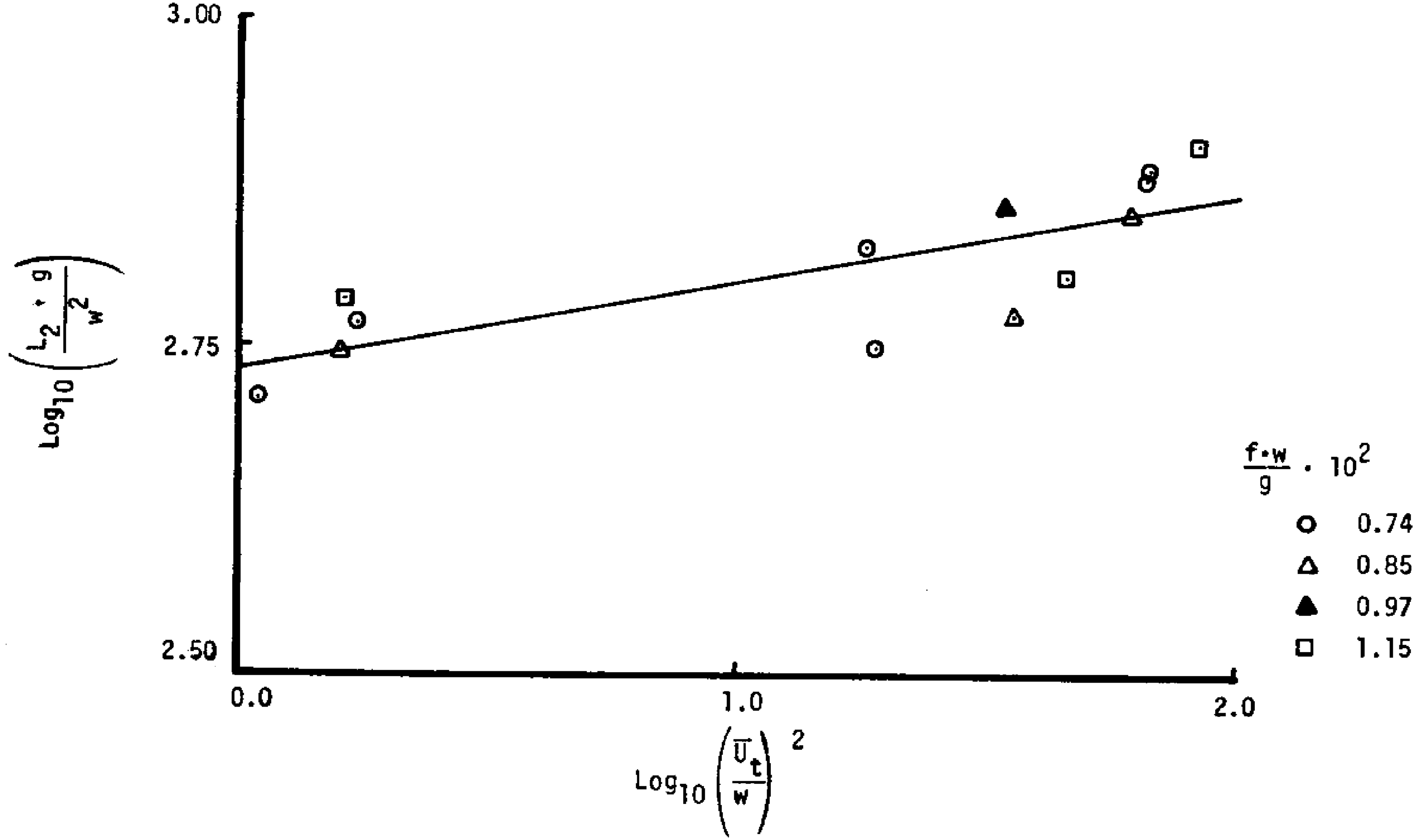

Figure 11. The characteristic ripple length for combined flows as a function of the relative mean flow intensity

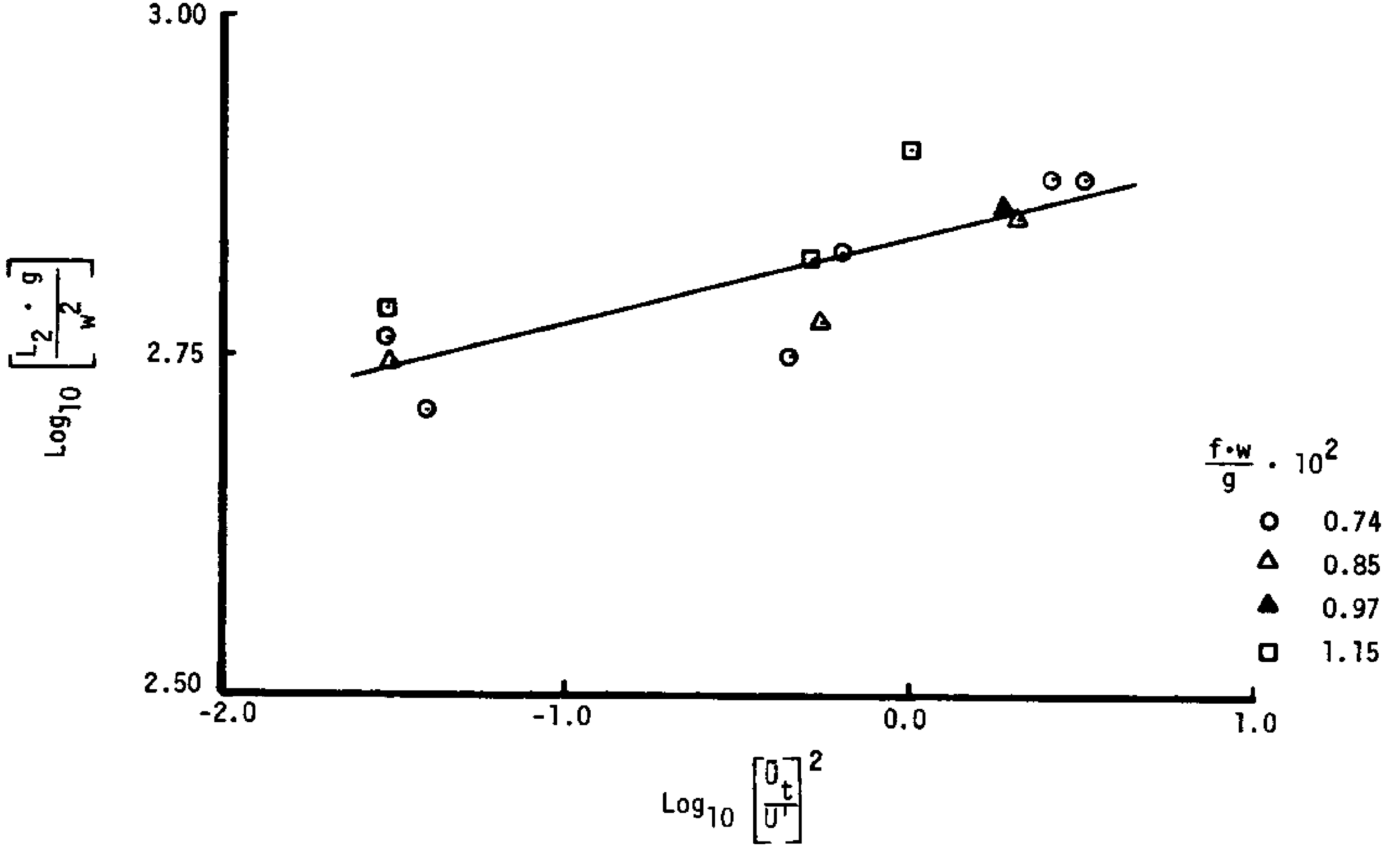

Figure 12. The characteristic ripple length for combined flows as a function of the relative flow intensity

5.3.3 Roughness Amplitude

No consistent relationship exists between the nondimensional ripple amplitude $STDV_r \cdot g/w^2$ and the independent variables.

The relationship between the nondimensional bedform amplitude $STDV_t \cdot g/w^2$ and the nondimensional frequency for the data representing the progressive wave experiments is shown in Figure 13. Since the remaining Pi parameters and g/w^2 were constant, the existing experimental data shows that the bedform height increased linearly with an increase in the wave frequency.

The nondimensional bedform amplitude data for the combined flow experiments is displayed with respect to the relative flow intensity in Figure 14. For a constant value of the relative flow intensity, the nondimensional bedform amplitude increase as the nondimensional wave frequency increases. For constant nondimensional wave frequencies, the nondimensional bedform amplitude decreases before increasing as the relative flow intensity increases.

In section 2.2 the method developed by Rice (46) for specification of the distribution of the local maximum ripple elevation, η_0, from a measurement of the moments of the ripple number spectrum was presented. For Δ equal to 1 (or 0) the distribution of η_0 is Gaussian (or Rayleigh). The values of Δ for the gravity wave experiments are plotted as a function of the nondimensional frequency in Figure 15. This graph shows that for the range of nondimensional frequencies which is presented, Δ increases linearly as the wave frequency increases.

The values of Δ for the combined flow experiments are plotted as a function of the relative flow intensity in Figure 16. This graph shows no consistent functional dependence between Δ and the dimensionless frequency. As the relative flow intensity increased to approximately 2.5, Δ approached 0.80. The investigation by Jain (26) of steady open channel flow bedform topography established that Δ equals one for fully developed bedform spectral distributions. It is apparent that data at larger relative flow intensities is necessary to establish the method in which Δ approaches this limit.

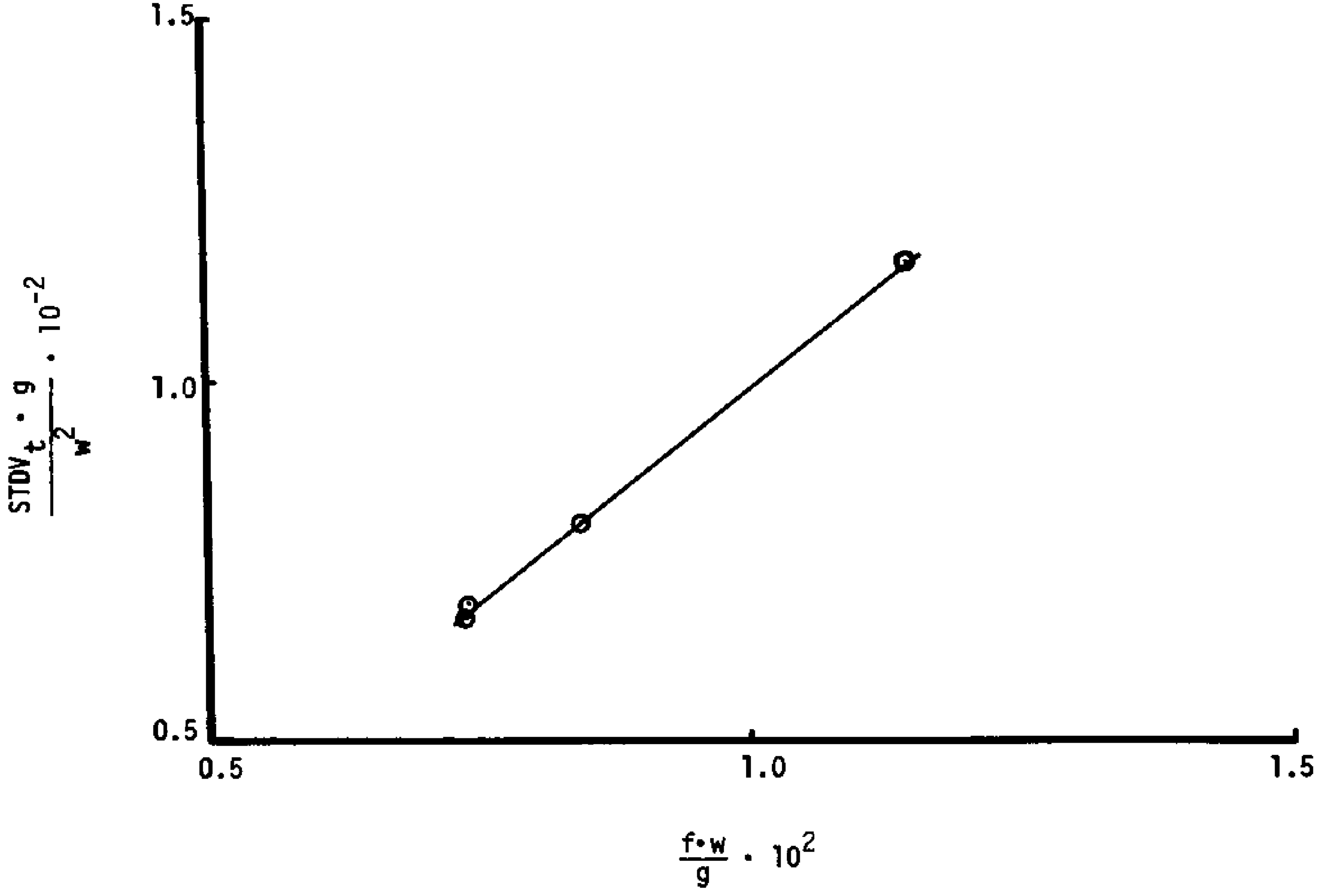

Figure 13. The characteristic bedform amplitude for gravity wave fields

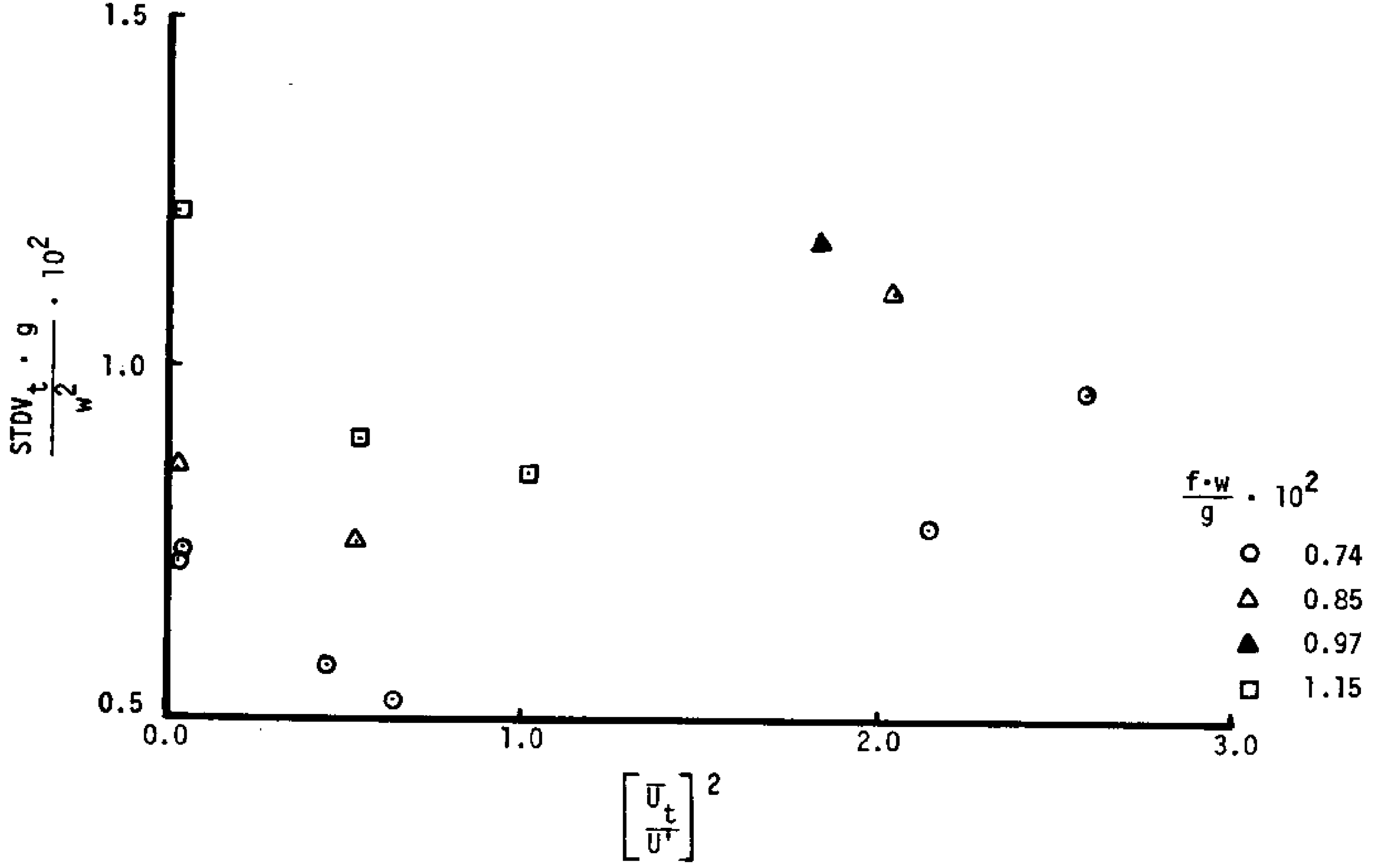

Figure 14. The characteristic bedform amplitude for combined flows

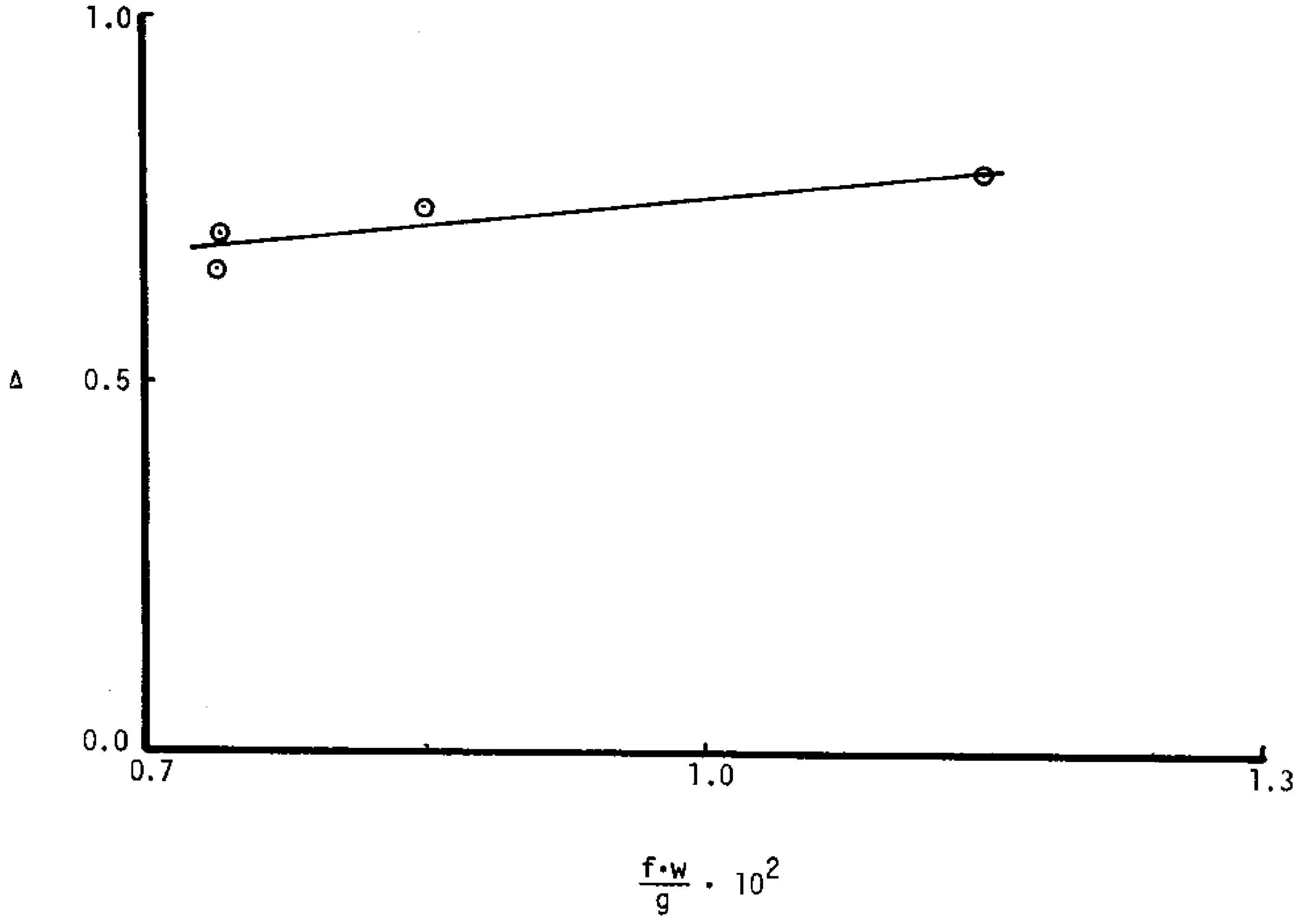

Figure 15. Ripple number spectral width for gravity wave fields

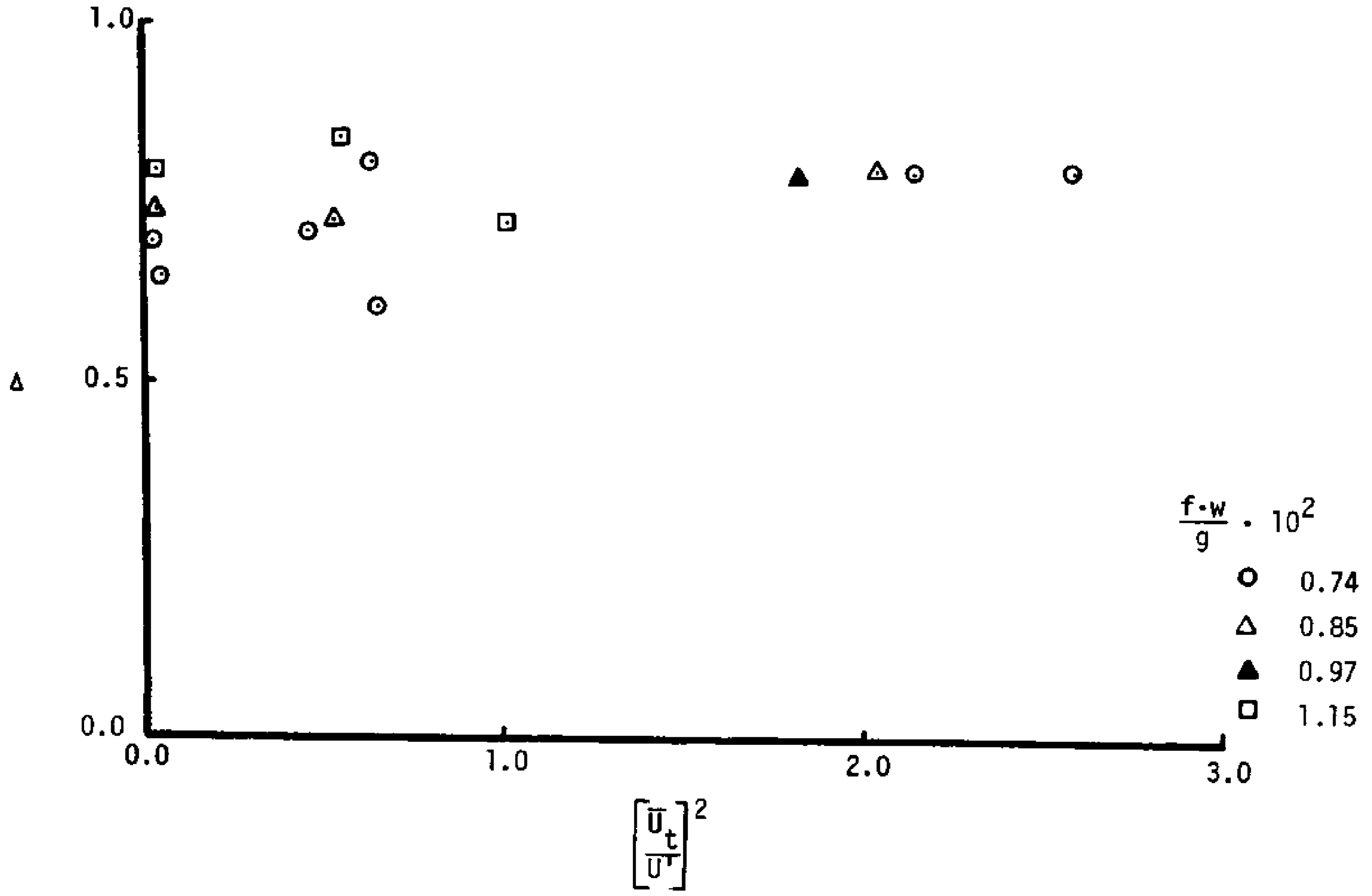

Figure 16. Ripple number spectral width for combined flows

5.3.4 Bedform Kurtosis

Kurtosis is a measure of the peakedness of a probability density distribution. As a standard for comparison, the normal distribution has a kurtosis value of 3.0.

A graph of the bedform kurtosis versus the relative flow intensity is displayed in Figure 17. The mean and standard deviation of the experimental kurtosis values are 2.66 and 0.59 respectively. The graph suggests that the bedform probability density distribution may tend to be platykurtic, i.e. have a kurtosis less than 3.0. The sign test is a statistical method which was employed to test this hypothesis. The sign test can be found in Davies and Goldsmith (10). At the 95 per cent confidence level, the sign test indicates that no significant difference exists between the kurtosis of the bedform and the normal probability density distributions. Therefore, the bedform kurtosis is approximately Gaussian.

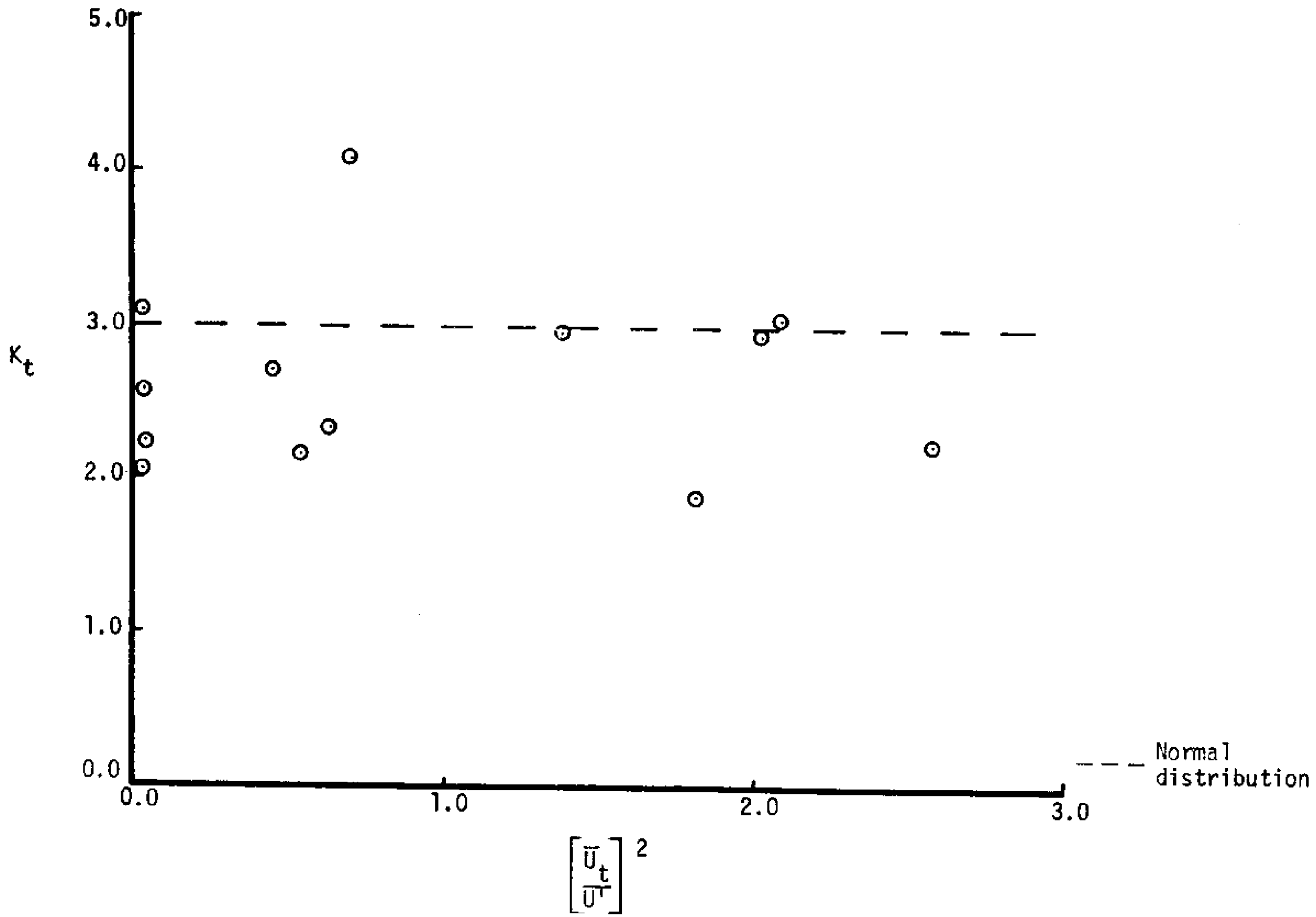

Figure 17. Bedform kurtosis for combined flows

5.3.5 Bedform Skewness

Skewness is a measure of the asymmetry of a probability density distribution. As a standard for comparison, the normal distribution has a skewness of zero.

The skewness of the bedform probability density distributions is plotted as a function of the relative flow intensity in Figure 18. The mean and standard deviation of the experimental skewness values are 0.26 and 0.35 respectively. The data suggests that the bedform skewness may typically be positive which would indicate that the sediment above the mean bed level has more relief than the sediment below the mean bed level. Since 11 of the 13 skewness values are positive, the sign test indicates that the bedform skewness is positive at the 97.5 percent confidence level. This data for bedform skewness quantitatively demonstrates that geologists correctly employ the skewness of bedforms, generated by flow conditions similar to those of the laboratory system, as an aid in interpreting previous depositional environments. For instance, when bedforms exist in a consolidated sedimentary rock, their skewness can establish the orientation of the rock with respect to the free surface of the water at the time when the material was deposited. It can also be used to determine whether the rock represents the original bedform or a cast of the bedform produced by the consolidation of sediment deposited over the original bedform.

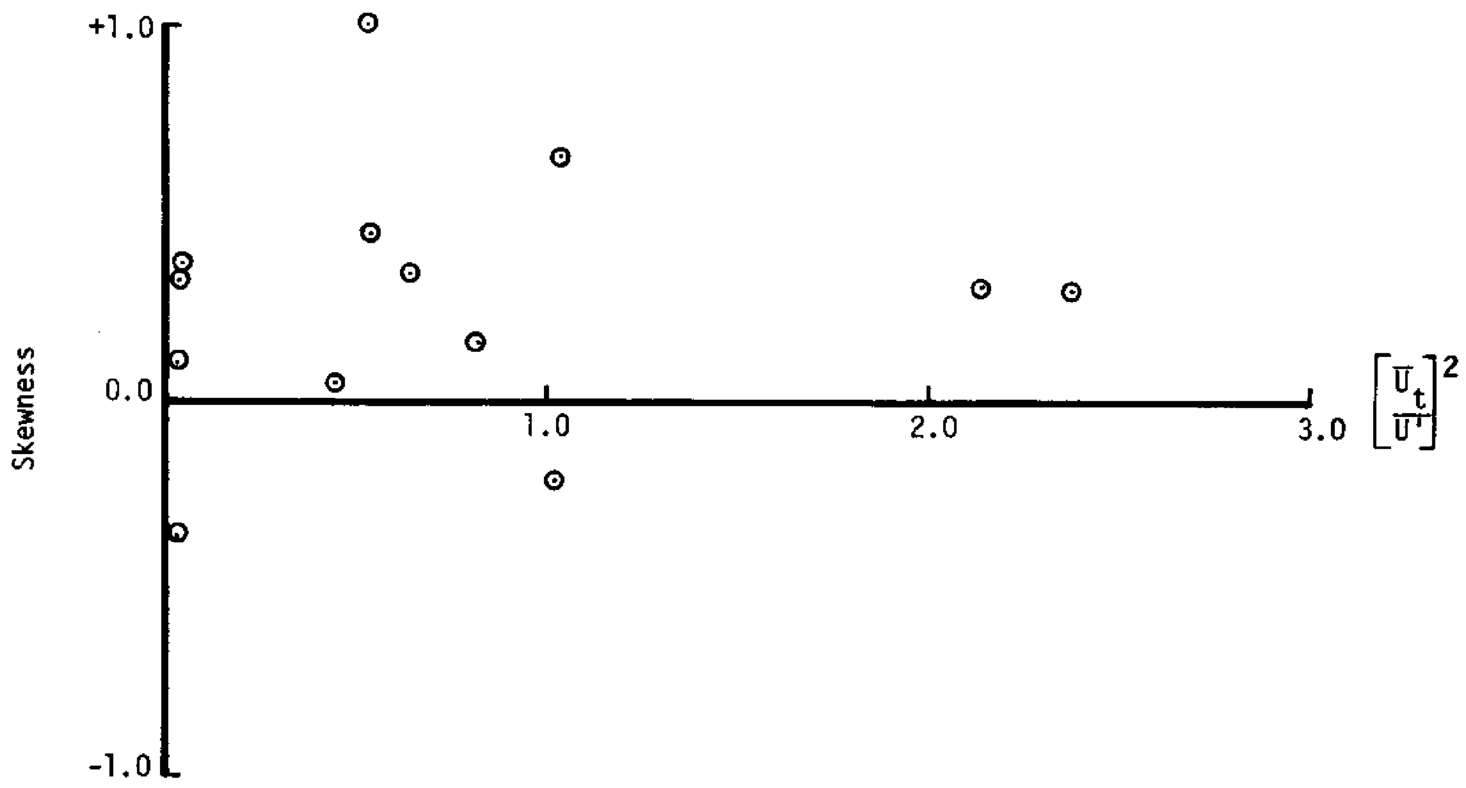

Figure 18. Bedform skewness for combined flows

5.3.6 Equilibrium Range of the Ripple Number Spectra

Fully developed bedforms are bedforms whose size is limited by the angle of repose of the sediment. The work by Hino (18) and Jain (26) established that the equilibrium range of the power spectral density distribution for fully developed bedforms obeys a "minus three power law." Hino further proposed that the constant of proportionality is a function of only the angle of repose. However, the experimental data presented by Jain can be used to demonstrate that the constant of proportionality is also a function of the flow field.

For low flow velocities, it is physically possible that mechanisms other than the angle of repose limit the development of the topographic features. For these low flow conditions, the fluid and sediment processes will establish a local equilibrium condition even though the size of the topographic features is not limited by the angle of repose. As the velocity is increased, the topographic features can continue to develop until their size is limited by the angle of repose, i.e. the bed is fully developed. The equation proposed by Hino (18) to represent the equilibrium range of a fully developed bedform spectrum is

$$G(k) = C(\theta)k^{-3}. \qquad 5.21$$

Clearly a more general expression is needed to represent the equilibrium range of the bedform spectrum for local equilibrium conditions. The dimensional analysis which was presented in section 5.2 suggests that a general form of Equation 5.21 may be expressed as

$$G(k) = C^{*}\, k^{-3+M} \qquad 5.22$$

where

$$C^* = \left(100\,\frac{w^2}{g}\right)^{-M} \quad C\left(\Theta, \frac{\rho_s}{\rho_f}, \frac{\nu g}{w^3}, \frac{hg}{w^2}, \frac{fw}{g}, \left(\frac{\bar{U}_t}{U'}\right)^2, \left(\frac{\bar{U}_t}{w}\right)^2\right) \tag{5.23}$$

and

$$M = \text{fn}\left(\Theta, \frac{\rho_s}{\rho_f}, \frac{\nu g}{w^3}, \frac{hg}{w^2}, \frac{fw}{g}, \left(\frac{\bar{U}_t}{U'}\right)^2, \left(\frac{\bar{U}_t}{w}\right)^2\right) . \tag{5.24}$$

With this representation of the equilibrium range, the relative slope M of the spectrum would be zero when the bed is fully developed. The logic used to choose the factor $100\,w^2/g$ in Equation 5.23 was as follows. The order of magnitude of w^2/g is 0.01 cm. This value raised to the minus M power has a large effect on the value of the equilibrium range coefficient C^* of the nondimensional ripple spectra. However, by employing $100w^2/g$, C^* is a slowly varying function of the flow and sediment characteristics.

During the experiments, several of the Pi values were constant so in the data analysis the general relationship for the equilibrium range spectrum reduces to

$$G(k) = C^*\,k^{-3+M} \tag{5.25}$$

where

$$C^* = \left(100\frac{w^2}{g}\right)^{-M} \quad C\left(\frac{fw}{g}, \left(\frac{\bar{U}_t}{U'}\right)^2, \left(\frac{\bar{U}_t}{w}\right)^2\right) \tag{5.26}$$

and

$$M = \text{fn}\left(\frac{fw}{g}, \left(\frac{\bar{U}_t}{U'}\right)^2, \left(\frac{\bar{U}_t}{w}\right)^2\right) . \tag{5.27}$$

The ripple number spectra are displayed in log-log form in Appendix 9.2. The relative slopes were obtained from these graphs and the values of the equilibrium range coefficients were obtained for k equal to 1.0 cm^{-1}. The equilibrium range coefficients are plotted as a function of the nondimensional frequency for the wave experiments in Figure 19. The graph shows that C^* increased linearly as the nondimensional frequency increased.

The equilibrium range coefficient of the nondimensional ripple spectra for combined flows is plotted as a function of the relative flow intensity in Figure 20. The data shows a decreasing scatter as the relative flow intensity increases.

The relative slope is plotted as a function of the nondimensional frequency for the wave experiments in Figure 21. The data shows that the relative slope is negative for the gravity wave induced topographic features. The value of M increases asymptotically to zero as the nondimensional frequency increases.

The relative slope is plotted as a function of the relative flow intensity for the combined flow experiments in Figure 22. The graph shows that all the values are less than or equal to zero and that as the relative flow intensity increases, the relative slope approaches zero.

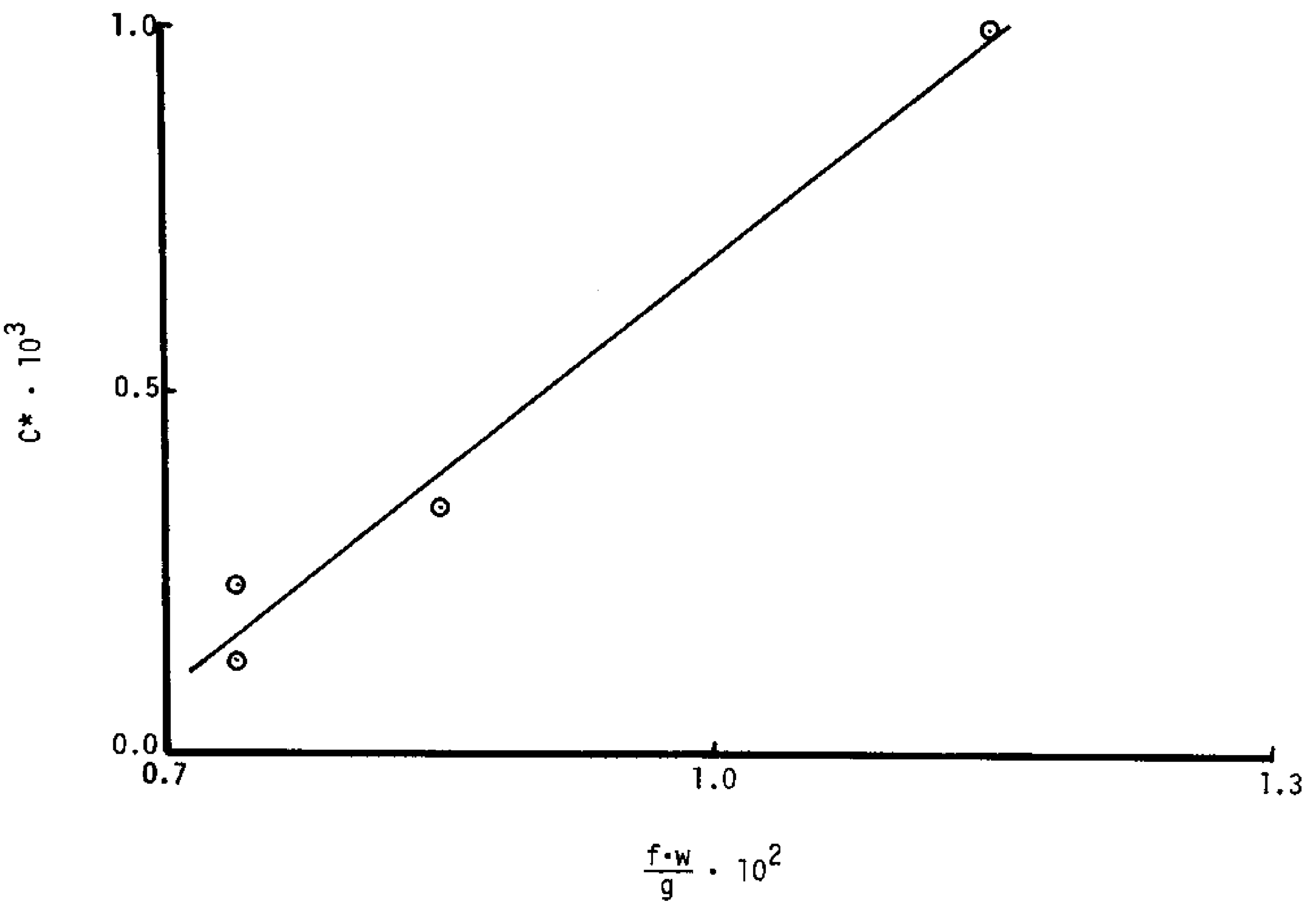

Figure 19. Ripple number equilibrium range coefficient for gravity wave fields

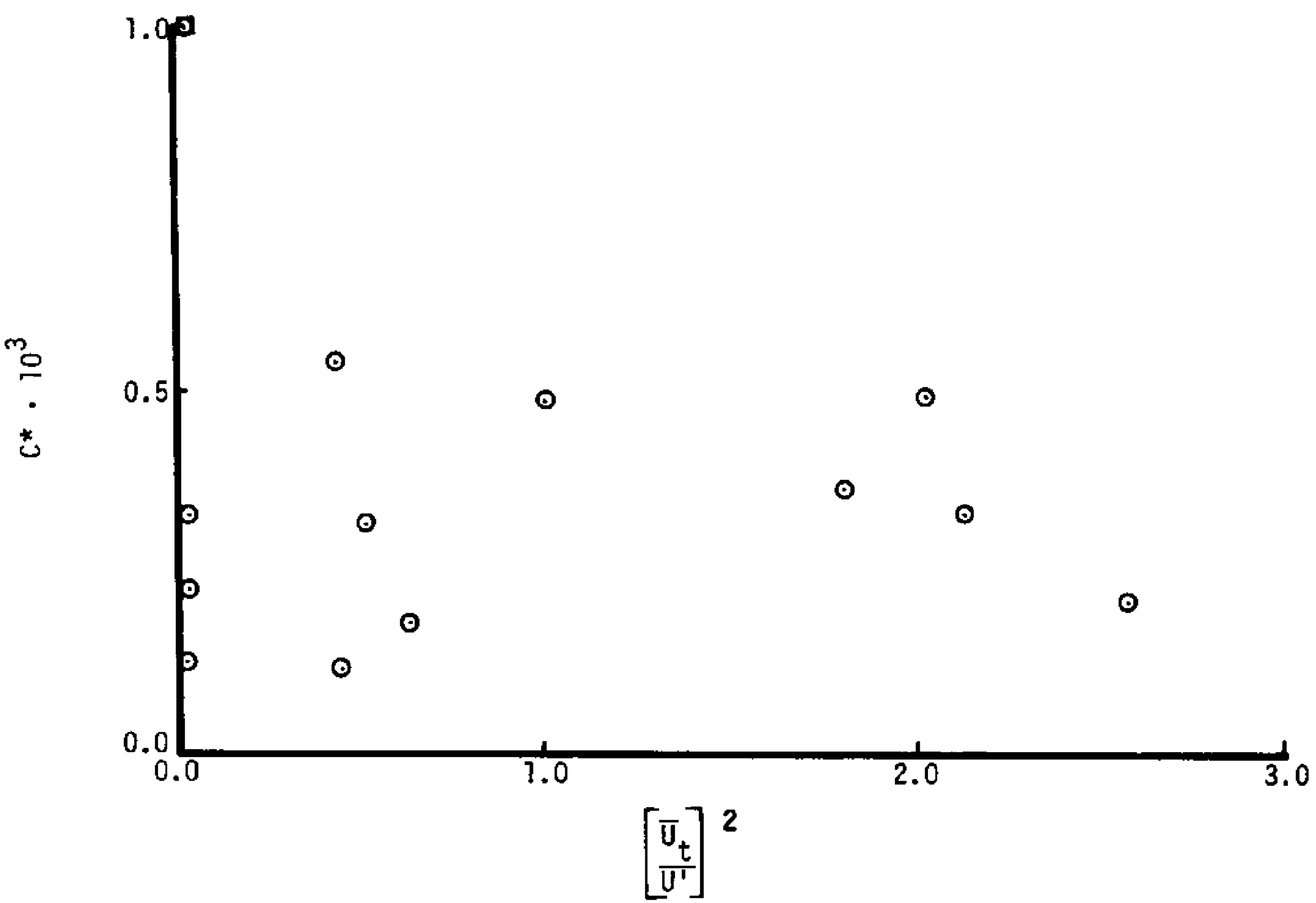

Figure 20. Ripple number equilibrium range coefficient for combined flows

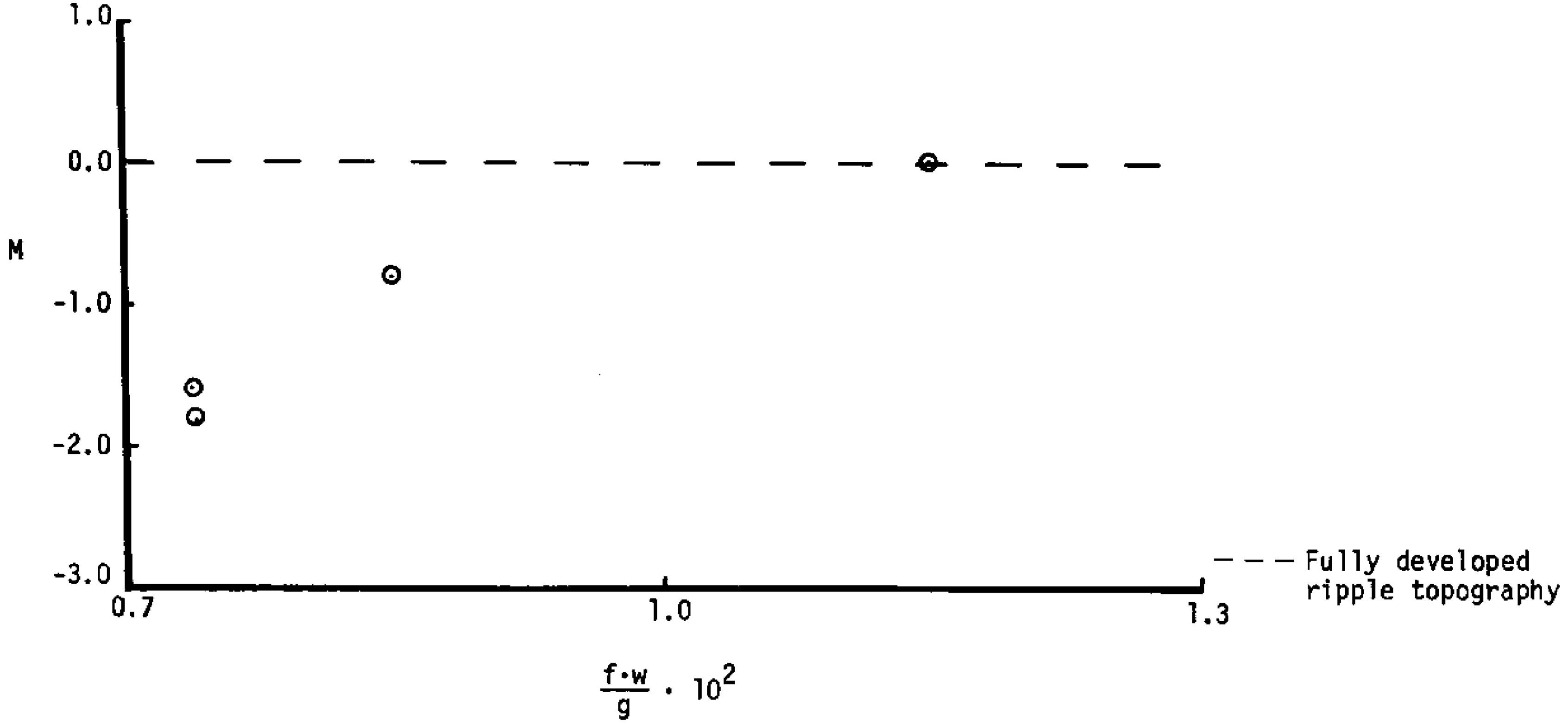

Figure 21. Ripple number equilibrium range relative slope for gravity wave fields

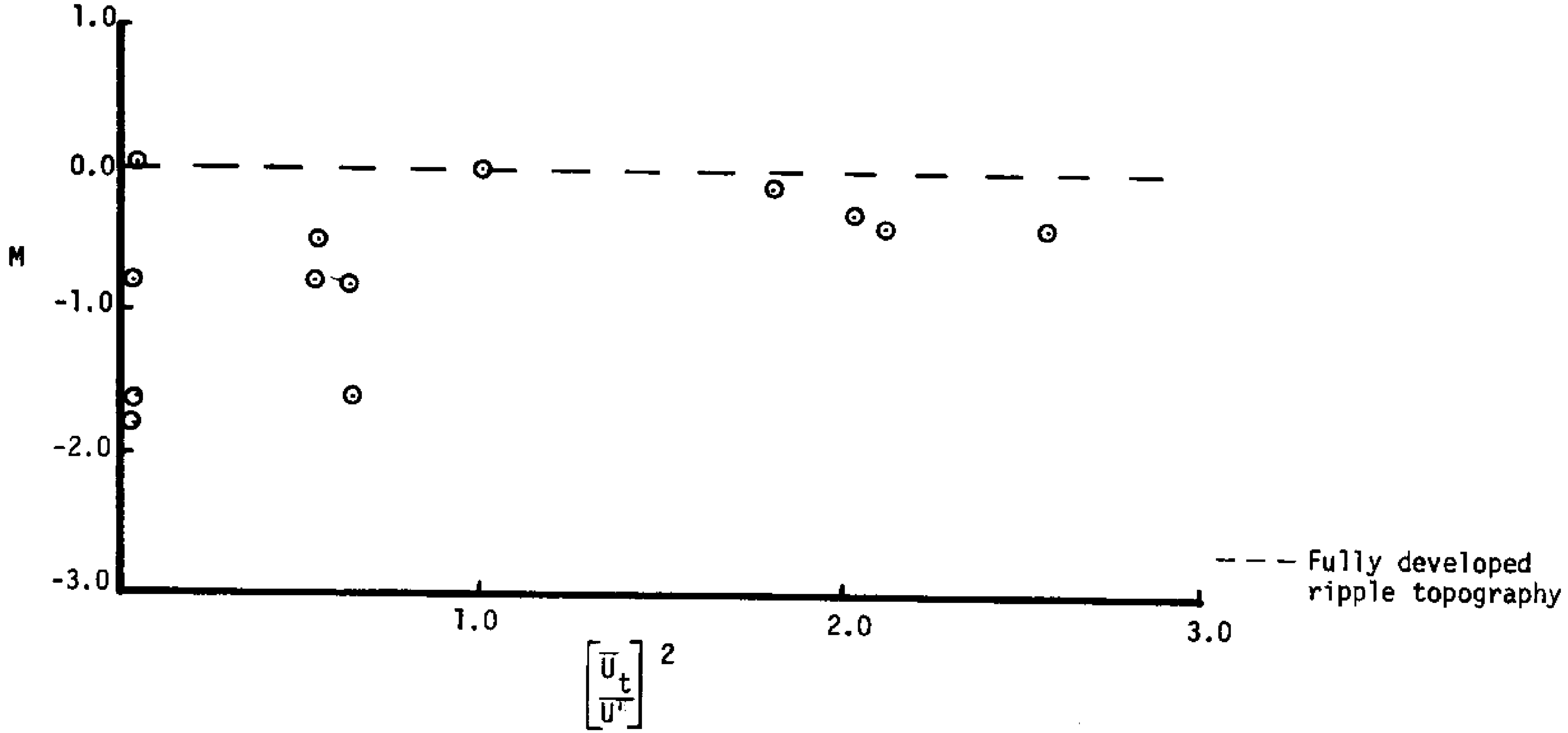

Figure 22. Ripple number equilibrium range relative slope for combined flows

5.4 Sediment Transport

Table 8 presents a tabulation of experimental values of the nondimensional flow parameters and the corresponding nondimensional dispersive and net sediment transport rates obtained during this investigation. In addition, the data obtained by Inman and Bowen (25), hereafter referred to as Inman, for combined flow sediment transport is also presented in the appropriate format in Table 8. In his laboratory experiment, Inman employed quartz sand which had a mean diameter of 0.19 mm and he measured the sediment transport by weighing the sand which was caught in traps at either end of the test section in a wave tank. To present this data in the form which was developed in the dimensional analysis of this text, a fall velocity of 3.2 cm/sec was calculated for the 0.19 mm quartz sand by the method presented by Mitchell (40).

Experiments 4AI and 5A display results that are not expected from a consideration of the theories developed by Longuet-Higgins (33) and Huang (22). These theories predict a positive (in the direction of wave propagation) drift velocity in the bottom boundary layer for small amplitude waves propagating over a flat impermeable bed. Therefore, sand with a dominant bedload transport mode should have a positive net sediment transport when it is generated by combined flows in which the wave and steady current propagate in the same direction. A plausible explanation of the negative net transports is wave reflections. The primary source of wave reflections in laboratory systems is incomplete wave energy absorption by the beach at the end of the tank. Inman noted but did not measure wave reflections. The measured wave reflection

Run	$\frac{f\cdot w}{g}\cdot 10^2$	$(\frac{D_t}{w})^2$	$(\frac{D_t}{U'})^2$	$\frac{h\cdot g}{w^2}\cdot 10^{-3}$	$\frac{Q_N\cdot g}{\rho_f w^3}$	$\frac{Q_D\cdot g}{\rho_f w^3}$
1A	0.74	1.1	0.04	1.45	0.021	0.045
1B	0.74	1.7	0.03	1.45	0.036	0.060
1C	0.74	17.8	0.64	1.45	0.215	0.215
1D	0.74	19.2	0.45	1.45	0.164	0.164
1E	0.74	67.6	2.14	1.45	0.287	0.287
1F	0.74	68.2	2.58	1.45	0.221	0.221
2A	0.85	1.6	0.03	1.45	-	-
2B	0.85	37.1	0.53	1.45	0.245	0.245
2C	0.85	61.2	2.04	1.45	-	-
3B	0.97	34.9	1.82	1.45	-	-
4AI*	1.03	3.1	0.04	4.80	0.105	1.337
4BI	1.03	5.6	0.07	4.80	0.251	1.591
4CI	1.03	9.0	0.10	4.80	-0.033	1.373
4DI	1.03	13.1	0.15	4.80	0.054	1.238
5A	1.15	1.6	0.03	1.45	-0.072	0.114
5B	1.15	46.0	0.54	1.45	0.218	0.350
5C	1.15	86.1	1.01	1.45	0.757	0.757
6AI	1.46	4.8	0.04	4.80	0.359	0.467
6BI	1.46	7.4	0.07	4.80	0.547	0.694
6CI	1.46	11.2	0.11	4.80	0.634	0.736
6DI	1.46	16.0	0.16	4.80	0.374	0.476

*Runs with suffix "I" were obtained by Inman and Bowen (25).

Table 8. Nondimensional Flow Parameters and Nondimensional Transport Rates.

for experiments 1A, 1C, and 1E was approximately 0.12, 0.20, and 0.31 respectively. Unfortunately, the reflection for the other runs was not measured. Since reflected waves probably induced the negative net sediment transports in runs 4AI and 5A, these runs are not included in the analysis.

Although sediment transport may occur as bedload, suspended load, or a combination of bedload and suspended load, the present inquiry is limited to an investigation of sediment transport generated by combined flows which produce bedload as the dominant transport mode. The data incorporated from the study by Inman was generated at two wave frequencies. The lower frequency data set is within the range of frequencies generated during the present investigation. For these experiments, the net transport rates are consistent with those obtained during the present investigation. Except for the flow depth Pi value, the Pi values for the lower frequency data set are similar to the Pi values for the present investigation. The flow depth Pi value in the study by Inman is approximately three times the flow depth Pi value in the present investigation. Since the net sediment transport rate for these experiments are similar, the influence of the flow depth on the net sediment transport rate was small.

The higher wave frequency data set produced by Inman had the highest frequency waves generated in these experimental systems. Inman recorded the presence of suspended sediment. While the other Pi values for this data set are within the range of values established by the remaining frequency data sets, the net sediment transport rate increased significantly with respect to the transport measured at the lower frequencies. This data emphasizes the tremendous increase in the sediment transport rate which can be generated by combined flows which produce suspended sediment transport. Since the sediment transport process associated with the highest wave frequency data set generated significantly greater sediment transport rates than was measured for the remaining data, it is not included in the analysis which follows.

Figure 23 shows the nondimensional net sediment transport rate as a function of the relative flow intensity. For comparison, the data generated by Inman is also plotted on this graph. A regression model shows that the nondimensional net sediment transport rate is related to the relative flow intensity as

$$\log\left(\frac{Q_n \cdot g}{\rho_f \cdot W}\right) = 0.98 \log\left(\frac{U_t}{U'}\right) - 0.49 \qquad 5.28$$

or equivalently as

$$\frac{Q_n \cdot g}{\rho_f \cdot W} = 0.32 \left(\frac{U_t}{U'}\right)^{-0.98} \qquad 5.29$$

with a correlation coefficient of 0.50. Thus for the range of data that was examined, the regression model shows that the net sediment transport rate increased approximately linearly as the relative flow intensity increased.

Figure 24 shows the nondimensional net sediment transport rate as a function of the relative mean flow intensity. For comparison, the data generated by Inman is also plotted on this graph. A regression

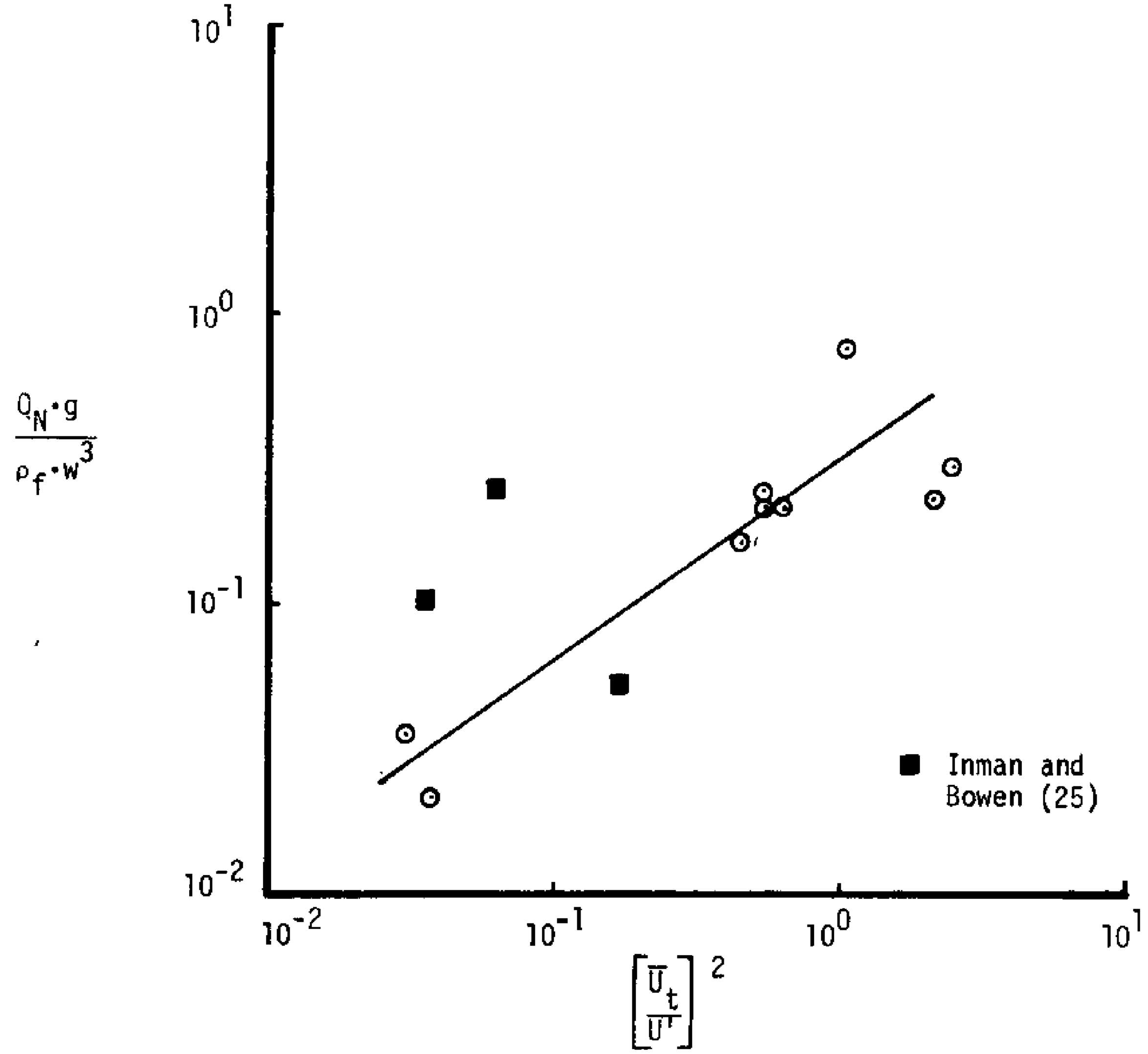

Figure 23. Net sediment transport rate for combined flows as a function of the relative flow intensity

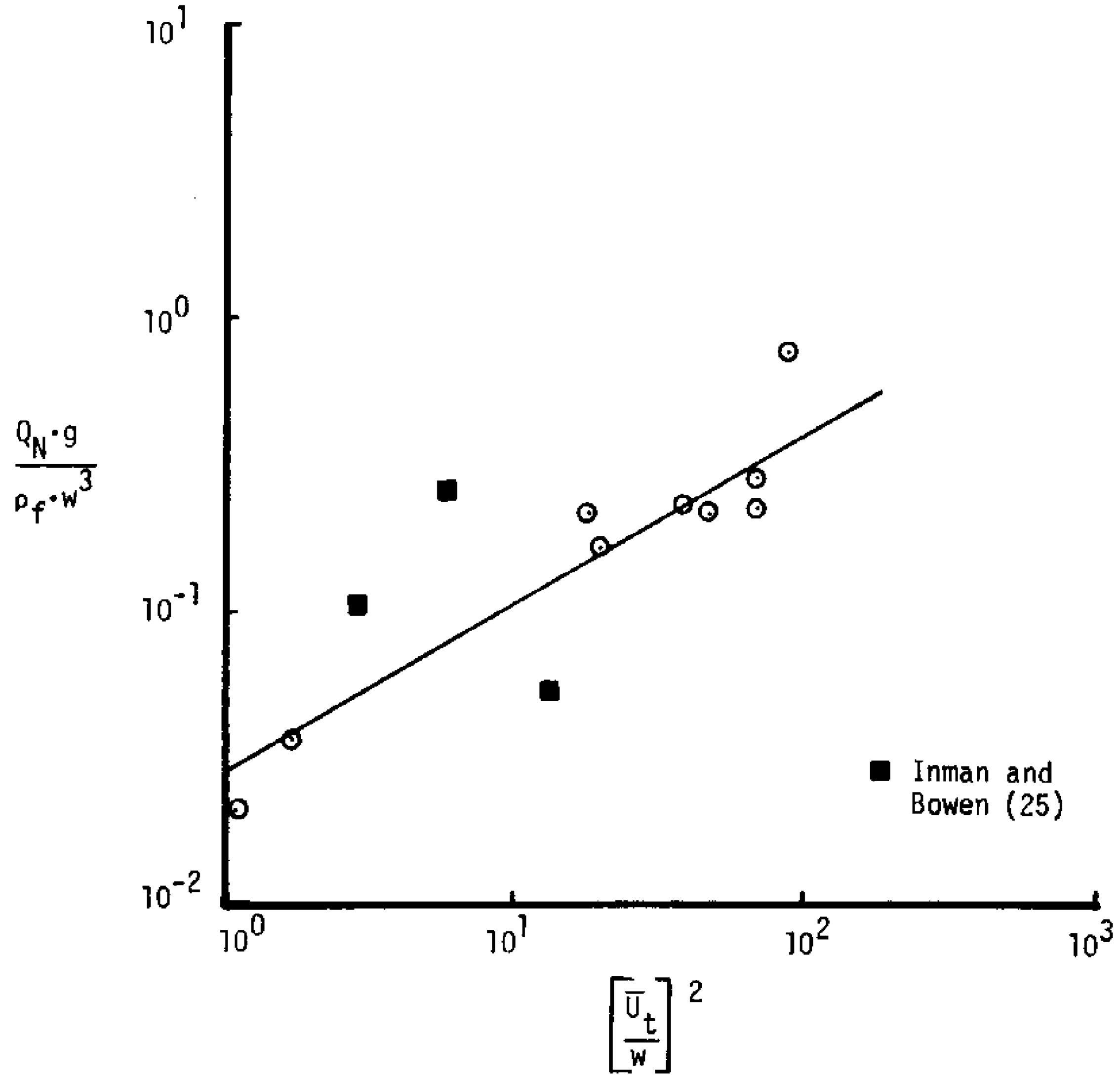

Figure 24. Net sediment transport rate for combined flows as a function of the relative mean current intensity

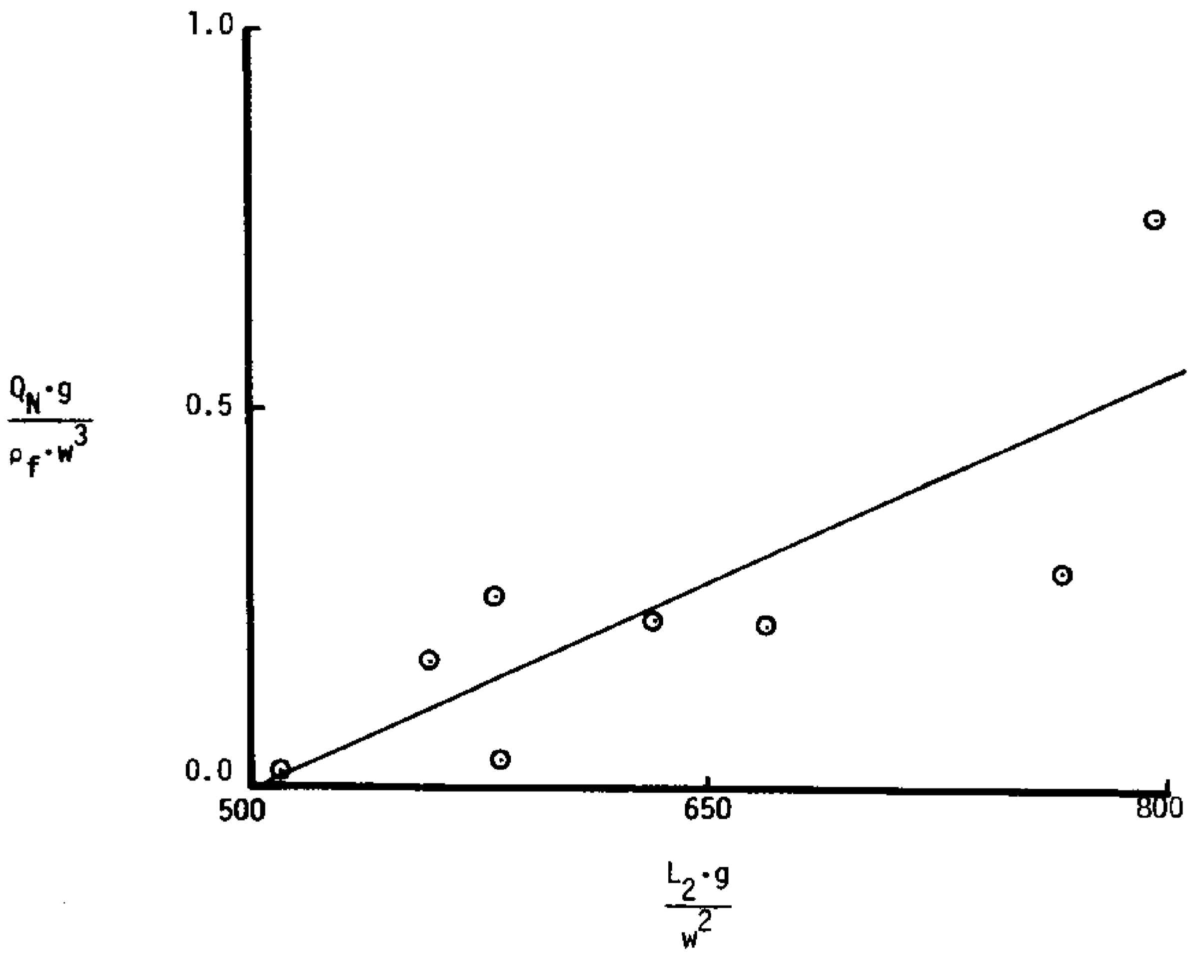

Figure 25. Net sediment transport rate for combined flows as a function of the ripple length

model shows that the nondimensional net sediment transport rate is related to the relative mean flow intensity as

$$\log \left(\frac{Q_n \cdot g}{\rho_f \cdot W^3}\right) = 1.12 \log \left(\frac{\bar{U}_t}{W}\right) - 1.49 \qquad 5.30$$

or equivalently as

$$\frac{Q_n \cdot g}{\rho_f \cdot W^3} = 0.033 \left(\frac{\bar{U}_t}{W}\right)^{1.12} \qquad 5.31$$

with a correlation coefficient of 0.70. Thus, for the range of data that is presented, the logarithm of the nondimensional net sediment transport rate correlates better with the logarithm of the relative mean flow intensity than it did with the logarithm of the relative flow intensity.

The nondimensional net sediment transport is displayed as a function of the nondimensional ripple length in Figure 25. A simple linear regression line is also shown on the graph. The correlation coefficient between the variables is 0.52. Thus, the limited data which is available shows that there is a relationship between the nondimensional ripple length and the nondimensional net sediment transport rate. However, more data is needed to further investigate the relationship so that better estimates of the transport rate can be made from ripple characteristics.

The combined flow net sediment transport rates are used to test the sediment transport model proposed by Bagnold (3). The theory indicates that the net immersed sediment transport rate is a linear function of the stream power which is defined as the rate at which the fluid does work on the sediment bed. Equation 2.20 represented a mathematical statement of this concept, i.e.

$$i = K\cdot(\bar{\tau}_0\cdot U)\ . \tag{5.32}$$

The constant K is an efficiency factor which represents the fraction of the work done by the fluid on the bed which is used to transport sediment. If all the work done by the fluid on the bed is employed to transport sediment, then K equals 1. For the process under consideration, τ was calculated using Equation 2.17 which was developed for a laminar boundary layer flow over a smooth, flat, impermeable bed. Obviously, some of the assumptions used to derive Equation 2.17 were not satisfied in the experimental system but this equation does represent a valid estimate of the wave induced shear stress. As theories for $\bar{\tau}_0$ develop which more accurately represent the physical system, they can be employed to update this analysis. The $\hat{U}_t$ values were employed as the appropriate representation of U. The agreement between the stream power sediment transport model and the experimental data is clearly shown in Figure 26. The data generated by Inman is also displayed for comparison. The correlation coefficient between the immersed weight sediment transport rate and the stream power is 0.73. The assumption that K equals one was made and used in Equation 5.32 to draw the line which is displayed in the figure. The assumption yields a good relationship between the theory and the experimental values which indicates that the work done in the bottom boundary layer by combined flows is very efficiently employed in the transport of sediment.

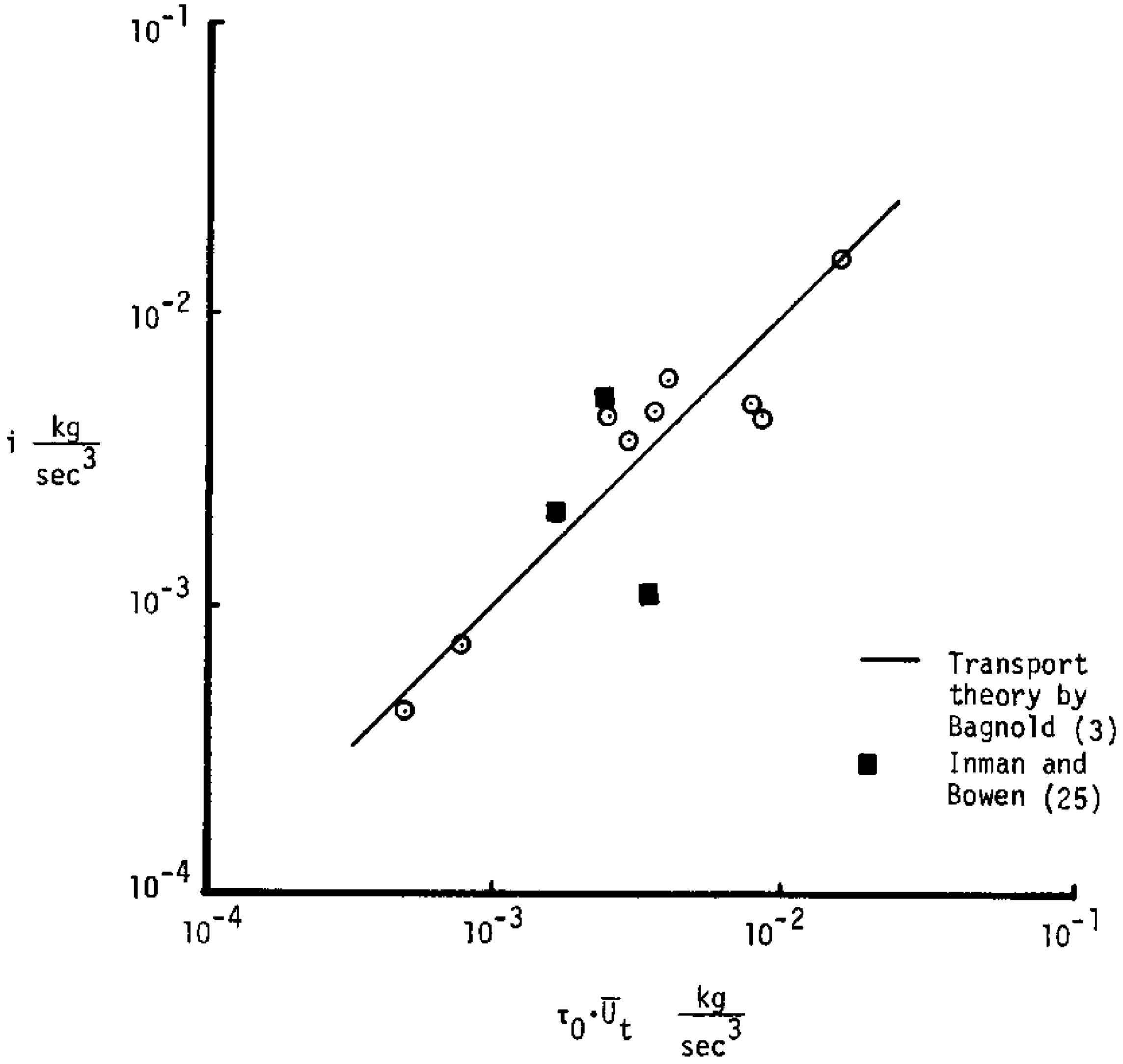

Figure 26. An experimental verification of the theory proposed by Bagnold (3) for sediment transport

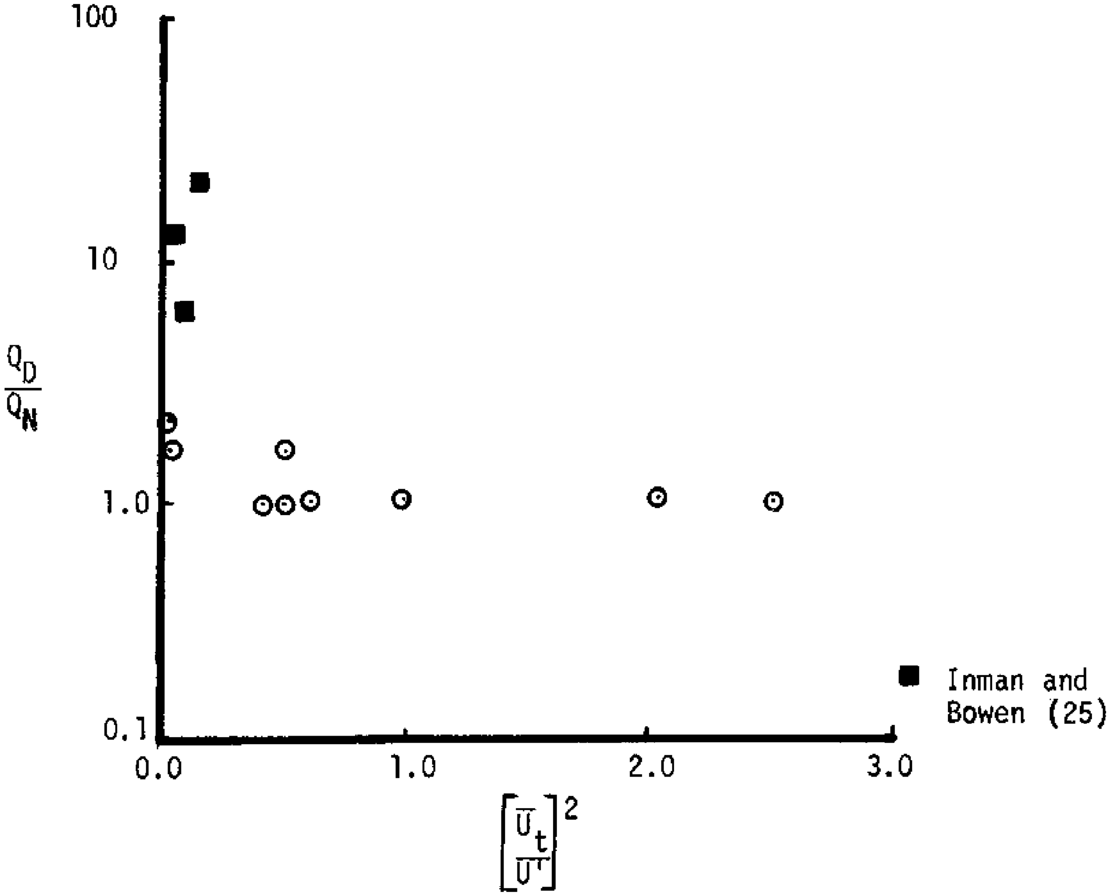

Figure 27. The relative sediment transport intensity as a function of the relative flow intensity

The ratio of the dispersive sediment transport rate to the net sediment transport rate is defined to be the relative transport intensity. The relative transport intensity is displayed as a function of the relative flow intensity in Figure 27. For small relative flow intensity values, the flow is dominated by wave motion. In this flow regime, the relative transport intensity is much greater than one which indicates that the dispersive transport rate is large compared to the net transport rate. As the relative flow intensity increases to one, the relative transport intensity decreases to one. When the total mean current velocity is greater than or equal to the maximum orbital velocity, the relative transport intensity is always one. Thus, all the sediment is transported downstream in this flow regime.

6. SUMMARY AND CONCLUSIONS

In this investigation, the sediment transport and topographic features generated by combined wave and steady current conditions which produce bedload as the dominant transport mode were investigated by laboratory experiments. The sand employed in the experiment was natural beach sand with a mean diameter of 0.22 mm. Since the mean current velocity was much less than the group velocity of the gravity waves, wave-current interactions were neglected. The topographic features generated by these flows represent a random process, so statistical methods were employed to determine meaningful characteristic measures of the topography. An earlier theoretical study by Hino (18) proposed that fully developed conditions exist when the flow field and sedimentary processes are in equilibrium and the development of the topographic features is limited by the angle of repose of the sediment. For these conditions, Hino employed a dimensional analysis to predict that the equilibrium range of the ripple number spectra obeys a minus three power law. The data collected by Jain and Kennedy (27) and other researchers support this conclusion for steady open channel flows. However, the bedform spectra for combined wave and steady current conditions produced by this investigation demonstrate that the equilibrium range does not always obey a minus three power law. Therefore, a local equilibrium condition is defined to exist when the flow field and the sedimentary processes are in equilibrium but the development of the topographic features is not limited by the angle of repose. The main results concerning the topography generated by combined wave and steady current conditions which generate bedload as the dominant transport mode are as follows:

1. The equilibrium range of the ripple number spectra for local equilibrium conditions decays more rapidly than the minus three power law.
2. For the equilibrium range of the spectra of fully developed bed forms, Hino (18) proposed that the constant of proportionality relating the power spectral density to the ripple number is a function of only the angle of repose. However, for local equilibrium conditions, the data demonstrates that the constant of proportionality is also a function of the flow field.
3. The variance of the ripple length for local equilibrium conditions generated by combined flows is less than the variance of the ripple length for fully developed conditions generated by steady open channel flows.
4. For local equilibrium conditions, the elevation of the bed topography is usually skewed toward the free surface of the water and the kurtosis of the bedform probability density distribution is approximately equal to the Gaussian value of 3.0.
5. The characteristic ripple length is approximately linearly related to the relative mean current intensity at the top of the bottom boundary layer.

During this investigation, the sediment transport rate was calculated by measuring the rate of movement of dyed sediment particles which were initially located in a core in a sediment trough. When the flow conditions were similar, this method produced net sediment transport rates which were on the same order of magnitude as the sediment transport rates measured in laboratory experiments by Inman and Bowen (25). They calculated the sediment transport rate by measuring the quantity of sand captured in traps at the ends of the test section. The main results concerning the sediment transport generated by combined wave and steady current conditions which produce bedload as the dominant transport mode are as follows:

6. The net immersed weight sediment transport rate is linearly related to the stream power available at the top of the bottom boundary layer. Furthermore, the proportionality constant is approximately 1.0 indicating that the work done by the fluid in the boundary layer is efficiently employed to transport sediment. This result confirms the sediment transport theory proposed by Bagnold (3).
7. The net sediment transport rate is approximately linearly related to the relative mean flow intensity at the top of the boundary layer.
8. The net sediment transport rate can be estimated by a measurement of the characteristic ripple length. Therefore, a method has been demonstrated which if extended by additional experimental investigation may allow the sediment transport rate for a broad range of combined flow conditions to be estimated from photographs of the bottom topography.
9. The dispersive sediment transport intensity decreases as the relative flow intensity increases.

No single theory has demonstrated the ability to predict the sediment transport rate for the entire range of sedimentary and flow field conditions. Therefore, advances in the knowledge of the sediment transport phenomena must rely on the results of well formulated experiments. The judicious use of dimensional analysis and reliable experimental data will allow the specification of differing transport regimes. In each flow regime the fundamental relationship between the flow field and the transport phenomena must be thoroughly investigated. A dimensional analysis was developed for combined flow fields which indicates the basic parameters which must be varied in order to broaden the knowledge of the transport phenomena generated by these flows. The analysis shows that the sediment characteristics, the relative flow intensity, the relative mean flow velocity, the relative depth, and the relative wave frequency are the important parameters controlling the dynamic sedimentary processes generated by combined flows.

Finally, a better understanding of the basic physical processes generating sediment transport must rely on theoretical developments which include real fluid and sediment effects.

7. LIST OF REFERENCES

1. Anderson, A. G., "The Characteristics of Sediment Waves Formed by Flow in Open Channels," Proceedings of the Third Conference in Fluid Mechanics, Minneapolis, Minnesota, 1953, pp. 379-395.

2. Ashida, K., and Tanaka, Y., "A Statistical Study of Sand Waves," International Association for Hydraulic Research, Part 2, 1957, pp. 103-110.

3. Bagnold, R. A., "Mechanics of Marine Sedimentation," in The Sea, ed. M. N. Hill, Interscience Publishers, Inc., New York, New York, Vol. 3, 1963, pp. 507-528.

4. Bendat, J. S., and Piersol, A. G., Random Data: Analysis and Measurement Proceedures, Wiley-Interscience, Inc., New York, New York, 1971.

5. Blassius, H., "The Boundary Layers in Fluids with Little Friction," Technical Memorandum No. 1256, National Advisory Committee for Aeronautics, 1908.

6. Carsten, M. R., Neilson, F. M., and Altinbilek, H. D., "Bedforms Generated in the Laboratory Under an Oscillating Flow: Analytical and Experimental Study," Technical Memorandum No. 28, U.S. Army Corps of Engineers, Coastal Engineering Research Center, 1969.

7. Carter, T. G., Liu, P., and Mei, C. C., "Mass Transport by Waves and Offshore Sand Bedforms," Journal of the Waterways, Harbors, and Coastal Engineering Division, ASCE, Vol. 99, No. WW2, Proc. Paper 9699, May, 1973, pp. 165-184.

8. Cartwright, D. E. and Longuet-Higgins, M.S., "The Statistical Distribution of the Maxima of a Random Function," Proceedings of the Royal Society, A237, 1956, pp. 212-232.

9. Colby, B. R. and Hembree, C. H., "Computations of the Total Sediment Discharge, Niobrara River near Cody, Nebraska," Water Supply Paper No. 1357, U.S. Geological Survey, 1965.

10. Davies, O. L. and Goldsmith, P. L., Statistical Methods in Research and Production, 4th ed., Oliver and Boyd Ltd., Edinburg, Great Britain, 1947.

11. Duane, D. B., "Tracing Sand Movement in the Littoral Zone: Progress in the Radioisotropic Sand Study," Miscellaneous Paper No. 4-70, U.S. Army Corps of Engineers, Coastal Engineering Research Center, 1970.

12. DuBoys, P., "Etudes du Regimes du Rhone et L'action Exercee par les Eaux un Lit a Fond de Graviers Indefiniment Affouillable, "

LIST OF REFERENCES (Continued)

Annales des Ponts et Chaussees, Series 5, Vol. 18, 1879, pp. 141-195.

13. Einstein, H. A., "The Bedload Function for Sediment Transport in Open Channel Flows," Technical Bulletin No. 1026, U.S. Department of Agriculture, Soil Conservation Service, 1950.

14. Folk, R. L., Petrology of Sedimentary Rocks, The University of Texas, Austin, Texas, 1968.

15. Hansen, M., "Velocity Distribution in the Boundary Layer of a Submerged Plate," Technical Memorandum No. 585, National Advisory Committee for Aeronautics, 1928.

16. Harms, J. C., "Hydraulic Significance of Some Sand Ripples", Bulletin, Geological Society of America, Vol. 80, No. 3, 1969, pp. 363-396.

17. Hegge-Zijner, B. G., "Measurements of the Velocity Distribution in the Boundary Layer Along a Plane Surface," Thesis Presented to the Delft Institute of Hydrology, at Delft, Holland, in 1924, in Partial Fulfillment of the Requirements for the Degree of Doctor of Philosophy.

18. Hino, M., "Equilibrium Range Spectra of Sand Waves Formed by Flowing Water," Journal of Fluid Mechanics, Vol. 34, Part 3, 1968, pp. 565-574.

19. Ho, R. T., and Gelhar, L. W., "Interaction Between Turbulent Flows and Undular Permeable Boundaries," Report No. 180, Ralph M. Parsons Laboratory, Massachusetts Institute of Technology, Cambridge, Massachusetts 1974.

20. Hooker, E., "The Suspension of Solids in Flowing Water," Transactions, Society of Civil Engineers, Vol. 36, 1896, pp. 239-324.

21. Horikawa, K., and Wantanabe, A., "A Study of Sand Movement Due to Wave Action," Coastal Engineering in Japan, Vol. 10, 1967, pp. 39-57.

22. Huang, N. E., "Mass Transport Induced by Wave Motion," Journal of Marine Research," Vol. 28, No. 1, 1970, pp. 35-50.

23. Inman, D. L., "Wave-Generated Ripples in Nearshore Sands," Technical Memorandum No. 100, U.S. Army Corps of Engineers, Beach Erosion Board, 1957.

LIST OF REFERENCES (Continued)

24. Inman, D. L., and Bagnold, R. A., "Littoral Processes," in The Sea, ed. M. N. Hill, Interscience Publishers, Inc., New York, New York, Vol. 3, 1963, pp. 529-553.

25. Inman, D. L., and Bowen, A. J., "Flume Experiments on Sand Transport by Waves and Currents," Proceedings, 8th Conference on Coastal Engineering, 1963, pp. 137-150.

26. Jain, S. C., "Evolution of Sand Wave Spectra," Thesis Presented to the University of Iowa, at Iowa City, Iowa, in 1971, in Partial Fulfillment of the Requirements for the Degree of Doctor of Philosophy.

27. Jain, S. C., and Kennedy, J. F., "The Spectral Evolution of Sedimentary Bedforms," Journal of Fluid Mechanics, Vol. 63, Part 2, 1974, pp. 301-314.

28. Kennedy, J. F., "The Mechanics of Dunes and Antidunes in Erodible-bed Mechanics," Journal of Fluid Mechanics, Vol. 16, Part 4, 1963, pp. 521-544.

29. Komar, P. D., Beach Processes and Sedimentation, Prentice-Hall, Inc., Englewood Cliffs, New Jersey, 1976.

30. Komar, P. D., and Inman, D. L., "Longshore Sand Transport on Beaches," Journal of Geophysical Research, Vol. 75, No. 30, 1970, pp. 5914-5927.

31. Komar, P., Neudeck, R. H., and Kulm, L. D., "Observations and Significance of Deep-Water Oscillatory Ripple Marks on the Oregon Continental Shelf," in Shelf Sediment Transport, ed. D. Swift, D. Duane, and O. Pilkey, Dowden, Hutchinson and Ross, Stroudsburg, Pa., 1972, pp. 601-619.

32. Lamb, H., Hydrodynamics, 6th ed., Dover Publications, Inc., New York, New York, 1945.

33. Longuet-Higgins, M. S., "Mass Transport in Water Waves," Proceedings of the Royal Society, A245, 1953, pp. 535-581.

34. Longuet-Higgins, M.S., "On the Intervals Between Zeros of a Random Function," Proceedings of the Royal Society, A246, 1958, pp. 99-118.

35. Masterson, R. P., Machemehl, J. L., and Cavaroc, V. V., "Sediment Movement in Tubbs Inlet, North Carolina," Report No. 73-2, The Center for Marine and Coastal Studies, N. C. State University, Raleigh, North Carolina, 1974.

LIST OF REFERENCES (Continued)

36. McArthur, D.S., and Rector, N. H., "A Method for the Rapid Production of Fluorescent Tracer," Report No. 4, Coastal Studies, Institute, Louisiana State University, Baton Rouge, Louisiana, 1970, pp. 77-81.

37. McClennen, C. E., "New Jersey Continental Shelf Near Bottom Current Meter Records and Recent Sediment Activity," Journal of Sedimentary Petrology, Vol. 43, No. 2, 1973, pp. 371-380.

38. McGoldrick, L. F. "A Sensitive Capacitance to Voltage Converter, With Applications to Surface Wave Measurements," A Review of Scientific Instruments, Vol. A2, No. 3, 1971, pp. 359-361.

39. McQuivey, R. S., "Principles and Measuring Techniques of Turbulence Characteristics in Open-Channel Flows," Professional Paper No. 802-A, U.S. Geological Survey, 1973.

40. Mitchel, S. J., Fluid and Particle Mechanics, Maxwell House, Inc., Elmsford, New York, 1970.

41. Mogridge, G. R., and Kamphuis, J. W., "Experiments on Bedform Generation by Wave Action," Proceedings, 13th Conference on Coastal Engineering, 1973, pp. 1123-1142.

42. Newton, J. G., Pilkey, O. H., and Blanton, J. O., An Oceanographic Atlas of the North Carolina Coastal Margin, Division of Mineral Resources, North Carolina Department of Conservation and Development, Raleigh, North Carolina, 1971.

43. Nordin, C. F., "Statistical Properties of Dune Profiles," Thesis Presented to Colorado State University, at Fort Collins, Colorado, in 1968, in Partial Fulfillment of the Requirements for the Degree of Doctor of Philosophy.

44. Phillips, O. M., "The Equilibrium Range of the Spectrum of Wind-Generated Waves," Journal of Fluid Mechanics, Vol. 4, 1958, pp. 426-434.

45. Phillips, O. M., The Dynamics of the Upper Ocean, Cambridge University, Press, London, Great Britain, 1969.

46. Rice, S. O., "Mathematical Analysis of Random Moise," in Selected Papers on Noise and Stocastic Processes, ed. N. Wax, Dover Publications, Inc., New York, New York, 1954.

47. Schlichting, H., Boundary Layer Theory, 6th ed., McGraw-Hill Book Co., Inc., New York, New York, 1968.

48. Simons, D. B., Richardson, E. V., and Nordin, C. F., "Sedimentary

LIST OF REFERENCES (Continued)

Structures Generated by Flow in Alluvial Channels," in Primary Structures and their Hydro-Dynamic Interpretation, by Society of Economic Paleontologists and Mineralogists, No. 12, 1965, pp. 34-52.

49. Straub, L. G., Discussion of "Sand Mixtures and Sand Movements in Fluvial Models," Transactions of the American Society of Civil Engineers, Vol. 100, 1935, pp. 789-873.

50. Sturm, G. V., and Sorrell, F. Y., "Optical Wave Measurement Technique and Experimental Comparison with Conventional Wave Height Probes," Applied Optics, Vol. 12, No. 8, 1973, pp. 1928-1931.

51. Tison, L. J., "Origine des Ondes de Sable et des Bancs de Sable sans L'action des Courants," 3rd Meeting of the International Association for Hydraulic Structure Research, Grenoble, France, 1949.

52. U.S. Army Corps of Engineers, Shore Protection Manual, Coastal Engineering Research Center, Washington, D.C., 1973.

53. Vanoni, V. A., "Sediment Transport Mechanics: Sediment Discharge Formulas," Journal of the Hydraulics Division, ASCE, Vol. 97 No. HY4, 1971, pp. 523-567.

54. Vanoni, V. A., Brooks, N. H., and Kennedy, J. F., "Lecture Notes on Sediment Transport and Channel Stability," Report KH - RI, W. H. Keck Laboratory, California Institute of Technology, Pasadena, California, 1960.

55. Vincent, G. E., "Contributions to the Study of Sediment Transport on a Horizontal Bed Due to Wave Action," Proceedings of the 6th Conference on Coastal Engineering, 1957, pp. 326-355.

56. Yang, C. T., "Incipient Motion and Sediment Transport," Journal of the Hydraulics Division, ASCE, Vol. No. HY10, 1973, pp. 1679-1704.

8. LIST OF SYMBOLS AND NOTATIONS

SYMBOL	QUANTITY
a	maximum gravity wave amplitude
a'	constant related to sediment pore space
A_c	total cross sectional area of transported dyed sediment
A_i	fractional cross sectional area of transported dyed sediment
C^*	generalized coefficient relating the power spectral density to the ripple number
$C(\Theta)$	coefficient relating the power spectral density to the ripple number.
d	mean grain diameter
D	drag coefficient
D_s	Stokes drag coefficient for a sphere
f	gravity wave frequency
g	acceleration due to gravity
G	power spectral density function
h	mean depth of fluid
i	immersed weight net sediment transport rate per unit channel width
k	ripple number
k_w	angular gravity wavenumber
K	constant in the sediment transport theory by Bagnold (1963)

LIST OF SYMBOLS AND NOTATIONS (Continued)

SYMBOL	QUANTITY
K_t	bedform kurtosis
L	gravity wave wavelength
L_c	width of dyed sediment core
L_{ex}	orbital excursion length of a water particle at the top of the bottom boundary layer
L_1	a characteristic ripple length
L_2	a characteristic ripple length
M	relative slope of the equilibrium range of a spectrum
M_e	immersed weight
M_i	ith moment of a power spectral density distribution
p	a nondimensional number
pd	probability density distribution
q_i	a fractional sediment transport per unit channel width per unit time
Q	sediment discharge
Q_D	total sediment discharge per unit channel width per unit time
Q_N	net sediment transport per unit channel width per unit time
Q^+	upstream sediment transport per unit channel width per unit time
Q^-	downstream sediment transport per unit channel width per unit time
R	a Reynolds number

LIST OF SYMBOLS AND NOTATIONS (Continued)

SYMBOL	QUANTITY
SK_t	bedform skewness
$STDV_r$	standard deviation of ripples
$STDV_t$	total standard deviation of bed
t	time
t_o	time constant for particle response to velocity variations
T	gravity wave period
T_e	duration of an experiment
u	x component of velocity
$\bar{U}$	mean fluid velocity
$\bar{U}_o$	gravity wave orbital velocity at the top of the bottom boundary layer
$\bar{U}_t$	total mean fluid velocity
U'	Maximum gravity wave orbital velocity at the top of the bottom boundary layer
v_i	fractional volume of the total displayed dyed sediment volume
V_c	total displaced dyed sediment volume
w	fall velocity of a sediment particle
$\bar{w}$	decrement of wave power
x,y,z	Cartesian coordinates
x_i	distance V_i is transported

LIST OF SYMBOLS AND NOTATIONS (Continued)

SYMBOL	QUANTITY
Z	change in elevation of dyed sediment core
α	bottom boundary layer thickness
α_i	nondimensional number
δ	boundary layer thickness
Δ	spectral width
ζ	fluid free surface elevation
η	bed elevation relative to mean bed elevation
η_m	a local maximum value of η
η_o	normalized local maximum value of η
Θ	angle of repose of sediment
λ	ripple length
η	dynamic viscosity
ν	kinematic viscosity
π	3.14
Π_i	i^{th} Buckingham Pi quantity
ρ_f	density of a fluid
ρ_s	density of sediment
$\bar{\tau}$	mean current bottom shear stress

LIST OF SYMBOLS AND NOTATIONS (Continued)

SYMBOL	QUANTITY
$\bar{\tau}_o$	wave induced mean shear stress at the top of the bottom boundary layer
ψ	a sedimentary characteristic

9. APPENDICES

9.1 Bed Profile Probability Density Distributions and Cumulative Probability Distributions

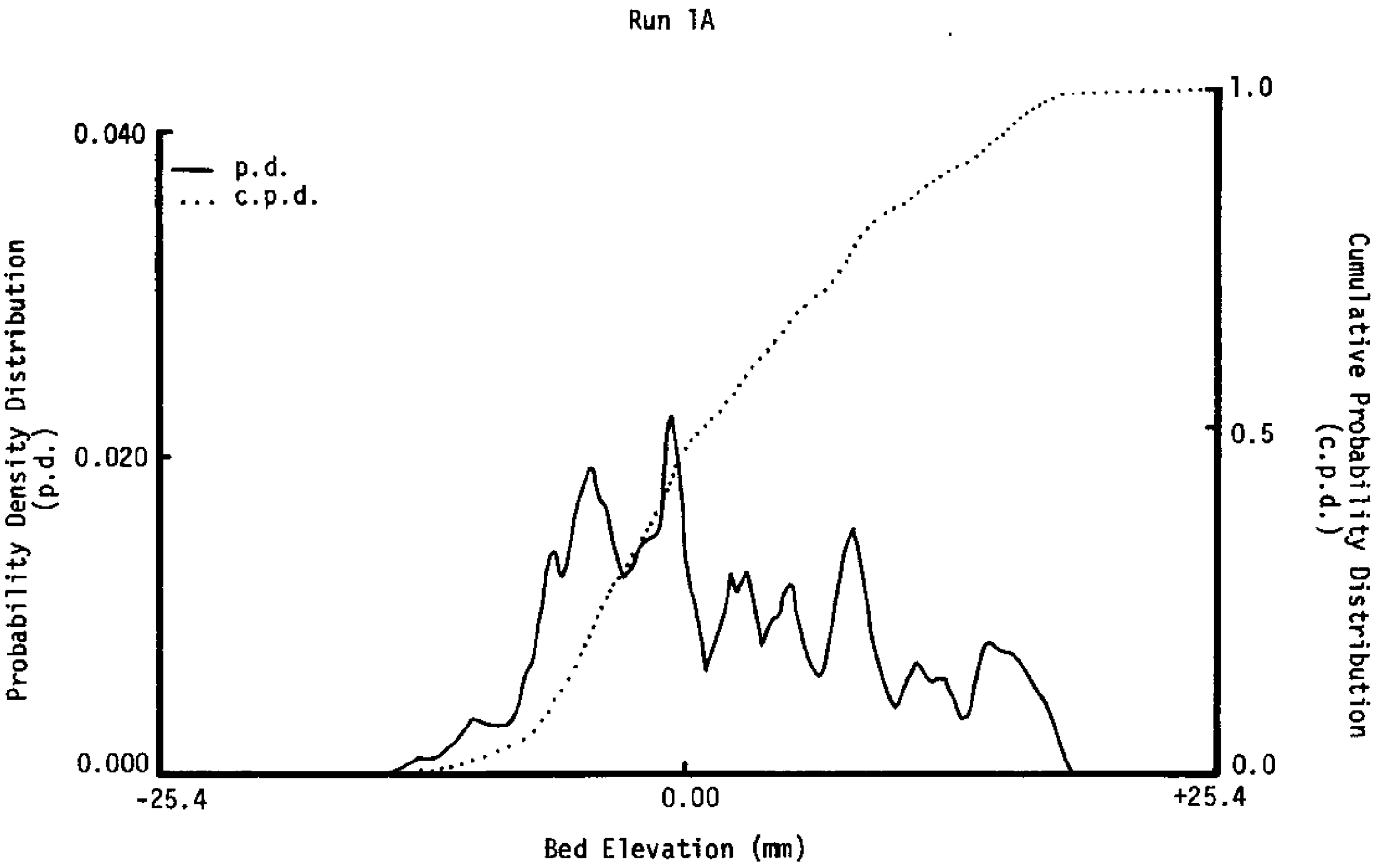

Figure 28. Bed profile probability density distribution and cumulative probability distribution

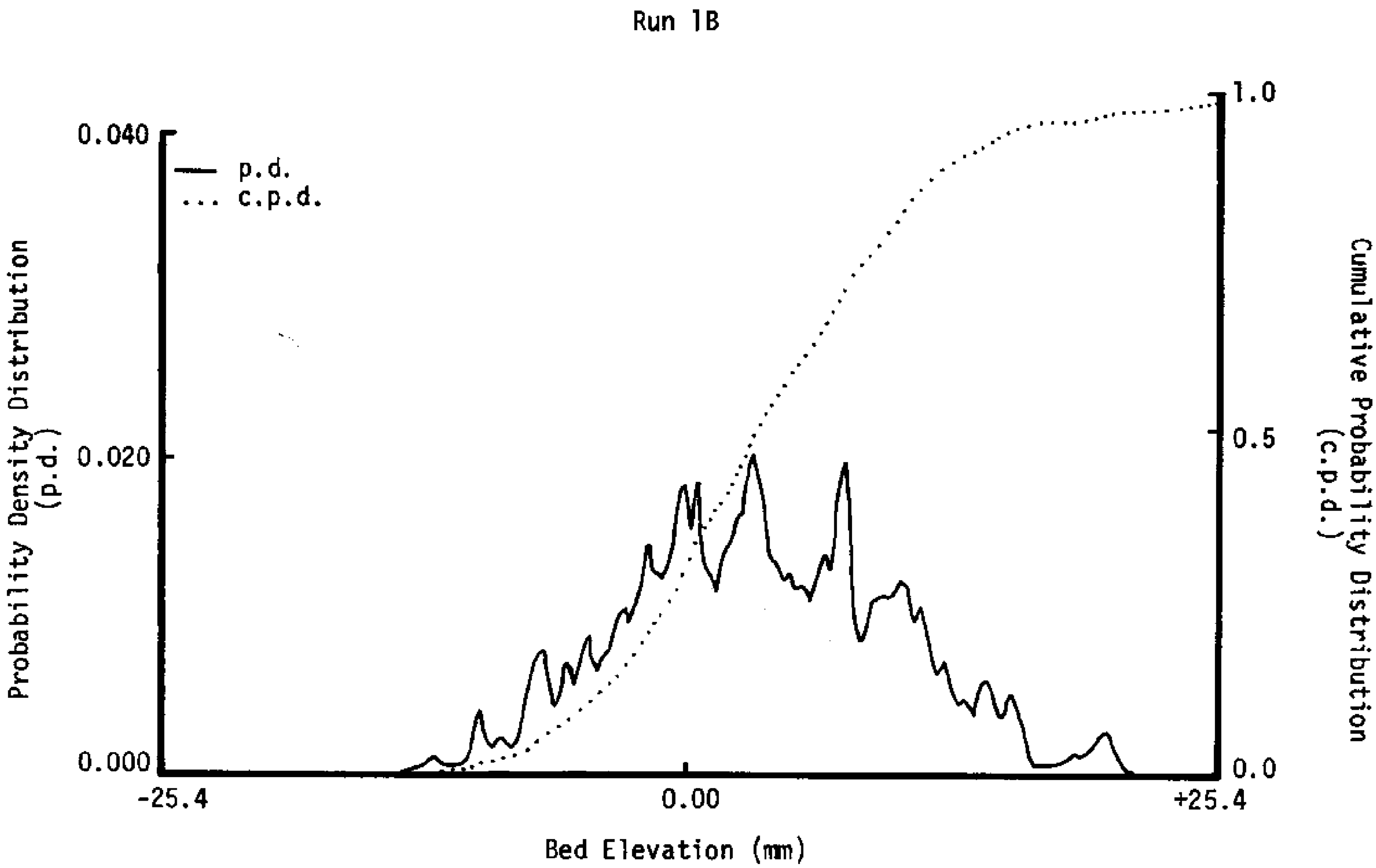

Figure 29. Bed profile probability density distribution and cumulative probability distribution

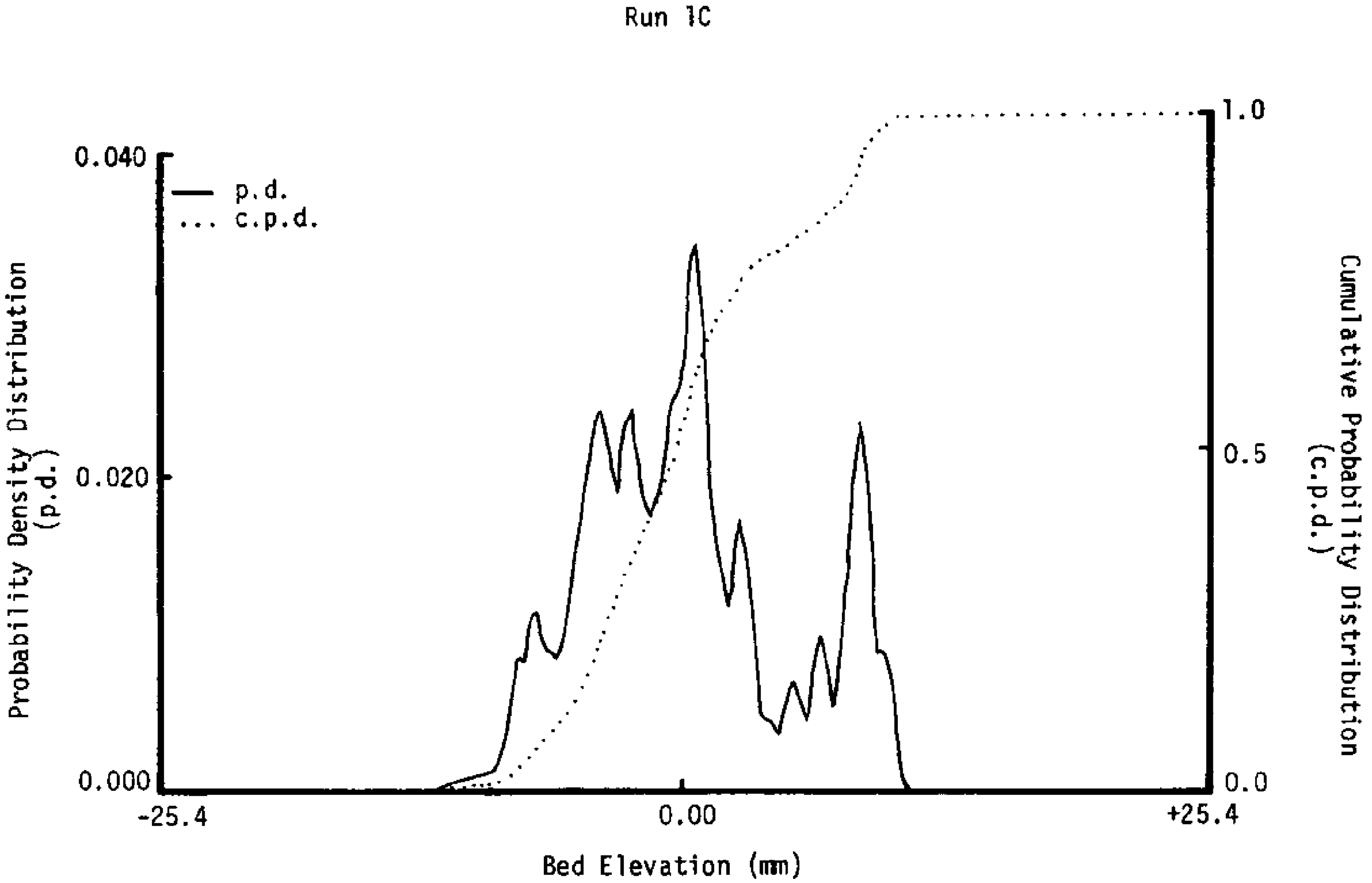

Figure 30. Bed profile probability density distribution and cumulative probability distribution

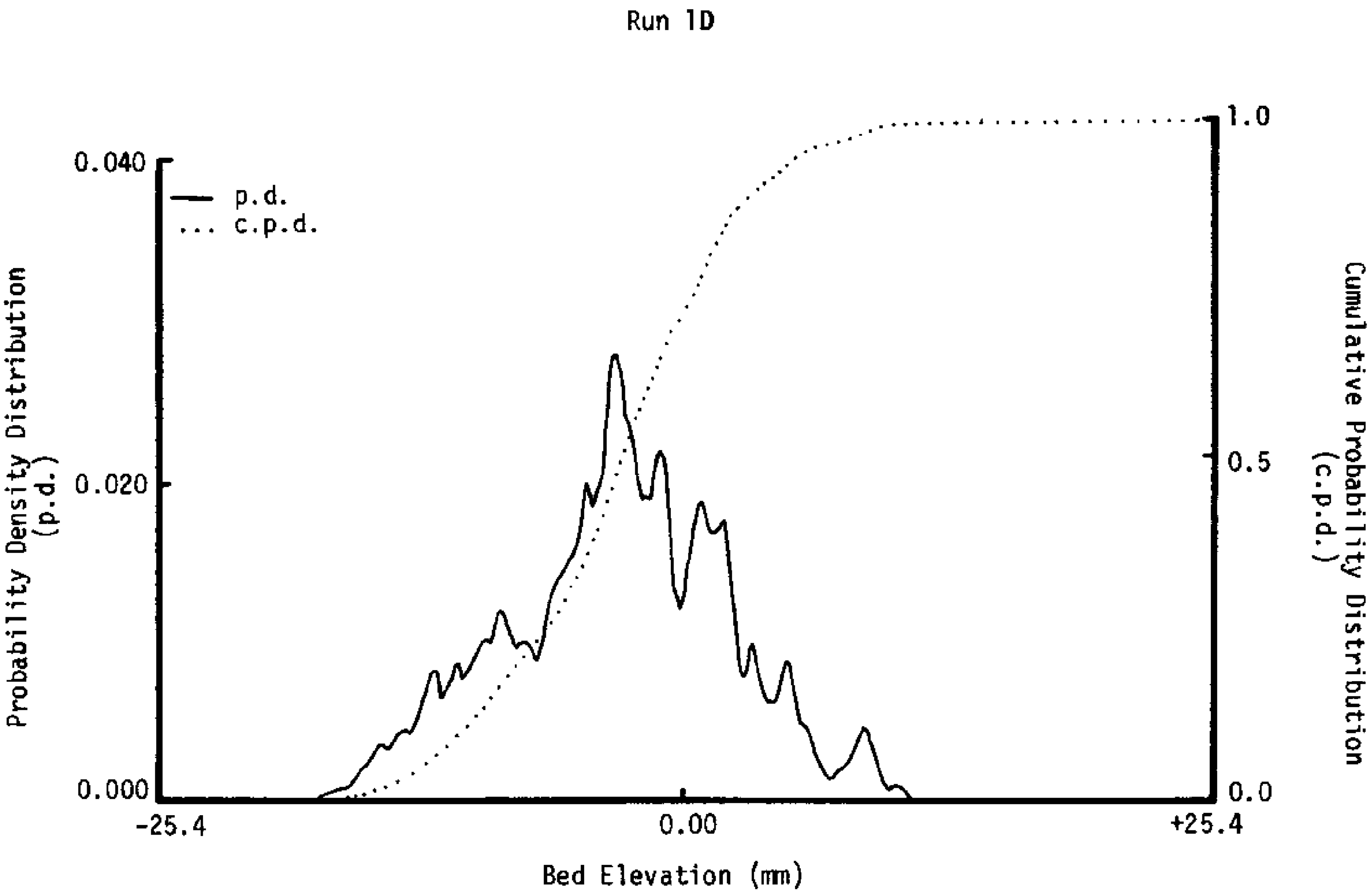

Figure 31. Bed profile probability density distribution and cumulative probability distribution

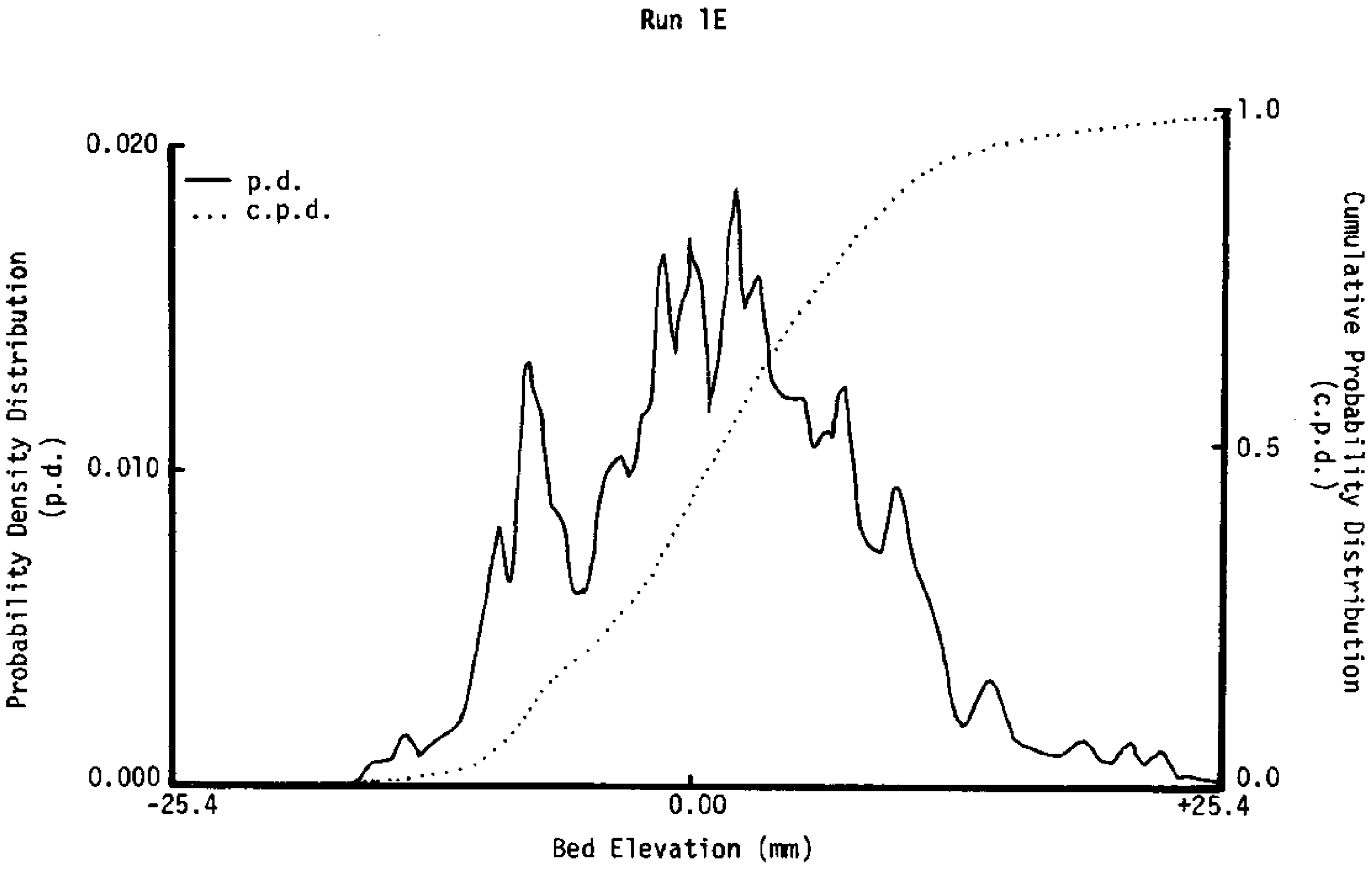
Run 1E

Figure 32. Bed profile probability density distribution and cumulative probability distribution

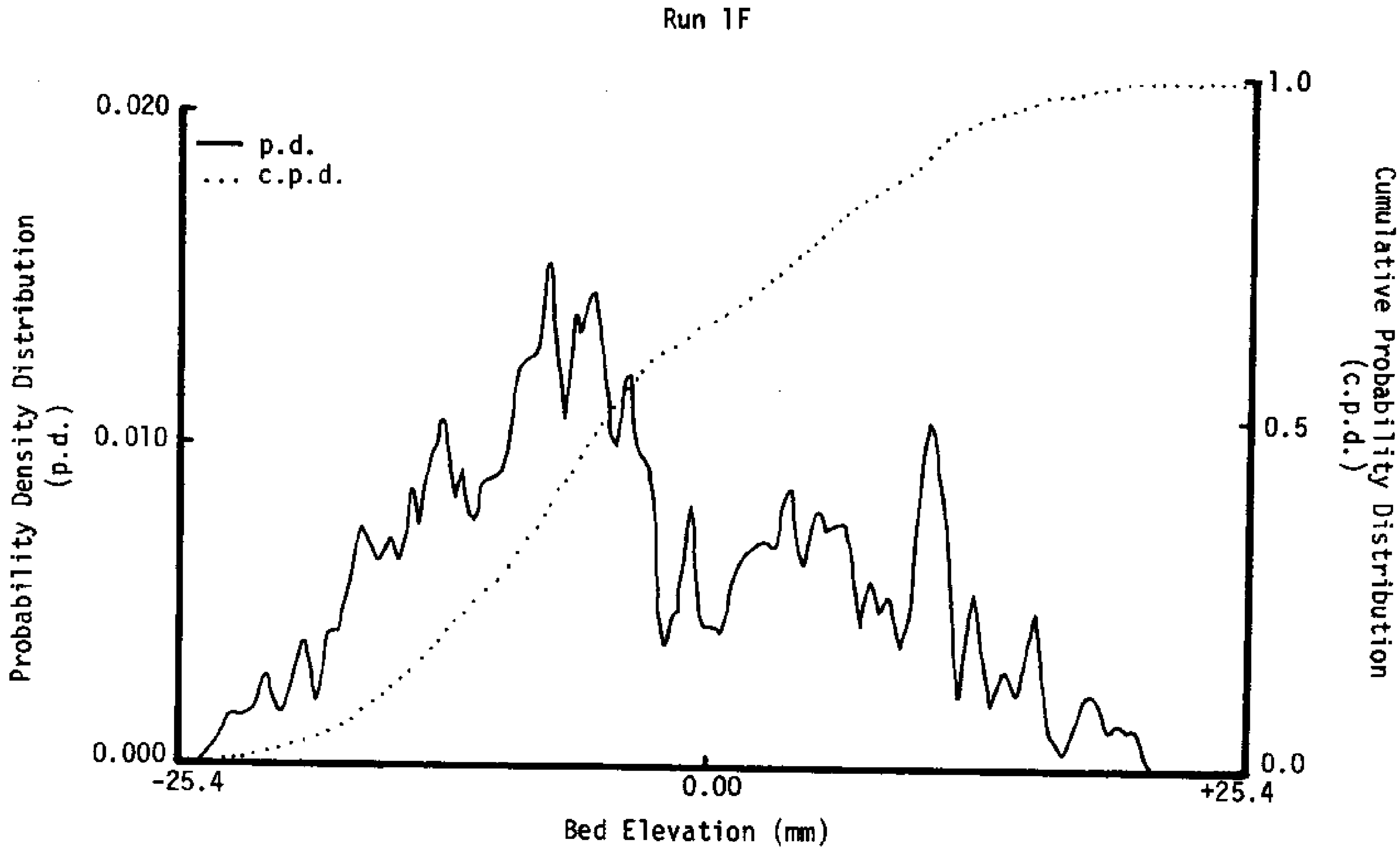
Run 1F

Figure 33. Bed profile probability density distribution and cumulative probability distribution

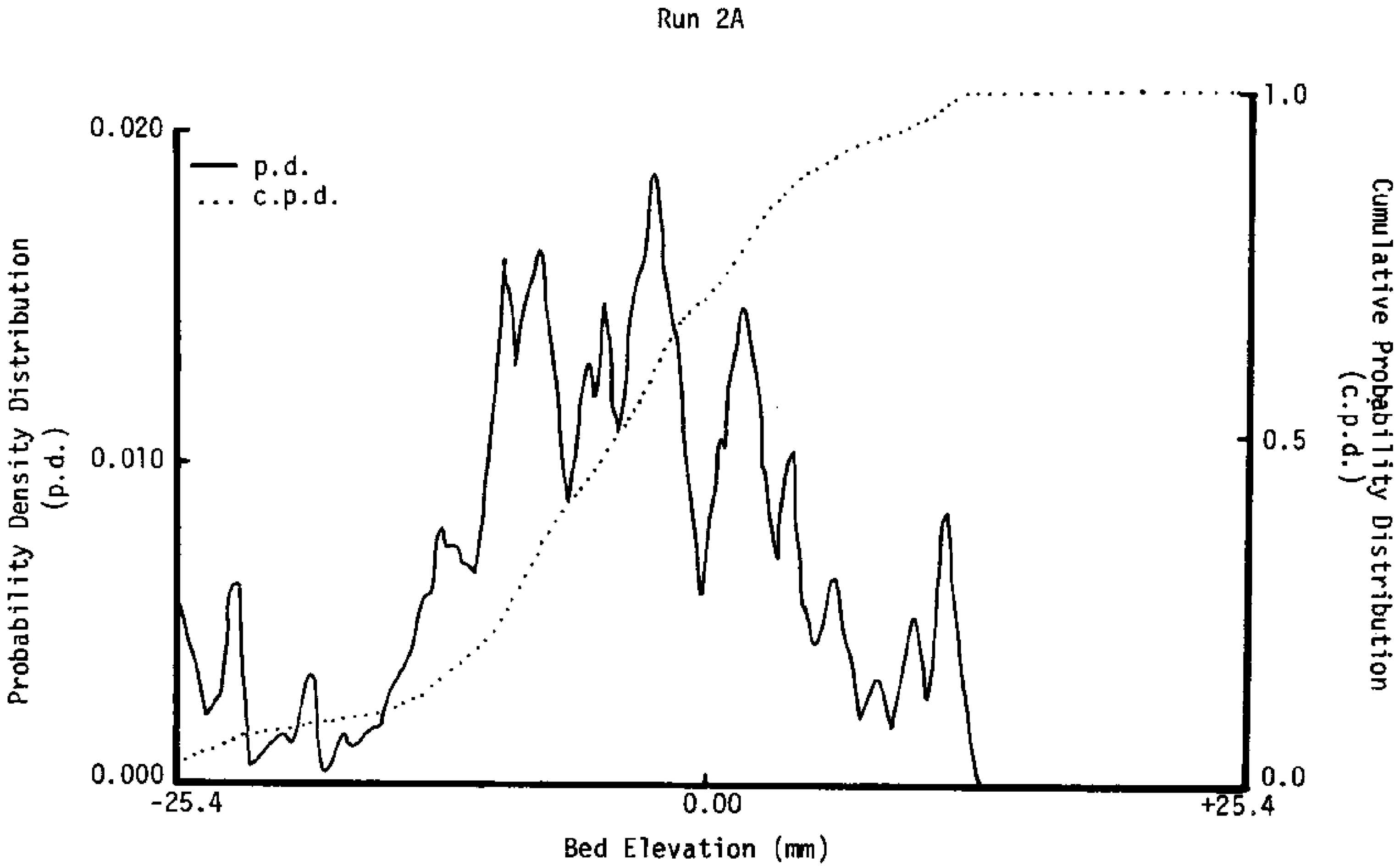

Figure 34. Bed profile probability density distribution and cumulative probability distribution

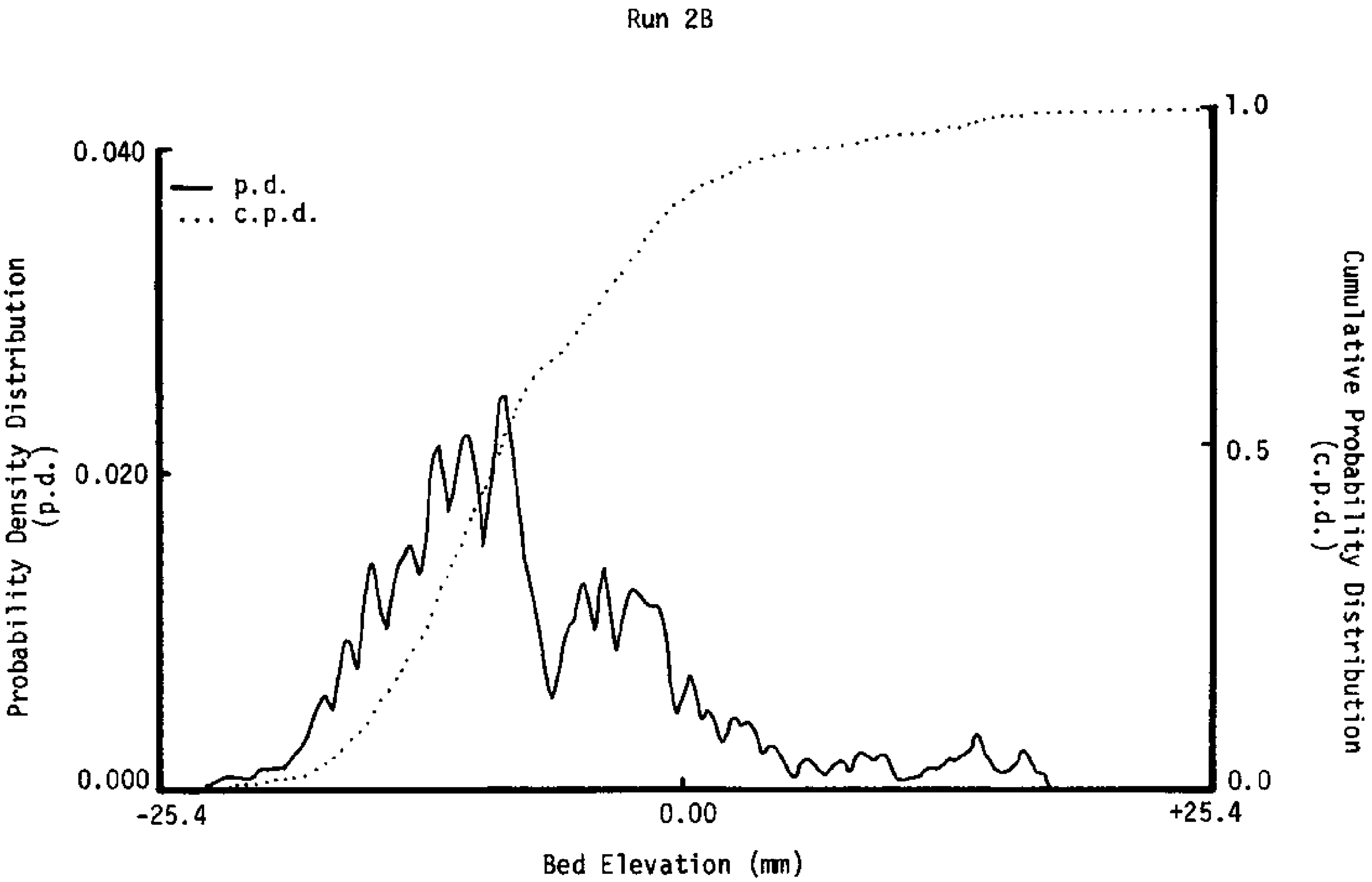

Figure 35. Bed profile probability density distribution and cumulative probability distribution

Run 2C

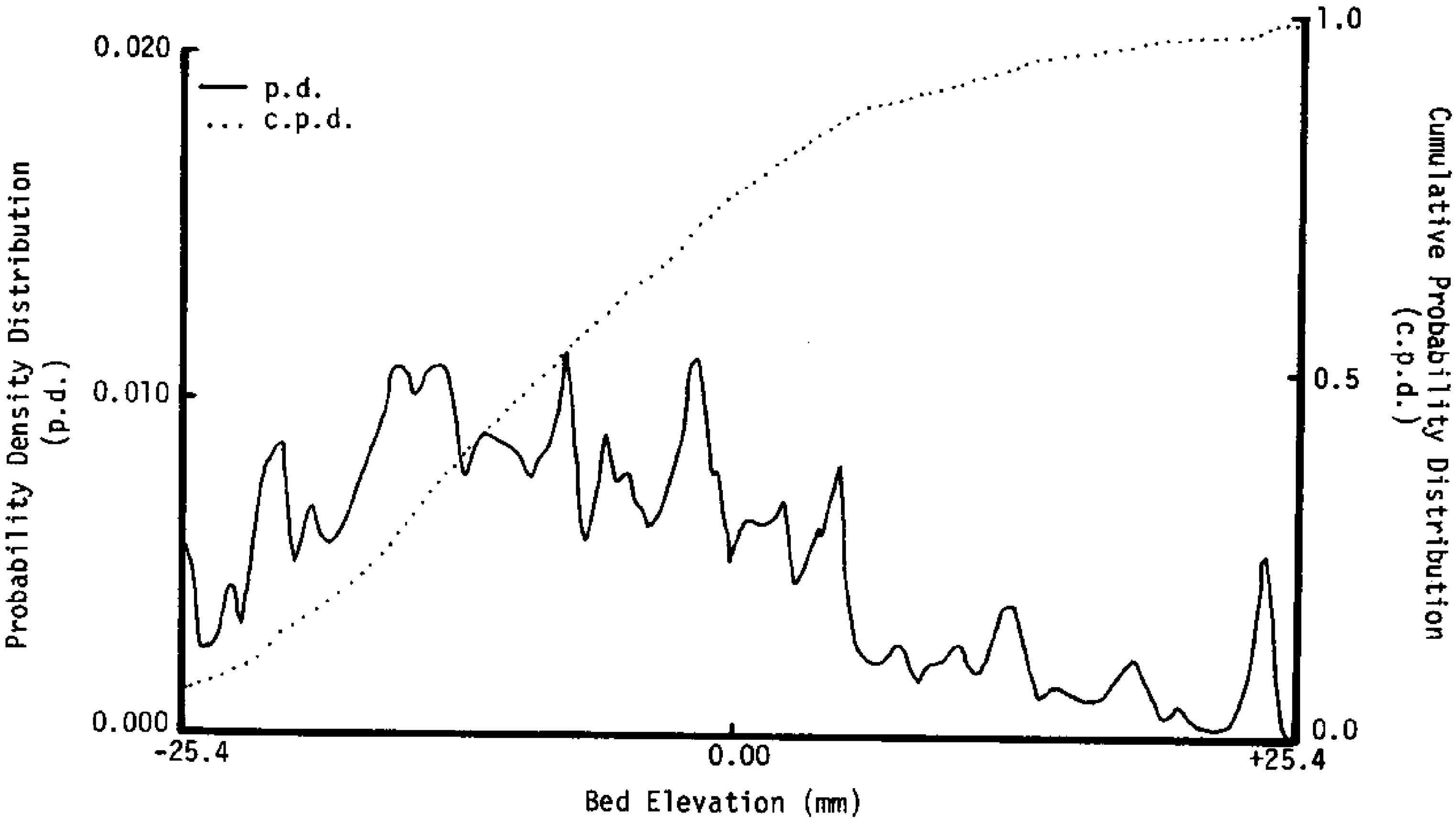

Figure 36. Bed profile probability density distribution and cumulative probability distribution

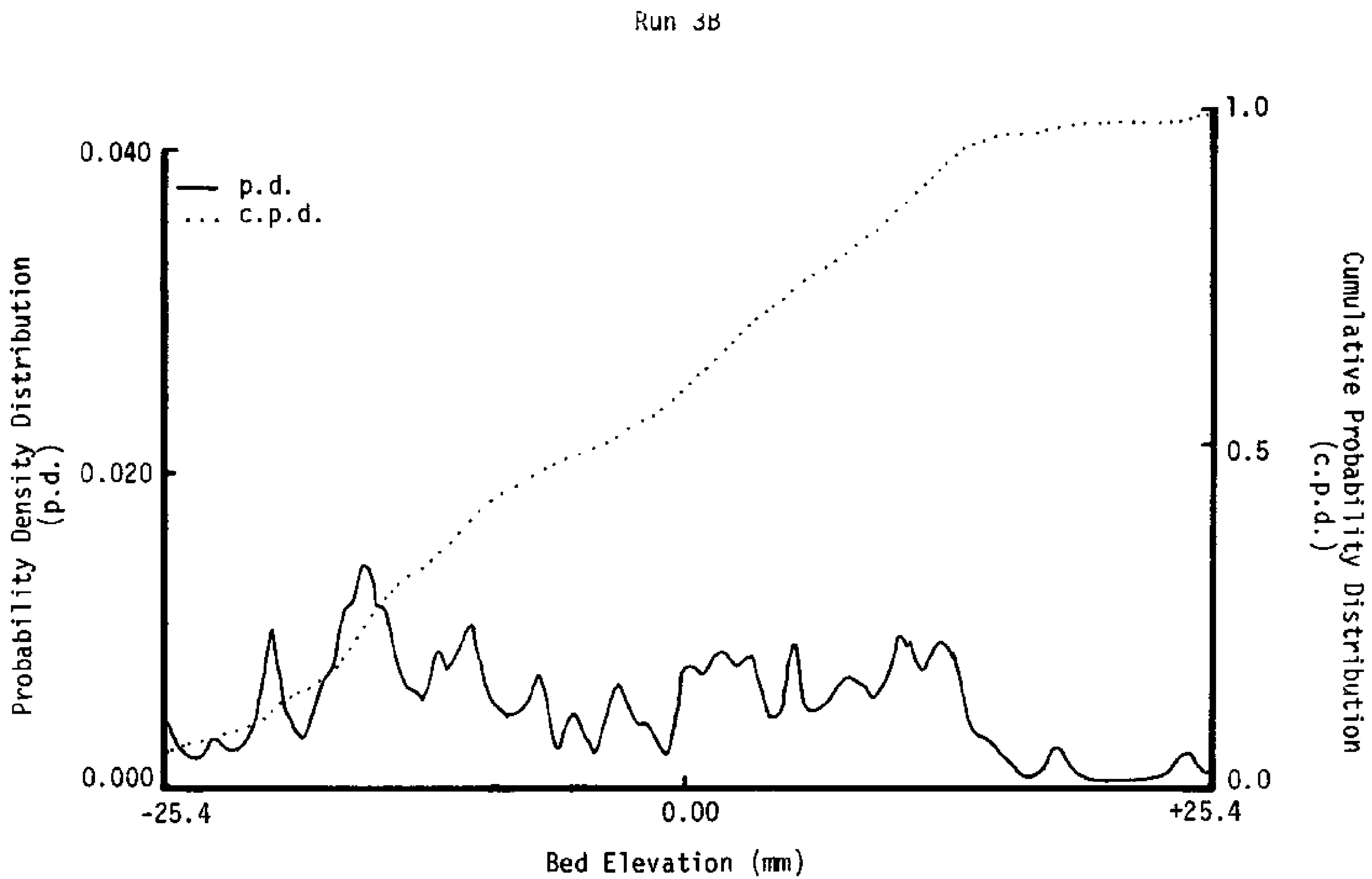

Figure 37. Bed profile probability density distribution and cumulative probability distribution

Run 5A

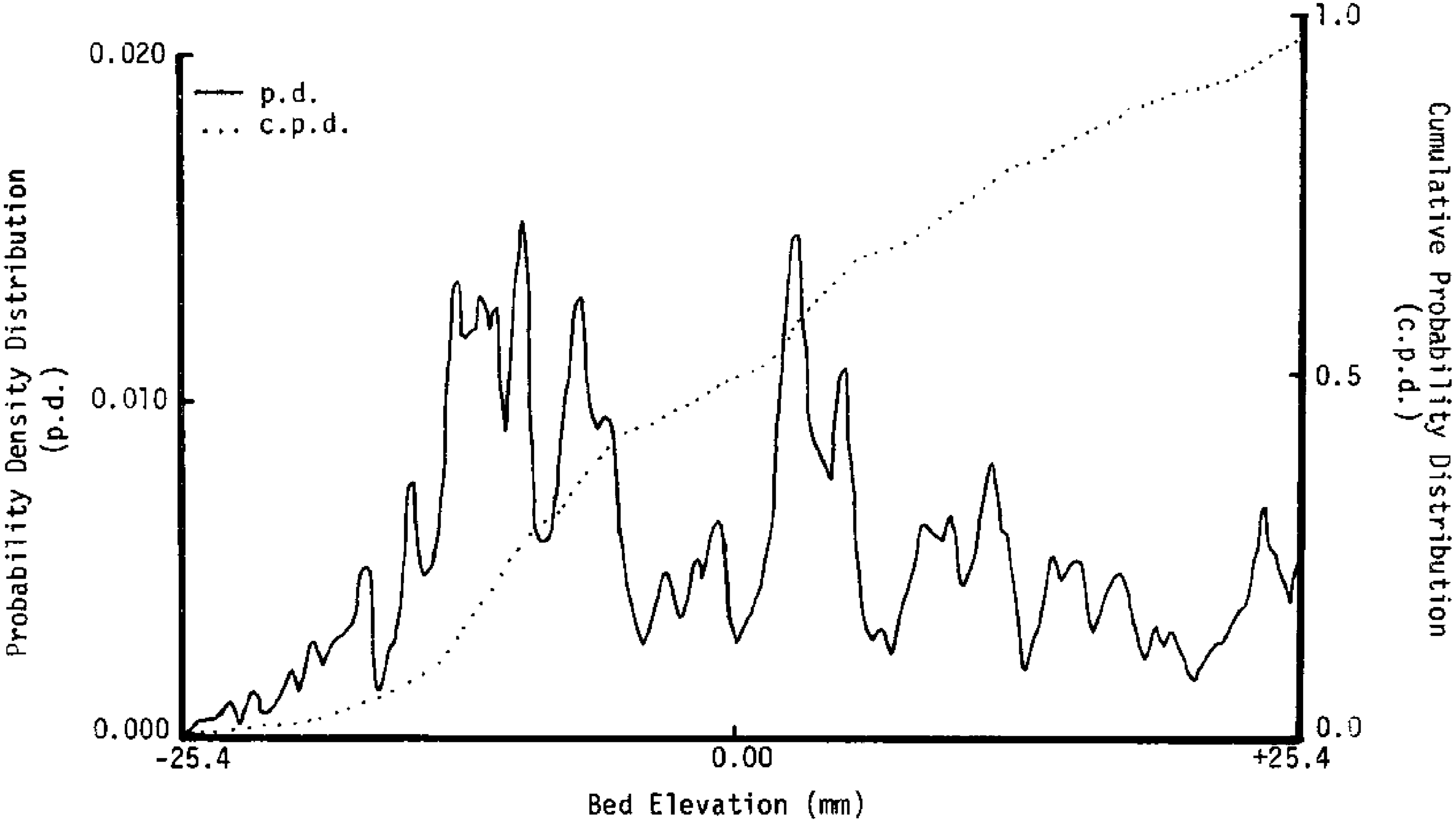

Figure 38. Bed profile probability density distribution and cumulative probability distribution

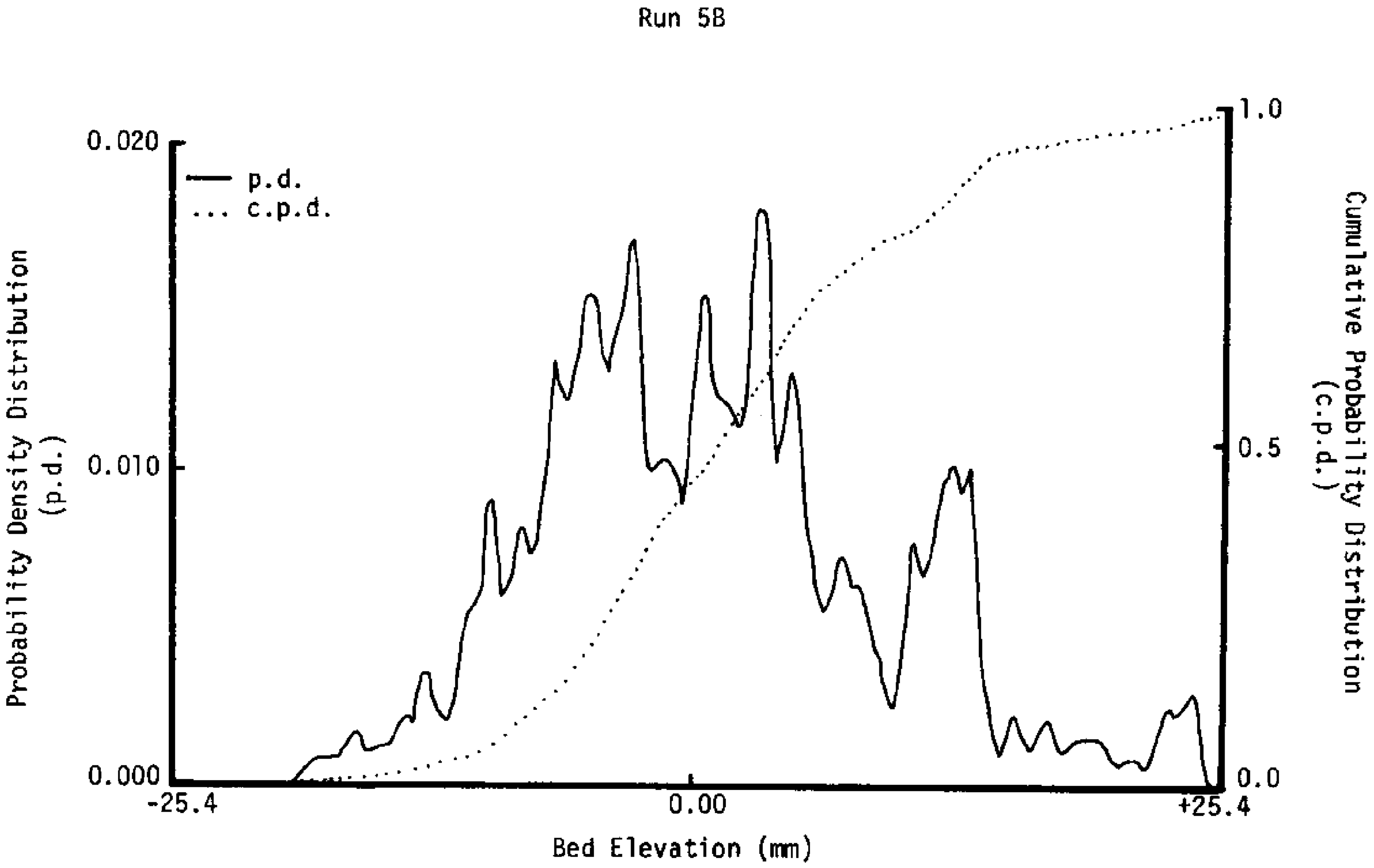

Figure 39. Bed profile probability density distribution and cumulative probability distribution

Run 5C

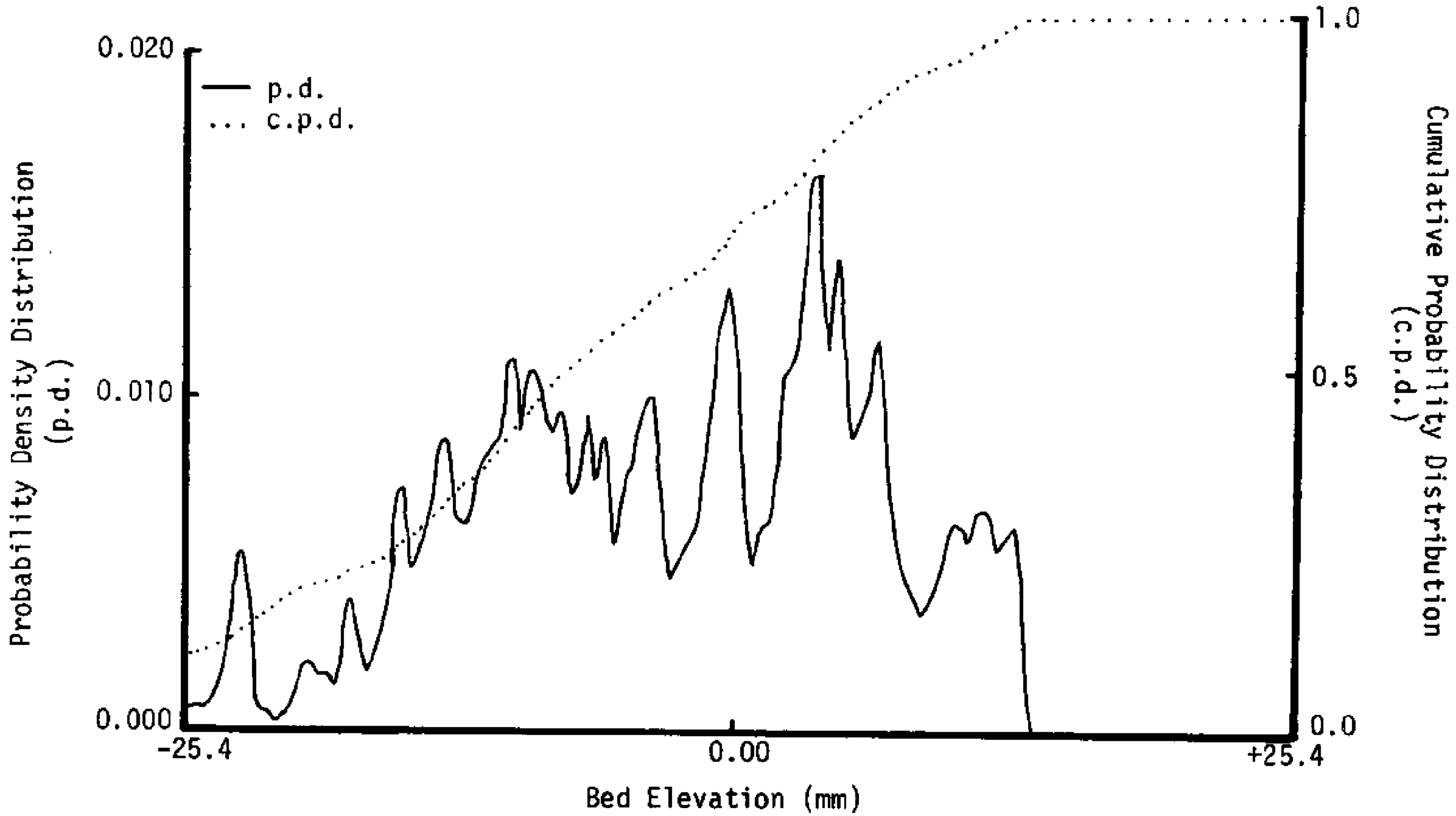

Figure 40. Bed profile probability density distribution and cumulative probability distribution

9.2 Ripple Number Spectra of Bed Profiles

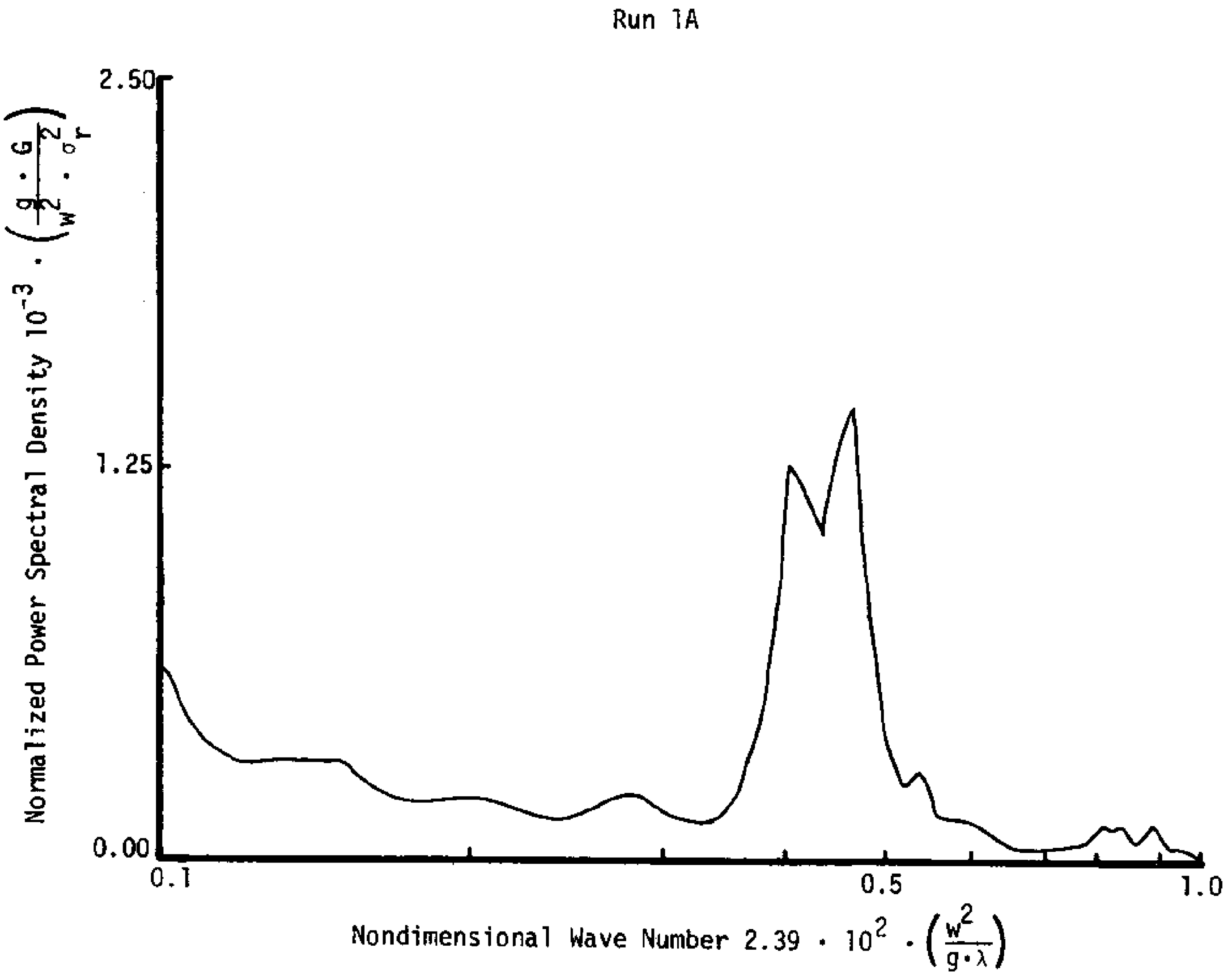

Figure 41. Spectrum of bed profile

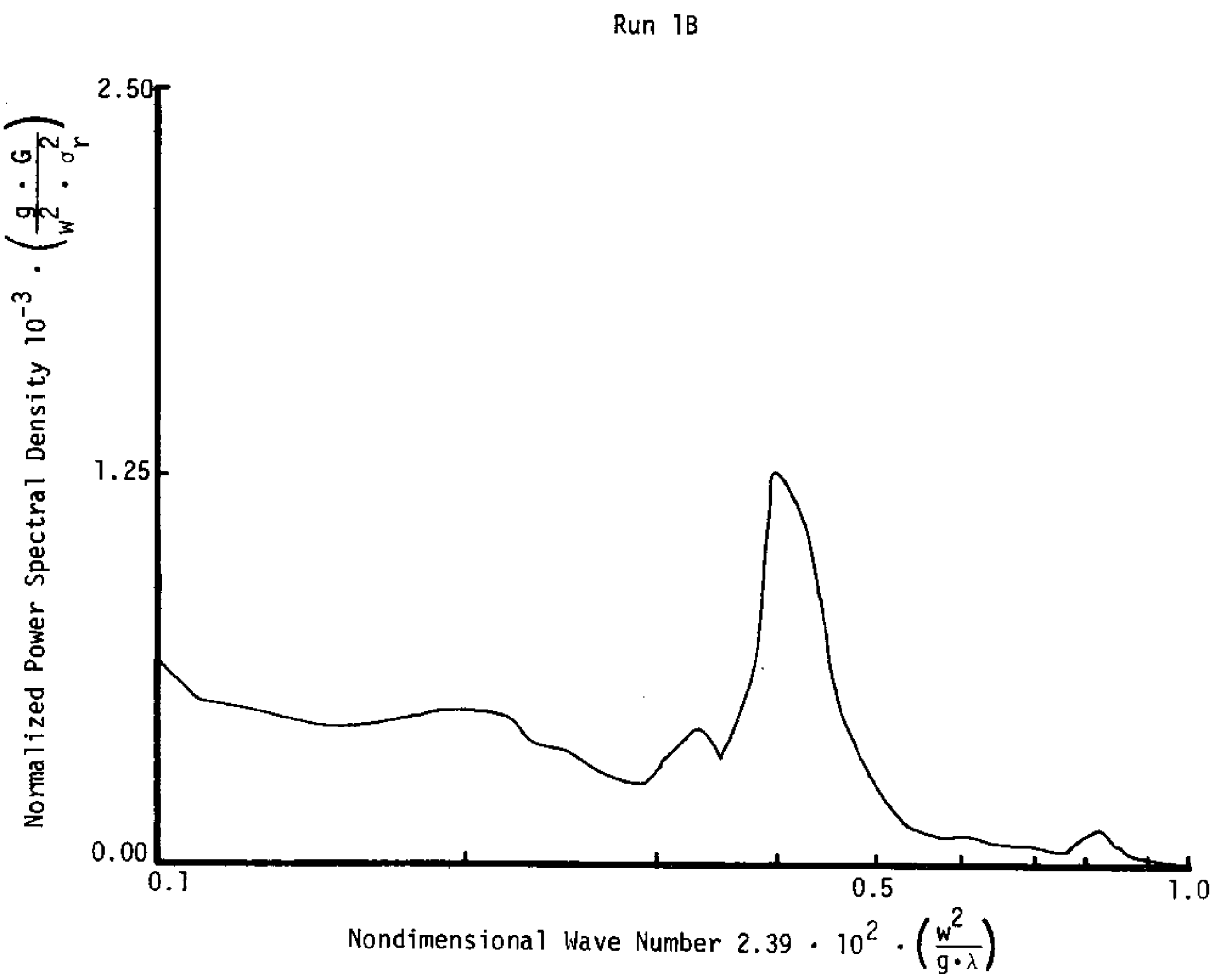

Figure 42. Spectrum of bed profile

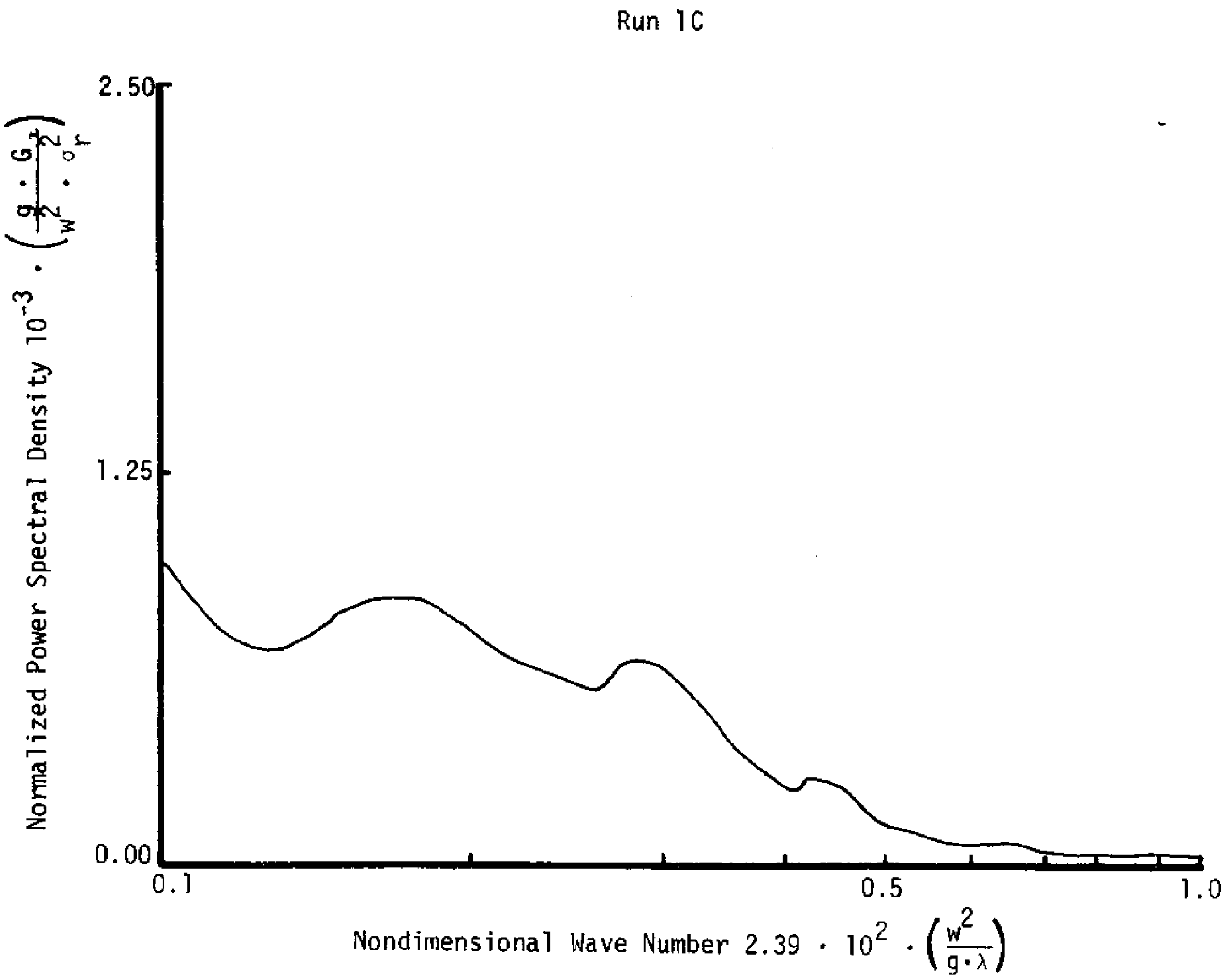

Figure 43. Spectrum of bed profile

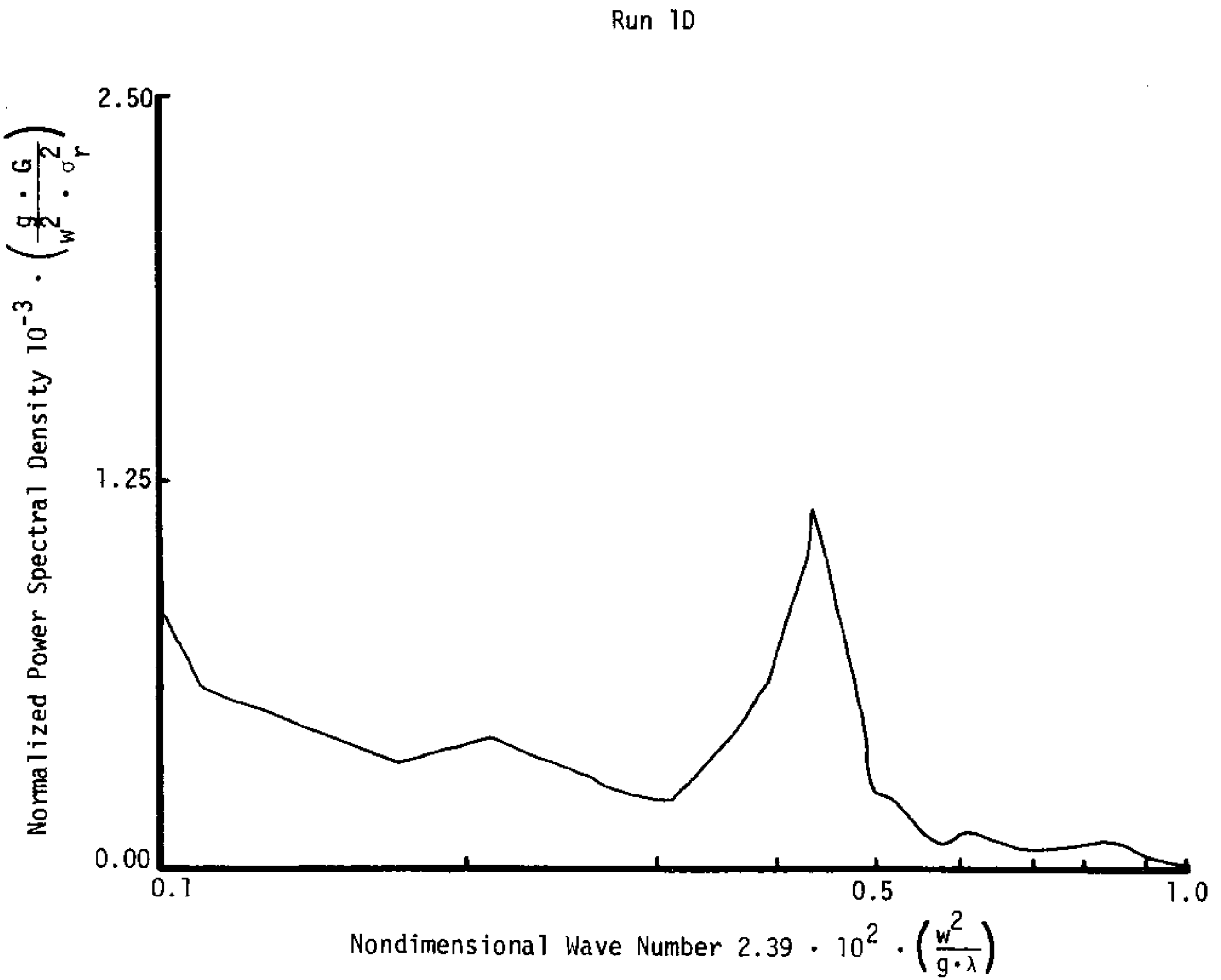

Figure **44.** Spectrum of bed profile

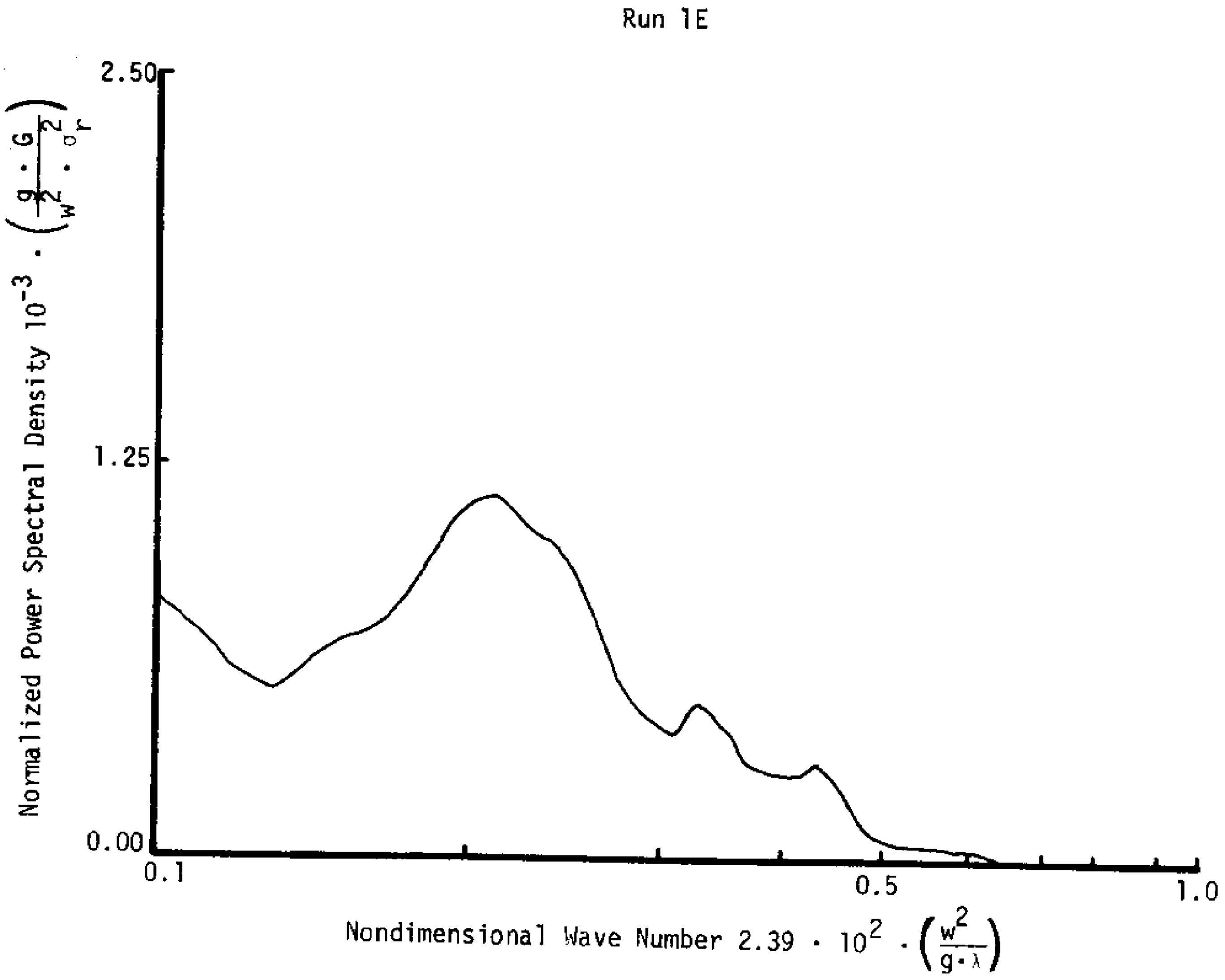

Figure 45. Spectrum of bed profile

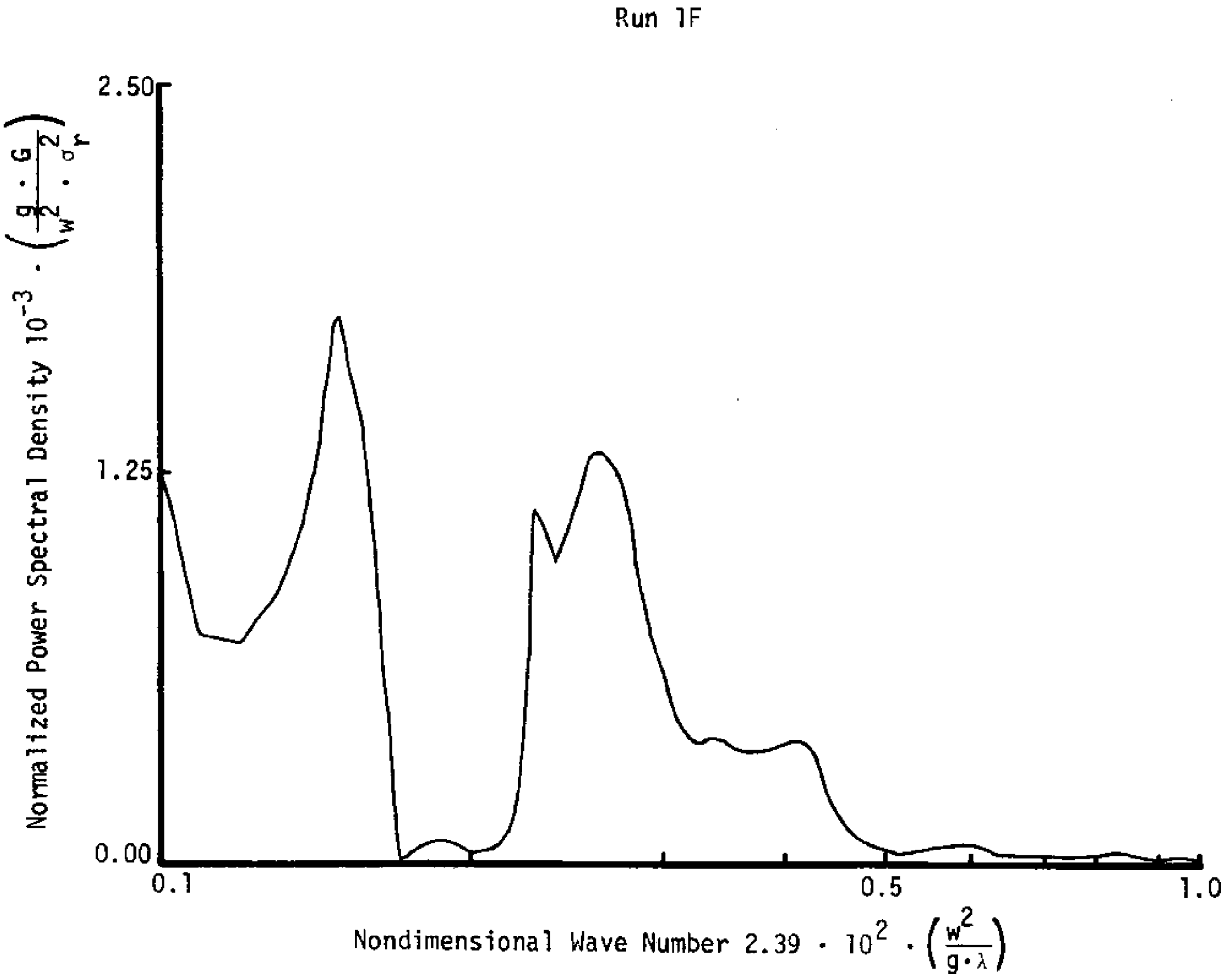

Figure 46. Spectrum of bed profile

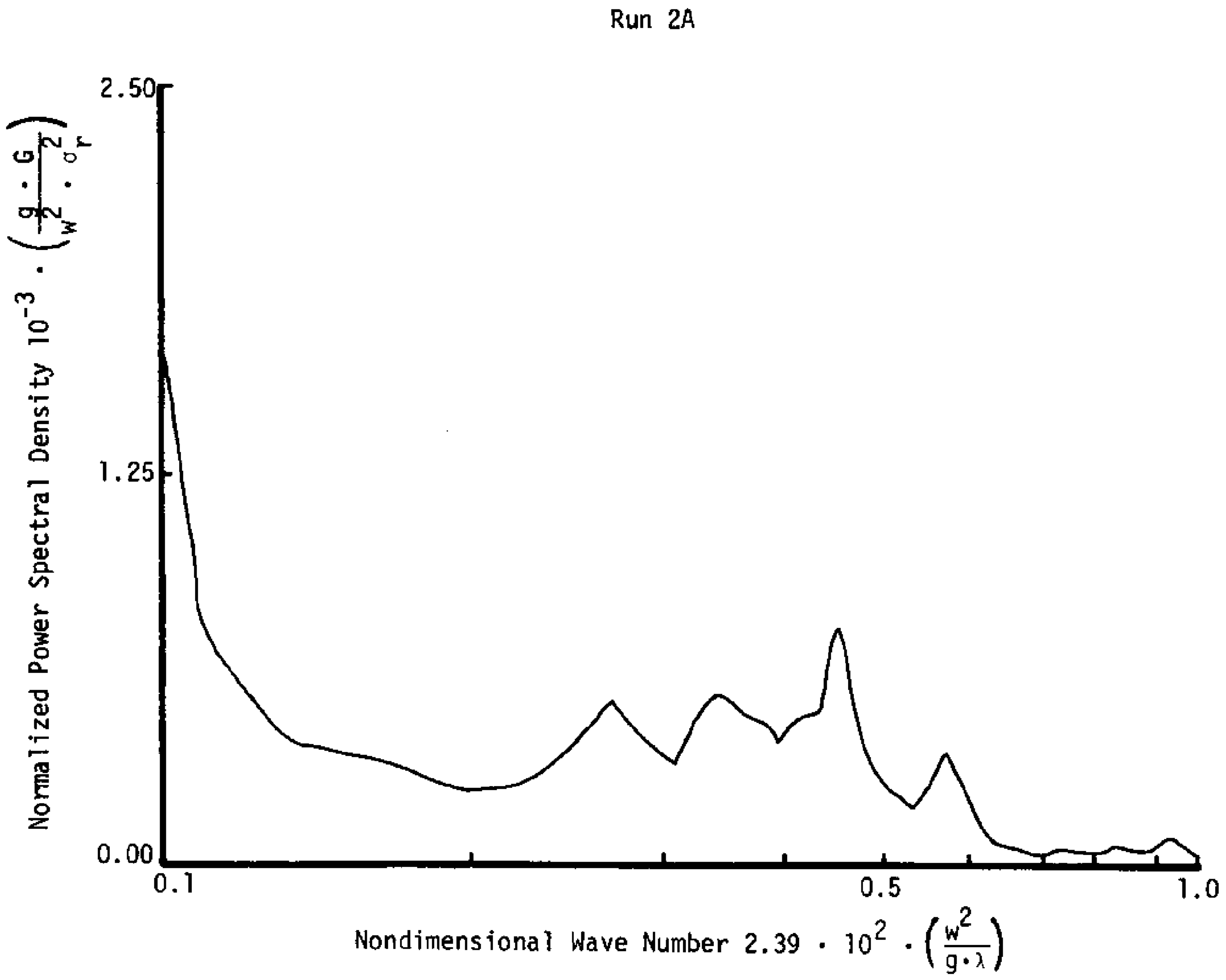

Figure 47. Spectrum of bed profile

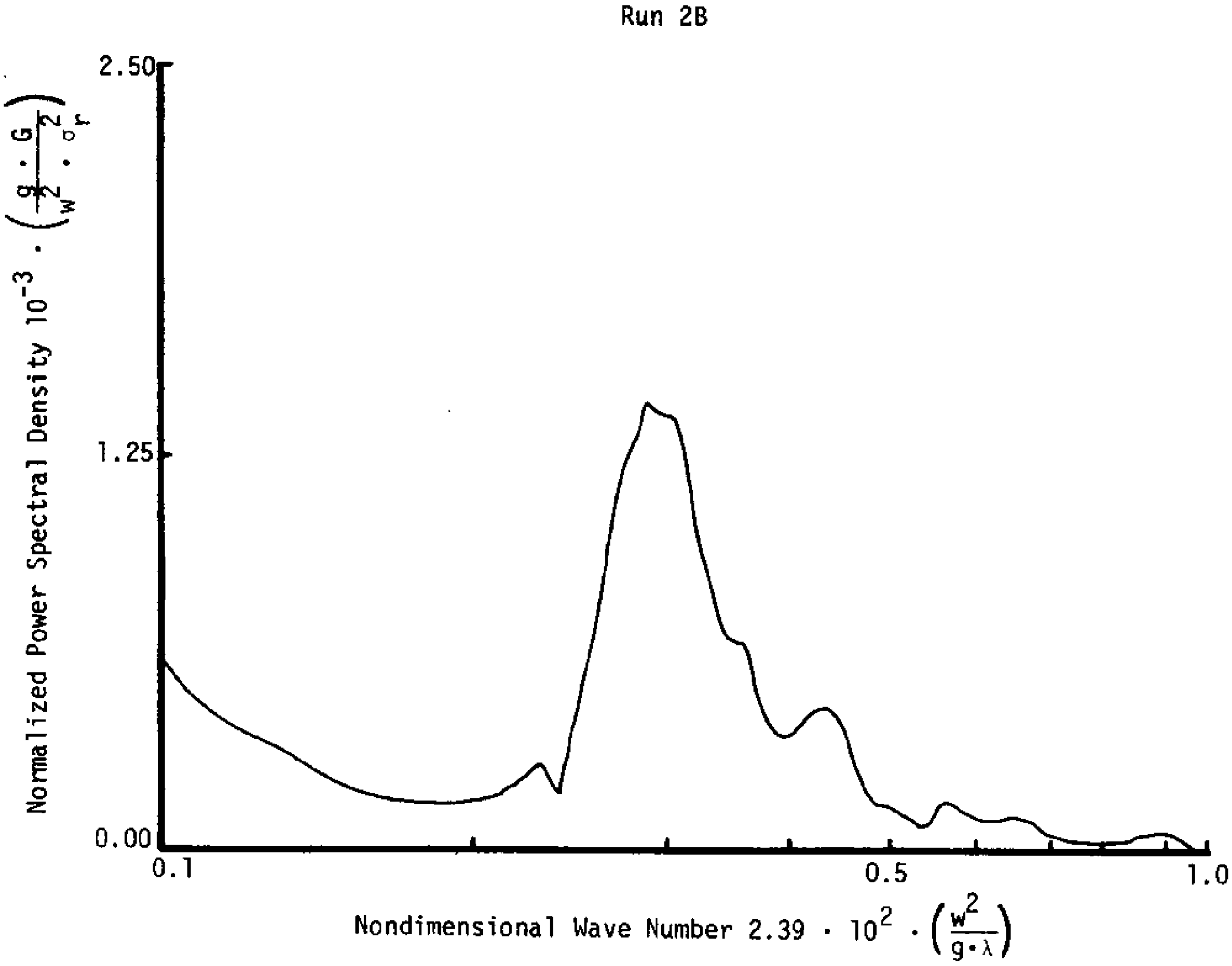

Figure 48. Spectrum of bed profile

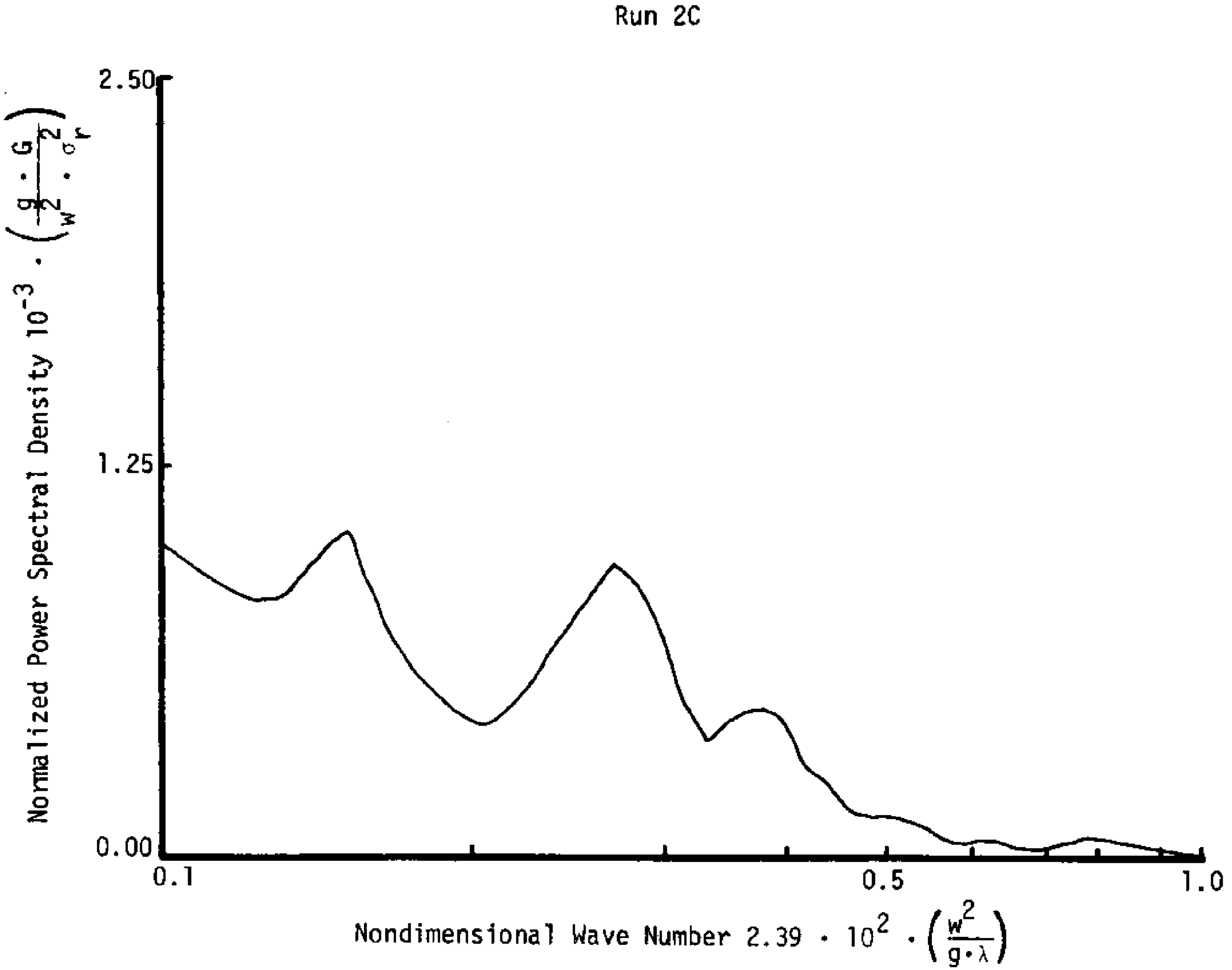

Figure 49. Spectrum of bed profile

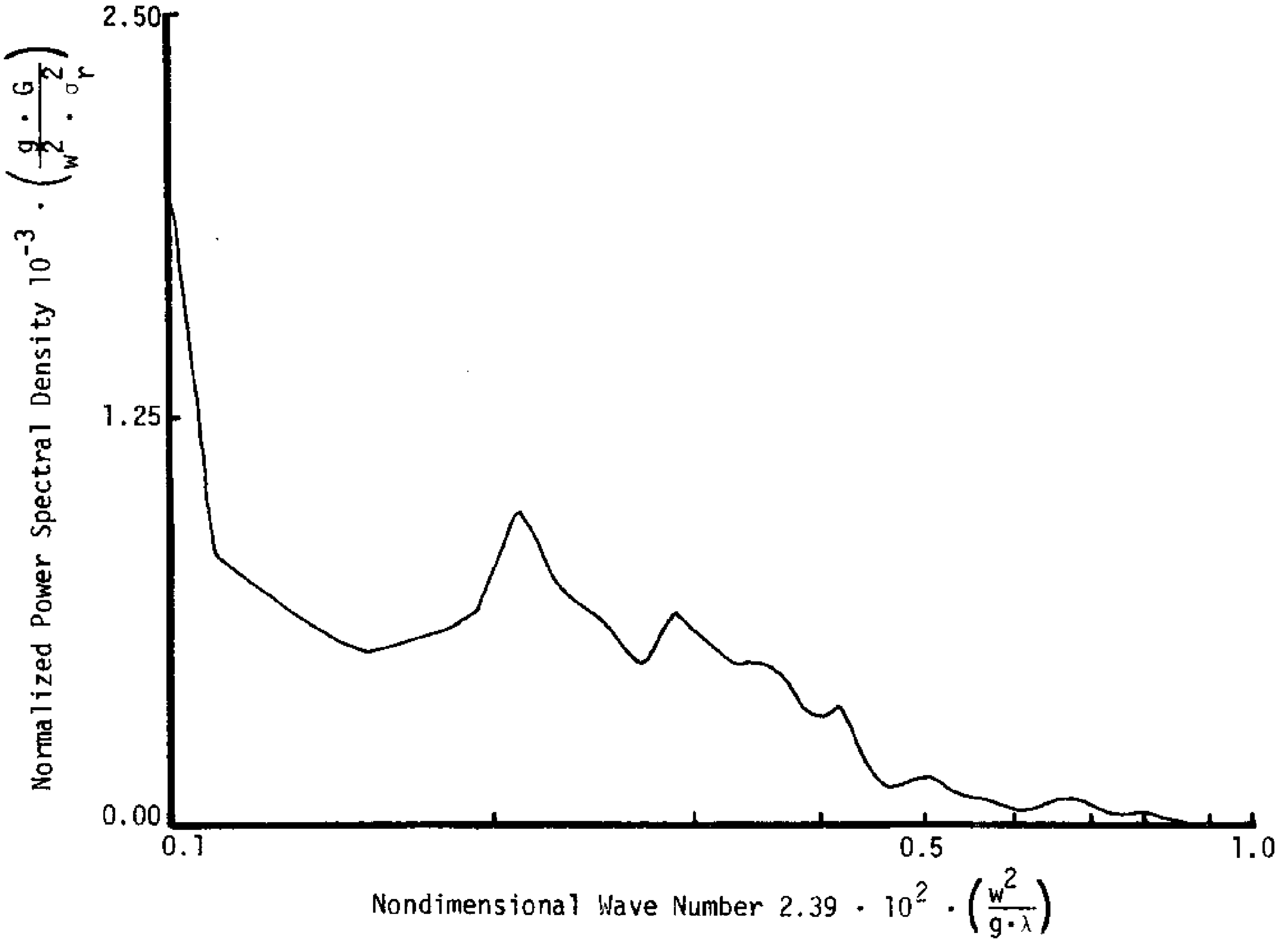
Run 3B

Figure 50. Spectrum of bed profile

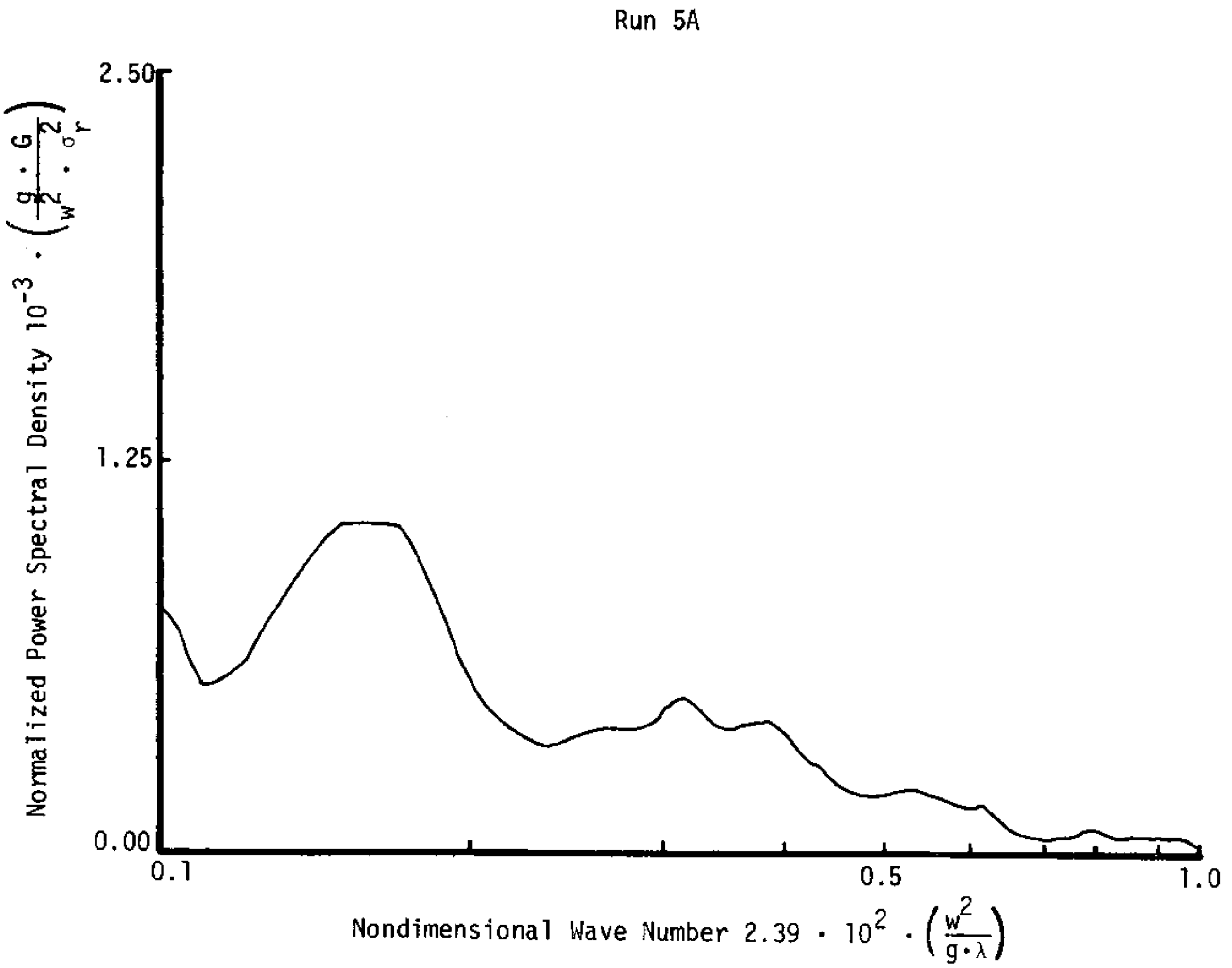

Figure 51. Spectrum of bed profile

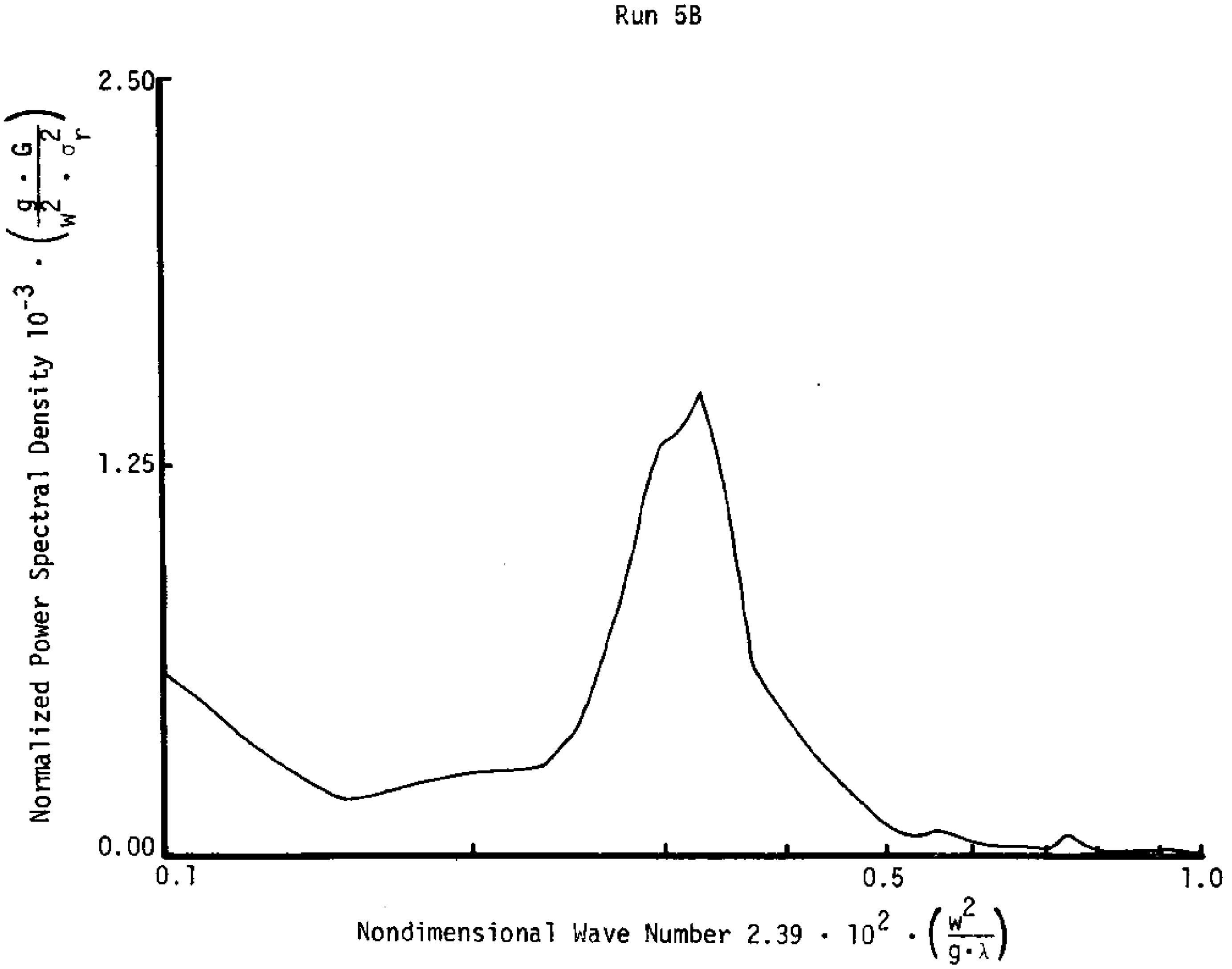

Figure 52. Spectrum of bed profile

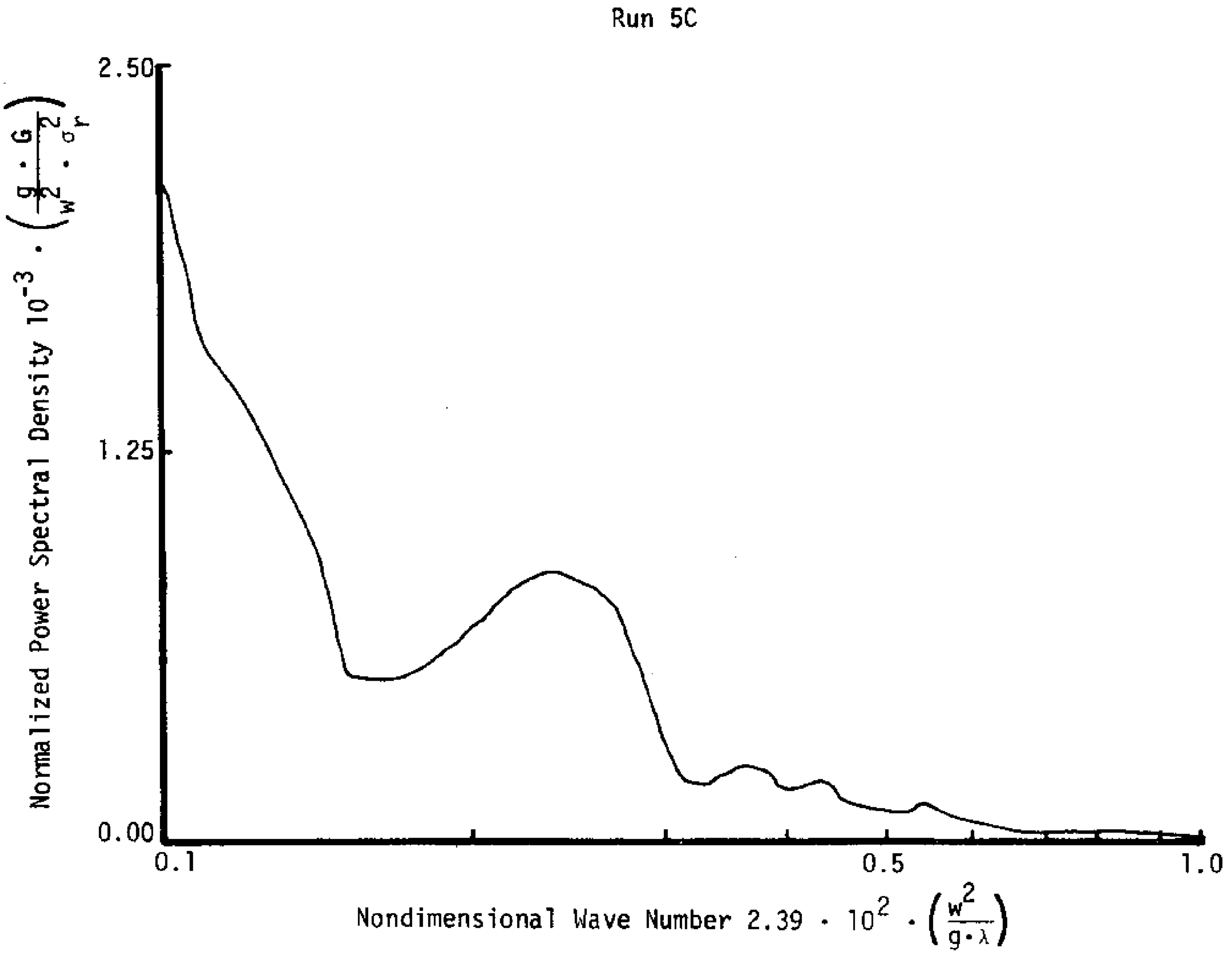

Figure 53. Spectrum of bed profile

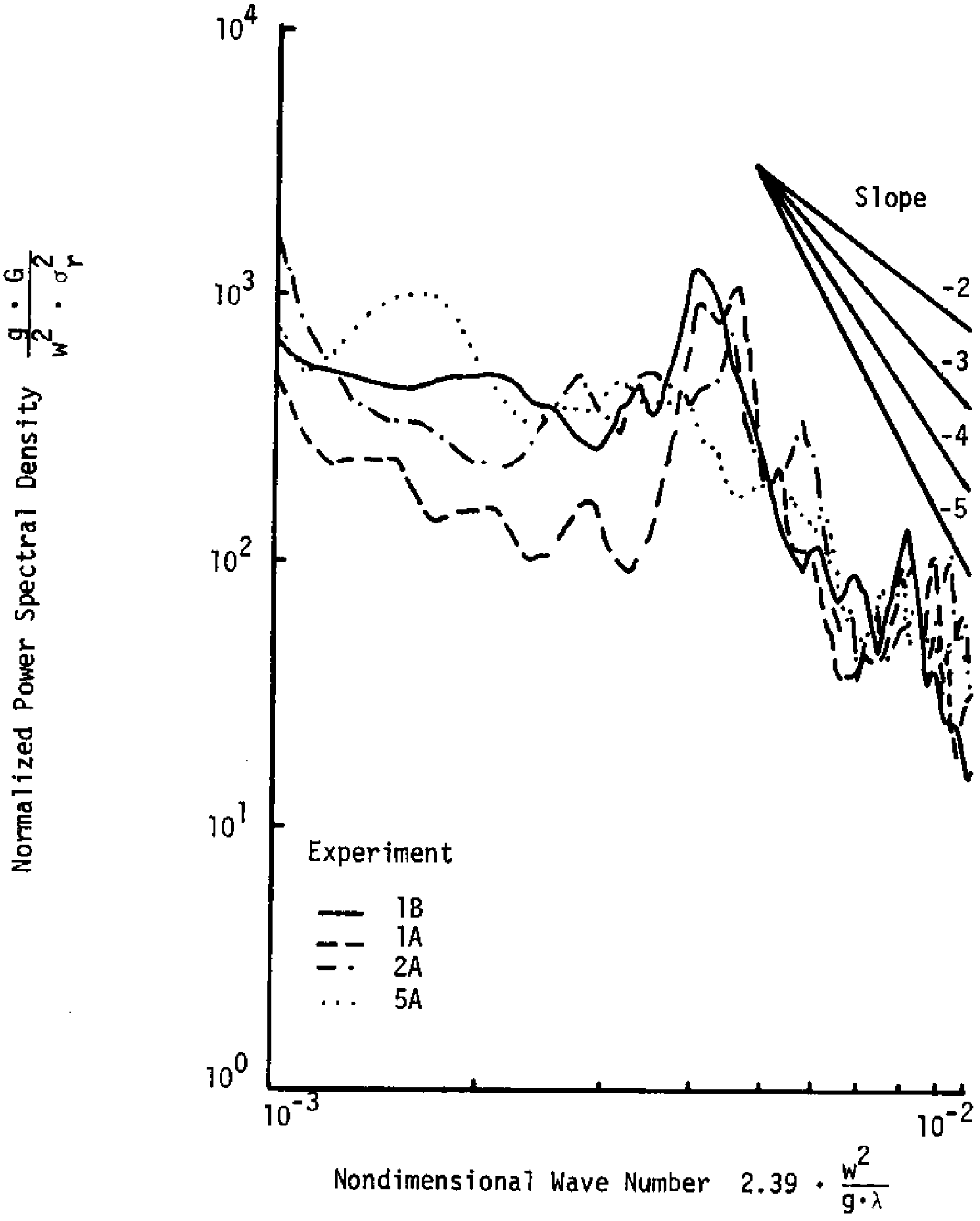

Figure 54. Spectra of bed profiles generated by progressive waves

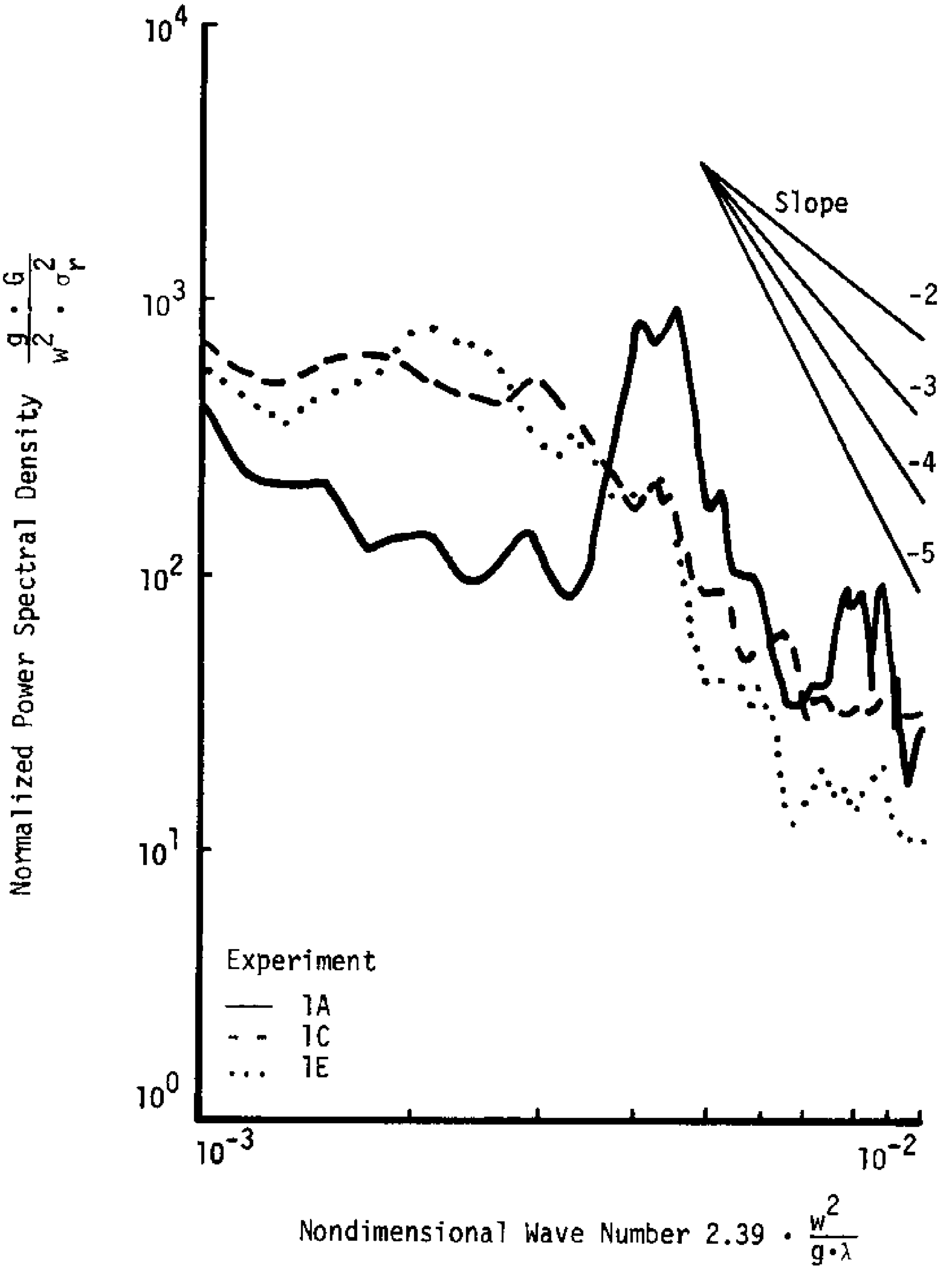

Figure 55. Spectra of bed profiles generated by combined flows

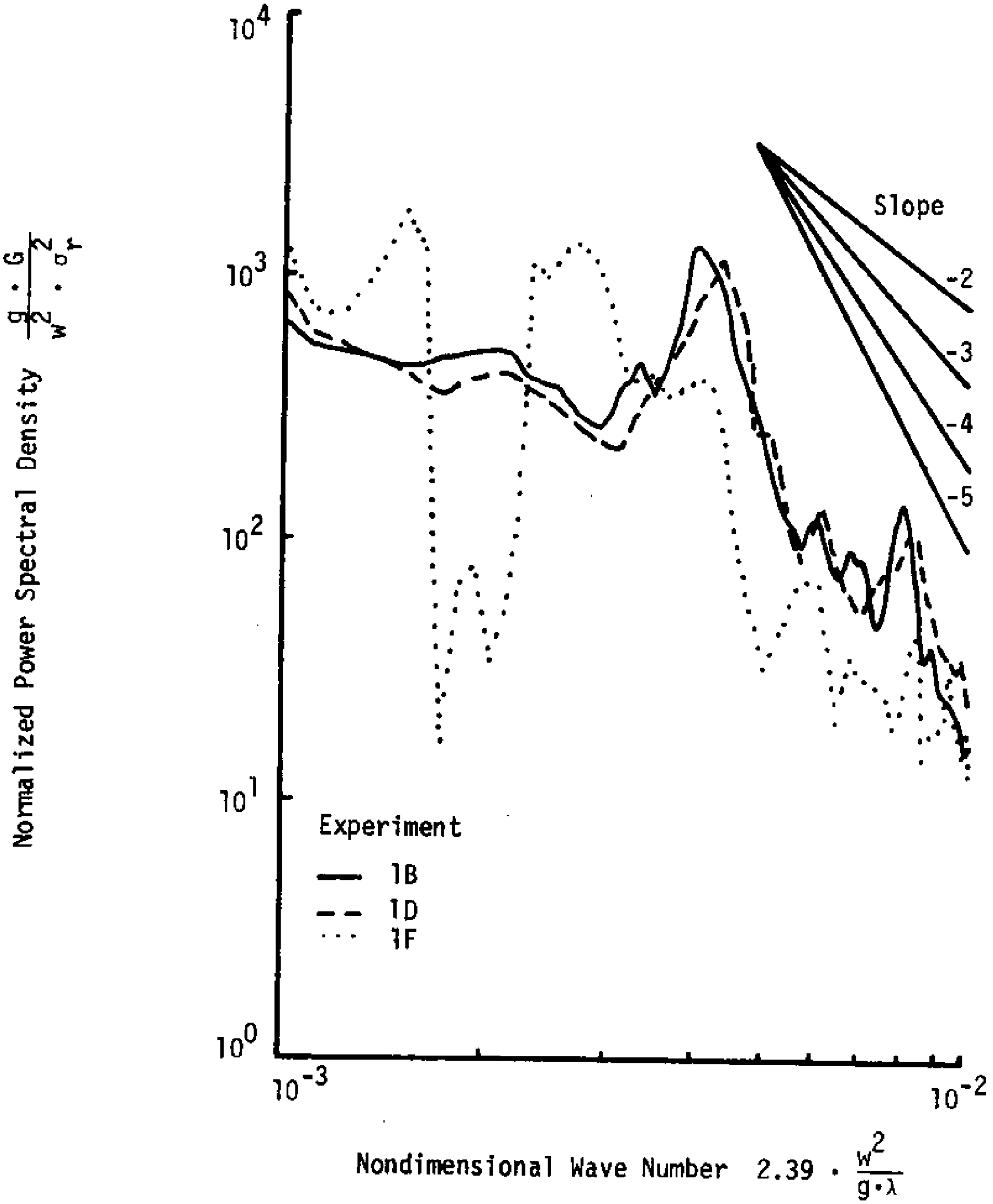

Figure 56. Spectra of bed profiles generated by combined flows

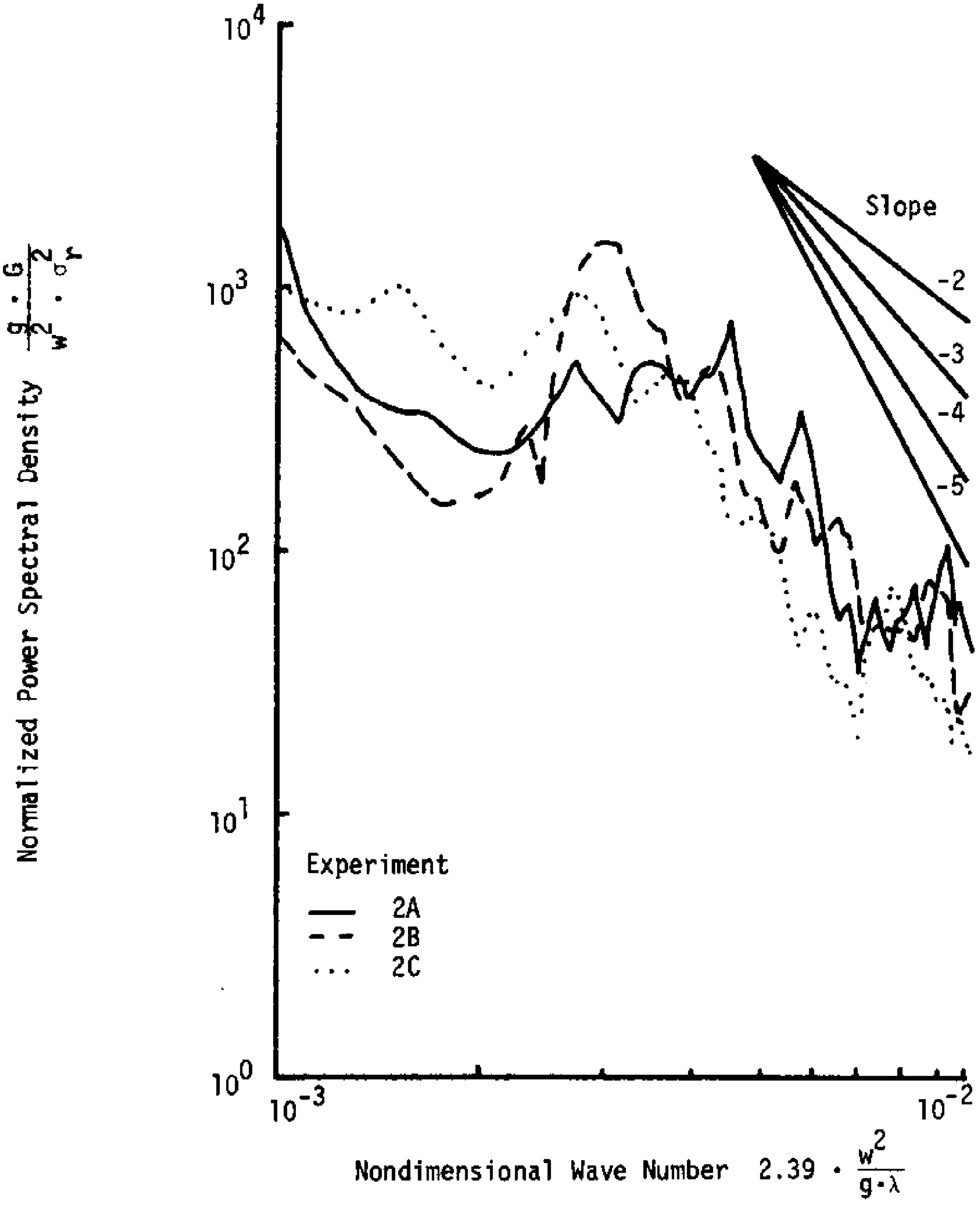

Figure 57. Spectra of bed profiles generated by combined flows

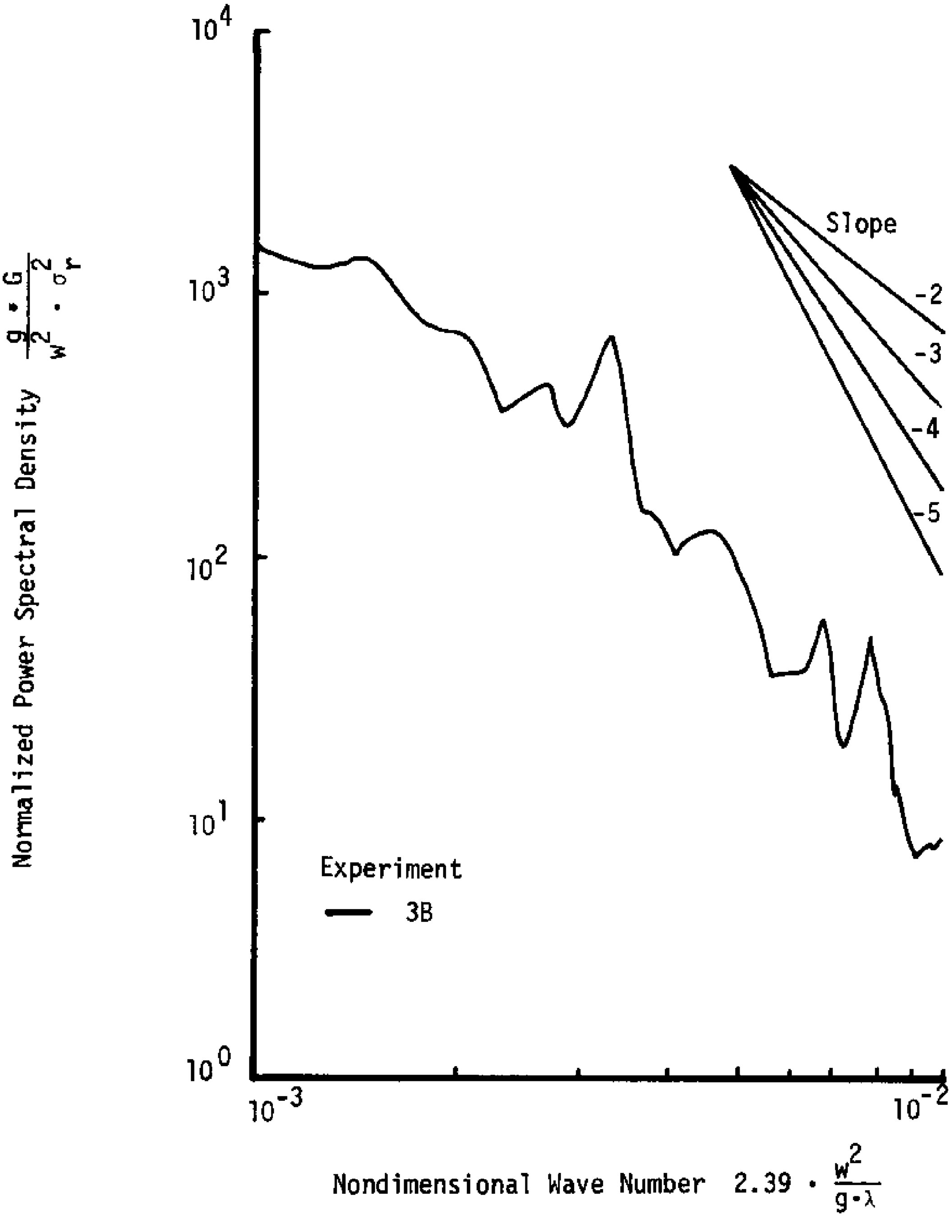

Figure 58. Spectrum of a bed profile generated by a combined flow

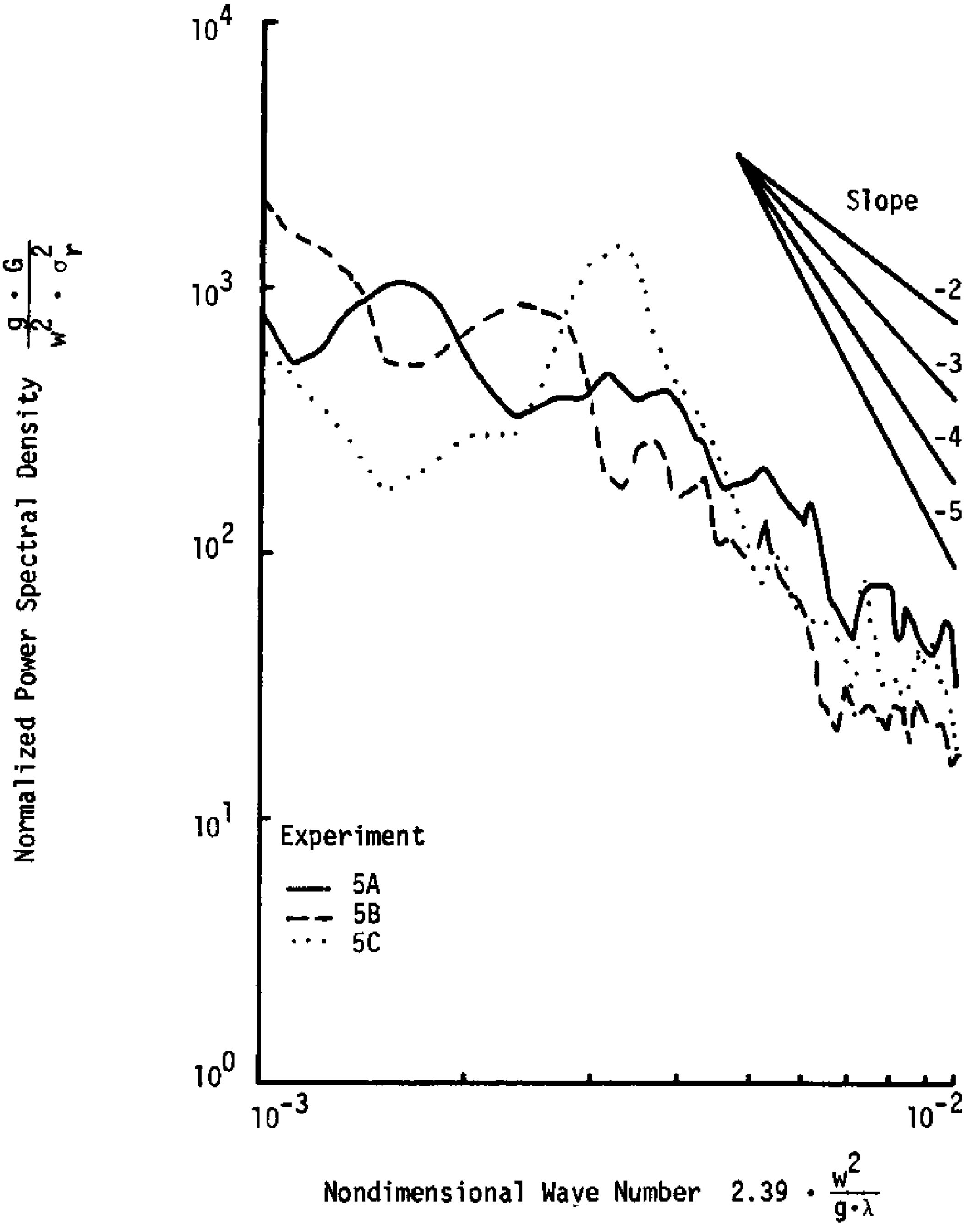

Figure 59. Spectra of bed profiles generated by combined flows

PREVIOUS PUBLICATIONS PUBLISHED
By
THE CENTER FOR MARINE AND COASTAL STUDIES

Wave-Current Force Spectra, C. C. Tung and N. E. Huang, Report No. 72-2, December, 1972.

A Survey of North Carolina Beach Erosion by Air Photo Methods, H. E. Wahls, Report No. 73-1, May, 1973.

Sediment Movement in Tubbs Inlet, North Carolina, Robert P. Masterson, Jr., Jerry L. Machemehl and Victor V. Cavaroc, Jr., Report No. 73-2, June, 1973.

Influence of Current On Some Statistical Properties of Waves, C. C. Tung and N. E. Huang, Report No. 73-3, December, 1973.

CTD Sensors, Specific Conductance and the Determination of Salinity, C. E. Knowles, Report No. 73-3, August, 1973.

Planning for North Carolina's Coastal Inlets - An Analysis of the Present Process and Recommendations for the Future, William S. Tilley, Report No. 73-4, September, 1973.

A Preliminary Study of Storm-Induced Beach Erosion for North Carolina, C. E. Knowles and Jay Langfelder and Richard McDonald, Report No. 73-5, October, 1973.

A Historical Review of Some of North Carolina's Coastal Inlets, Jay Langfelder, Tom French, Richard McDonald and Richard Ledbetter, Report No. 74-1, January, 1974.

Statistical Properties of Kinematics and Dynamics of a Random Gravity Wave Field, C. C. Tung, Report No. 74-2, June, 1974.

A New Technique of Beach Erosion Control, Tom French, Jerry L. Machemehl and N. E. Huang, Report No. 74-3, June, 1974.

Citizen Participation in North Carolina's Coastal Area Management Program, Steve Tilley, Report No. 74-4, June, 1974.

An Experimental Study of Scour Around Marine Foundations Due to Oscillatory Waves and Undirectional Currents, Greg N. Abad and Jerry L. Machemehl, Report No. 74-5, September, 1974.

Proceedings of A Conference on Coastal Management, Report No. 74-6, September, 1974.

Statistical Properties of Fluid Motion and Fluid Force in A Random Wave Field, Keikhosrow Pajouhi and C. C. Tung, Report No. 75-1, May, 1975

A Numerical Method for Solutions of Systems of Non-Linear Algebraic Equations , John M. Klinck and Leonard J. Pietrafesa, Report No. 75-2, July, 1975.

Wave-Current Interactions in Water of Variable Depths , A. M. Radwan, C. C. Tung and N. E. Huang, Report No. 75-3, August, 1975.

Conference Proceedings Energy From The Oceans Fact or Fantasy? , Jerome Kohl, Report No. 76-1, UNC-SG-76-04, January, 1976.

Long Waves Trapped by the Cape Fear Continental Shelf Topography: A Model Study of Their Propagation Characteristics and Circulation Patterns , David A. Brooks, Report No. 76-2, July, 1976.

A Comparative Study of Three Methods of Inhibiting Scour Around A Vertical Circular Cylinder, David M. Rooney and Jerry L. Machemehl, Report No. 76-3, September, 1976.

A Flow Study of Drum Inlet, North Carolina, Paul R. Blankinship, Report No. 76-4, UNC-SG-76-13 November, 1976.

Dune Stabilization with Panicum amarum Along the North Carolina Coast, E. D. Seneca, W. W. Woodhouse, Jr., and S. W. Broome, Report No. 77-1, UNC-SG-77-03, February, 1977.

A Mathematical Model of Nutrient Distribution In Coastal Waters, Eileen E. Hofmann, Leonard J. Pietrafesa, Larry P. Atkinson, Gustav-A. Paffenhöfer and William M. Dunstan, Report No. 77-2, February, 1977.

An Experimental Investigation of Some Combined Flow Sediment Transport Phenomena, Larry Bliven, Norden E. Huang and Gerald S. Janowitz, Report No. 77-3, UNC-SG-77-04, February, 1977.